DEVELOPMENT OF CARBON DOTS

FOR SECURITY INKS

by

Pelda Akin

A Dissertation Submitted to the
Graduate School of Sciences and Engineering
in Partial Fulfillment of the Requirements for
the Degree of

Master of Science

in

Materials Science and Engineering

KOÇ
ÜNİVERSİTESİ

January 21, 2022

DEVELOPMENT OF CARBON DOTS

FOR SECURITY INKS

Koç University

Graduate School of Sciences and Engineering

This is to certify that I have examined this copy of a master's thesis by

Pelda Akin

and have found that it is complete and satisfactory in all respects,

and that any and all revisions required by the final

examining committee have been made.

Committee Members:

_____

Prof. Havva Yağcı Acar (Advisor)

_____

Assoc. Prof. Uğur Ünal

_____

Prof. Duygu Avcı Semiz

Date: _____

[Dedicated to my dear family and friends]

ABSTRACT

Development of Carbon Dots for Security Inks

Pelda Akin

Master of Science in Materials Science and Engineering

January 21, 2022

Carbon Dots (CDs) emerged as metal-free promising nanoparticles creating new opportunities in optoelectronics, bio-applications, catalysis, sensing, security applications, *etc*. However, a profound understanding of the physical and chemical properties still pose a significant challenge. The origin of optical properties and emission tunning is not straightforward. The fundamental problem of this thesis work is towards elucidating the relationship between the structural/chemical features and the optical properties of CDs.

This thesis also addresses a daily problem: Authentication of valuable papers such as diplomas, banknotes, passports, etc. to prevent counterfeiting. Therefore, CD`s developed in this thesis was evaluated in inks and binders towards developing photostable optical tags. The documents were authenticated by measuring or reading these tags with special optical sensors or lamps.

Key words: Carbon dot, Fluorescent Ink, Counterfeiting, Security.

ÖZETÇE

Güvenlikli Mürekkepler İçin Karbon Noktacığı Geliştirilmesi

Pelda Akin

Malzeme Bilimleri ve Mühendisliği, Yüksek Lisans

21 Ocak 2022

Metal içermeyen, ümit verici nanoparçacıklar olarak orataya çıkan Karbon Noktacıkları (KN'ler) optoelektronik, biyolojik uygulamalar, kataliz, sensor, güvenlik vb. alanlarda yeni imkanlar yaratıyor. Fakat, KN'lerin karışık tabiatlarından dolayı fiziksel ve kimyasal özellikleri hakkında derin bir kavrayış kazanmak hâlen güçlük oluşturuyor. Optik özelliklerin kökeni ve emisyon ayarlanması kolay değil. Bu tez çalışmasının esas problemi, KN lerin yapısal/kimyasal özellikleri ile optik özellikleri arasındaki ilişkiyi aydınlatmak.

Bu tez aynı zamanda gündelik bir probleme de cevap veriyor: Sahteciliği önlemek amacıyla diploma, kağıt para, pasaport vb. değerli belgelerin doğruluğunun kanıtlanması. Bu yüzden bu tezde, geliştirilen KN'ler mürekkep ve bağlayıcı malzemelerde, fotostabil optik etiketler geliştirmek için değerlendiriliyor. Belgelerin doğruluğu özel optik sensörlerle ölçülerek ve lambalarla okunarak tespit ediliyor

Anahtar Kelimeler: Karbon noktacığı, Floresan Mürekkep, Sahtecilik, Güvenlik.

AKNOWLEDGEMENTS

I appreciated the people that I mentioned below, who sincerely helped and supported me during my MSc studies.

First and foremost, I would like to thank my dear advisor, Prof. Havva Yağcı Acar, for her passion for teaching, guidance, optimistic point of view, understanding, support and encouragement, which enabled me to be more productive, energetic and dedicated to my work through my whole MSc.

I would like to thank my thesis committee members Assoc. Prof. Uğur Ünal and Prof. Duygu Avcı Semiz for their effort and time while doing the evaluation of my thesis.

I am deeply thankful to Dr. Hadi Jahangiri for his numerous contributions and time in the optical and structural characterizations and friendly attitude during these two years.

I would like to thank Dr. Barış Yağcı for his contributions and time in the XPS measurements and friendly attitude during these two years.

I am deeply thankful to my beloved friend Kübra Nur Özvural Sertçelik, whom I spent most of the time, for her work in tandem, full support, kindness, and open-mindedness.

I would like to thank all the members of Polymers and Nanomaterials Research group, especially Kübra Nur Özvural Sertçelik and Mine Demir for their joy, support, encouragement, and invaluable friendship.

I am deeply thankful to my mother, father, and my sisters Nalan, Burcu and Esra for their sincere support and unconditional love and thankful to my little nephews Ekin, Can and Bulut for the joy and happiness they brought my life.

TABLE OF CONTENTS

LIST OF TABLES

LIST OF EQUATIONS

LIST OF FIGURES

ABBREVIATIONS

CD	Carbon Dot
QD	Quantum Dot
NP	Nanoparticle
UV	Ultraviolet
PL	Photoluminescence
QY	Quantum Yield
XRD	X-Ray Diffraction
TEM	Transmission Electron Microscopy
XPS	X-Ray Photoelectron Spectroscopy
FTIR	Fourier Transform Infrared Spectroscopy
DLS	Dynamic Light Scattering

CHAPTER 1 INTRODUCTION TO CARBON DOTS

1.1 Nanomaterials

Nanomaterials have been extensively investigated due to their unique size dependent chemical and physical properties. Unlike the traditional bulk forms, the physical properties of the nanomaterials including optical and electrical properties are size-dependent due to quantum confinement of electrons. Compared to traditional bulk forms, the large surface area to volume ratio in nanomaterials provides higher chemical reactivity which becomes vital in, for example, catalysis. Materials can be classified as nano-scaled when their size at least in one-dimension ranges from 1 nm to 100 nm (Müller Kerstin, 2017). Nanosized materials are characterized by free nanoparticles of various nano-dimensions as zero-dimensional, one-dimensional, two dimensional and three-dimensional (Murr et al., 2015). Nanoparticles can be classified under two main categories as organic and inorganic. Organic nanoparticles are dendrimers, liposomes, micelles etc., on the other hand inorganic nanoparticles are quantum dots, carbon nanoparticles, gold nanoparticles, superparamagnetic iron oxide nanoparticles etc.

1.1.1 Quantum Dots

The proposal of luminescent Quantum dots (QD) dates to 1980s. QDs luminesce upon light excitation, and they possess high photostability, broad absorption spectra, narrow and symmetric emission spectra, and a long luminescence lifetime. QDs are zero-dimensional semiconductor nanoparticles containing an inorganic core and usually an organic shell enclosing the crystal surface to passivate the active sites. The core size and type are mainly responsible for optical behavior. The shell around the core controls the shape and size and deactivates the surface defects to minimize non-radiative events responsible for emission intensity (Kouznetsov, 2016). The shell is also a barrier that separates the core from the medium. Several milestones in nanoscience and technology came from research related to QDs, such as size-controlled synthesis, quantum confinement effect, boundary effect etc. (Vinoth et al, 2021). Since the particle size ranges

from 1 to 10 nm, Quantum Confinement has a major role in the optical and electronic properties of QDs. As the semiconductor QD is illuminated by light up to some critical wavelength, light is absorbed. After that critical wavelength light is transmitted since the incoming light cannot satisfy the energy of the band gap between the valence and the conduction band anymore. Light absorption results in the excitation of a valence electron that is loosely bound by leaving a hole behind. The size of the separation between electrons and holes is called the *exciton Bohr radius*. There arises a Coulombic attraction between the positively charged holes and negatively charged electrons. If the size of the Quantum dot is smaller than the exciton Bohr radius, continuous energy states are quantized and become discrete, meaning finite separation between energy states of QDs. When the photoexcited electron returns to its original place and couples with the hole, absorbed energy is released as a photon, called as the luminescence. Hence, the color of emission (luminescence) is mostly determined by the size of the QDs and chemical composition, which determines the bandgap energy and is affected by the surface functional groups as well (Kouznetsov, 2016).

1.1.2 Carbon Nanomaterials

Carbon is the primary source of all organic molecules and constitutes nearly 50% of the dry weight of living things (Houghton, 2003). It is found in elemental form in nature as allotropes. These are graphite, coal, and diamond. Carbon allotropes are found in different structures and hybridization states, from sp^3 hybridized diamond to sp^2 hybridized graphite (Figure 1.1). This enables unique optical, chemical, and electrical properties that open a wide range of applications by using the same element (Mauter, 2008). Zero-dimensional, one-dimensional, and two-dimensional carbon nanomaterials (i.e., fullerenes, carbon nanotubes and graphene, respectively) have attracted significant attention in the last three decades. Diamond is a metastable form of carbon that possesses a three-dimensional cubic lattice; however, graphite is the most thermodynamically stable form of carbon at room temperature, which consists of sp^2 bonded carbons in a two-dimensional layered structure. Each layer has a hexagonal honeycomb structure, and the layers interact with each other via weak Van der Waals forces. By rolling two-

dimensional sp^2 hybridized graphene into a sphere, zero-dimensional fullerene was built. Their size ranges from 30 to 3000 carbon atoms (Jariwala, 2013). The discovery of fullerene (C60 bucky-ball) by Kroto (Kroto, 1993) accelerated the development of a different carbon crystal structure. Thereby, Carbon Nanotubes were discovered by Iijima in early 1990s by elongating the fullerene in one dimension (Iijima, 1991).

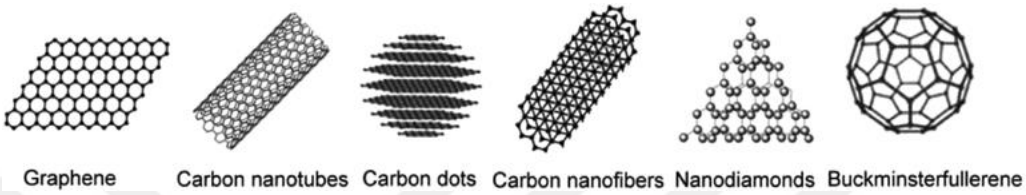

Figure 1.1: Carbon Nanoparticles (Wang Z, 2015).

1.2 Carbon Dots (CDs)

Carbon dots are the novel zero-dimensional carbonaceous nanomaterials that draw attention due to their high hydrophilicity, biodegradability biocompatibility, chemical stability, inertness, broad Stokes shift, low toxicity, ease of surface modification which resulted in unique optical properties (Alas, 2020). They are quasi-spherical in shape with a diameter of usually 1-10 nm (Wang Y. &., 2014). Most particles lack lattice fringes and happen to be amorphous; only some of them show crystalline graphite nature with well-resolved lattice fringes in TEM analysis (Wang et al., 2012).

CDs are synthesized by following two main routes: top-down and bottom-up methods. CDs generally have a conjugated carbon core encapsulated by a surface with various functional groups, such as carboxylic acid, amine, hydroxyl, and carbonyl moieties allowing their dispersion in different media (Li L. &., 2018). Depending on the core and surface characteristics CDs are classified into four main group as: Carbon Quantum Dot (CQD), Carbon Nano Dot (CND), Graphene Quantum Dot (GQD) and Carbonized Polymer Dot (CPD) (Ding H. L., 2020) . The GQDs are made up of single or a few graphene layers, having well defined graphene lattices and some functional groups at the edges. On the other hand, both CQDs and CNDs have a highly carbonized core and have chemical groups on their surface. CQDs have a well-defined crystalline core,

whereas CNDs generally don't possess obvious crystalline lattices. Lastly, CPDs have crosslinked carbon core and polymer chains on their surface.

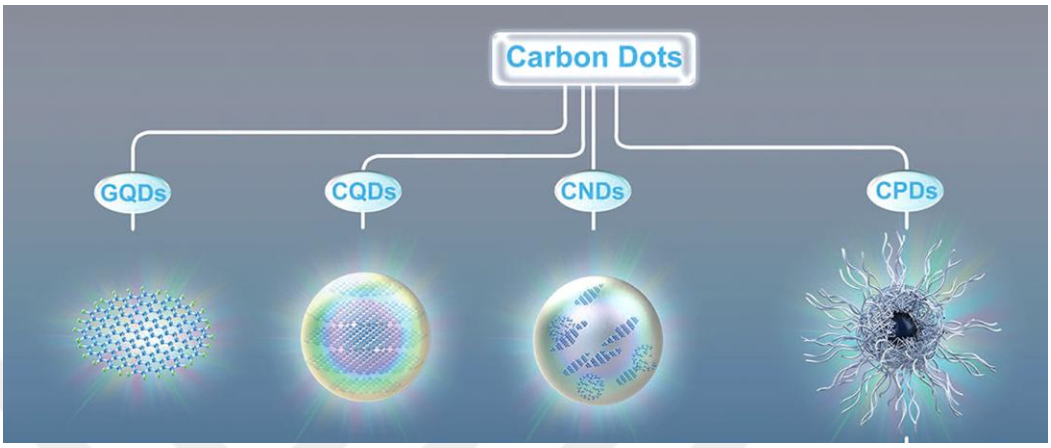

Figure 1.2: Carbon Dot Types. (Ding, 2020)

CDs are utilized in energy applications, for example, catalysis, LEDs, photovoltaics and in optical applications, for example, security/anticounterfeiting, sensing and in biomedical applications (Liu J. L., 2020). The majority of the CDs developed initially mainly exhibit a strong absorption in the UV range and dominant blue emission (Liu et al., 2018). CDs usually show an excitation dependent emission behavior, in other words, by increasing the excitation wavelength, the emission shifts to a longer wavelength but this is accompanied by a decrease in the emission intensity.

Biomedical applications, photocatalysis and security applications require CDs with emission at longer wavelengths, especially at red/NIR region (Zhu Z. Z., 2019). Tuning of the surface functional groups of CDs and choosing the proper reaction solvent and precursor are the major tools to shift the absorbance and emission of CDs to longer wavelengths (Bartolomei, 2021).

1.2.1 Synthesis of Carbon Dots

CDs are synthesized by two main routes: top-down and bottom-up methods (Figure 1.3). The top-down methods refer to the cutting of carbon materials into carbon nanoparticles, denoted as laser ablation, arc discharge, acidic oxidation, and plasma

treatment (Zuo, 2016). The bottom-up approach refers to the conversion of small molecules into CDs. These include hydrothermal treatment, pyrolysis, ultrasonic treatment, thermal decomposition, microwave assisted synthesis *etc*. (Sharma, 2019). Compared to top-down, the bottom-up approach is more widely used in the synthesis of CDs, allowing a careful selection of the precursors and a better property control (Liu et al., 2019). Also, bottom-up approaches are simpler and require fewer rough conditions. However, in general, in both methods, control over the size of the synthesized CDs is low.

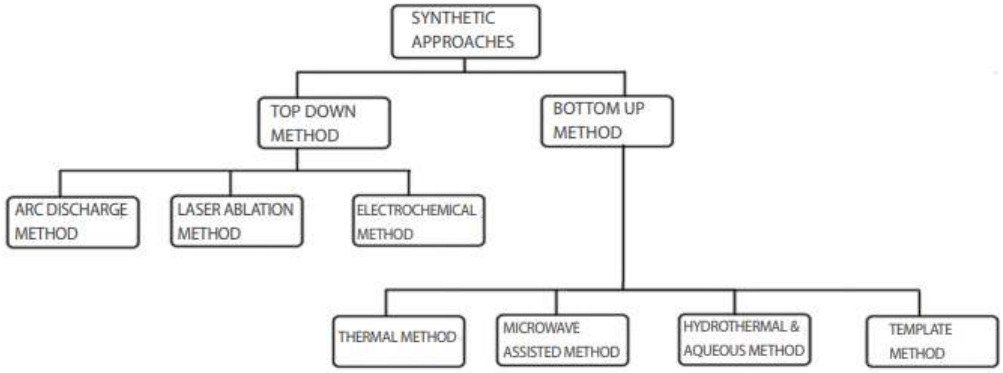

Figure 1.3: Carbon Dot Synthesis Methods. (Singh, 2018)

1.2.1.1 Bottom-up Methods

In the *Hydrothermal/Solvothermal Synthesis*, CDs are synthesized from small organic molecules by applying heat and pressure generally in Teflon lined stainless steel autoclave. First, the small organic molecule precursors get ionized and dissociated (Sharma, 2019). Second, they are condensed and further polymerize to form polymer-like carbon clusters. Third, they carbonize and nucleate to form CDs. In the *Pyrolysis*, carbon precursors are decomposed in a crucible under high temperature to form carbon nanoparticles. The Microwave assisted method benefits from the advantages of microwave and hydrothermal methods. It simply heats up the carbon precursors just in a few minutes by adjusting the power.

1.2.1.2. Top-down Method

In *Laser Ablation*, a carbon material is irradiated by laser under an inert atmosphere to cleave fluorescent carbon dots. In *Arc Discharge* method, the bulk carbon material constitutes the electrodes, anode and cathode. These electrodes are positioned closely under an inert atmosphere. When an electric field is applied, bulk material is cleaved, vaporized, and condensed on the cathode. In Acidic Oxidation strong acids decompose carbon target to form carbon nanomaterials with hydrophilic surface functional groups (Chen et al., 2012).

1.2.2 Absorbance of CDs

A typical UV–visible spectra of CDs display sharp absorption peaks in the UV region ranging from 240 to 330 nm. Approximately the UV absorbance at 240-270 nm corresponds to π-π* electronic transition of C=C bonds and 300-330 nm corresponds to n- π* electronic transition of C=O or C=N bonds (Figure 1.5) and the absorption tail extends to visible region (Alas et al., 2020). Modifications to the interior or surface structure e.g., surface passivation/functionalization and heteroatom doping, lead to a shift in the absorption maxima (Wibrianto, 2020).

1.2.3 The Theory and The Factors Affecting Fluorescence

Pauli Exclusion principle states that only two electrons that acquire opposite spin can occupy an orbital since no two electrons can have the same four quantum numbers (Singh, 2016). Therefore, the electrons in the orbitals are always paired. When light (photon) interacts with a molecule, the molecule absorbs the light up to a critical wavelength correlated with the energy of the incoming photon. Once the energy of the photon is absorbed by the molecule, the valence electrons in the ground energy level (S_0) excite into higher singlet energy states (S_1, S_2) with an opposite spin relative to the electron in the ground state. Since the excited energy states are not stable, there occurs either radiative or non-radiative relaxation processes to the ground state. The radiative relaxations are called *photoluminescence* (PL). There are two scenarios for

photoluminescence. The first scenario is the internal conversion and/or vibrational relaxation of the excited electrons to the lowest energy state of S_1 to make fluorescence. Second is the intersystem crossing from S_1 to T_1 (triplet state) to make phosphorescence (Itoh, 2012).

As can be seen in Figure 1.4a, in the Singlet State (S_1, S_2) the excited electron has an opposite spin relative to the one in the ground state; however, in Triplet State (T_1) the electron is parallel relative to the one in the ground state. There is no direct excitation from ground to a triplet state, requiring a change in multiplicity (Skoog et al., 2018).

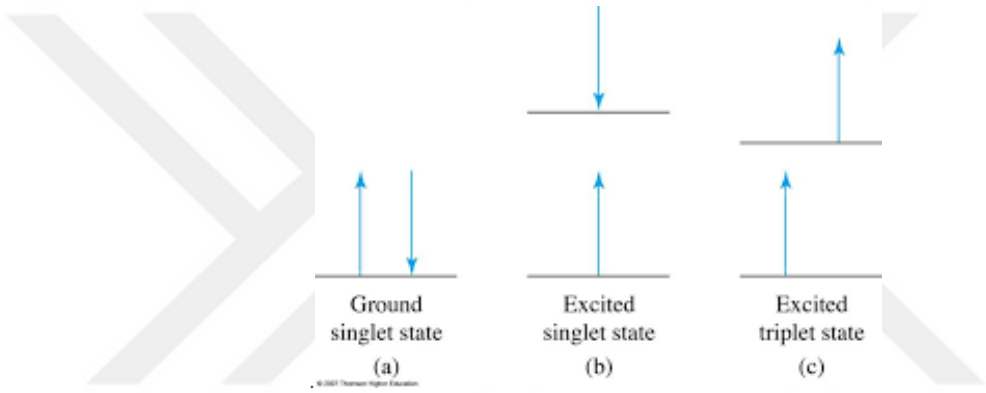

(a)

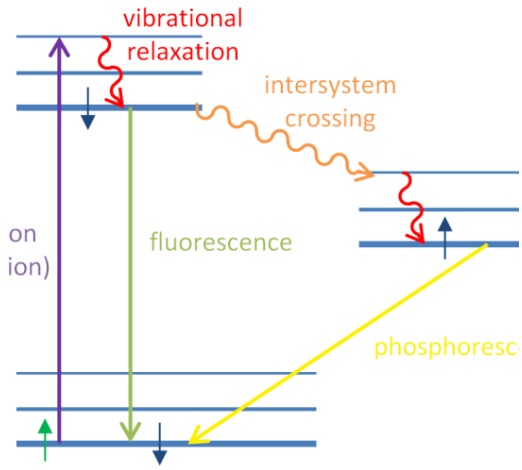

(b)

Figure 1.4: (a) Energy States (IYTE, 2021) , (b) Jablonski Diagram (Eck., 2014).

As can be seen in Figure 1.4b, there is no change in the electron spin for molecular fluorescence; however, there is a change in electron spin for phosphorescence. Therefore, the lifetime of a triplet excited state phosphorescence, ($\sim 10^{-4}$ s to minutes or even hours) is much longer than a singlet state fluorescence, (10^{-8}s) (Bhattacharyya S. &., 2011). The singlet state has higher energy than the excited triplet state (Figure 1.4b). Fluorescence take place from the lowest vibrational energy level of S_1 to the ground state and it is observed because of the $\pi^* \rightarrow \pi$ and $\pi^* \rightarrow n$ transitions, not by $\sigma^* \rightarrow \sigma$ transition, which requires highly energetic photons (Kalsi, 2007). This high energy photon might damage the organic molecules.

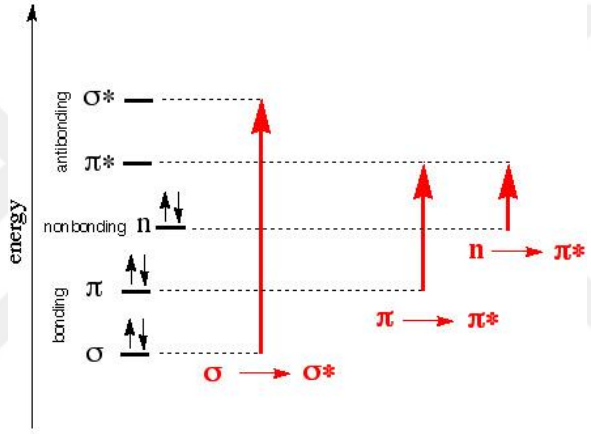

Figure 1.5: Energy of Transitions (Chem UCLA, 2021).

There are some factors affecting fluorescence. These are:

Structure and Rigidity: Molecules having aromaticity are more prone to fluorescence due to easy excitation of delocalized electrons by $\pi \rightarrow \pi^*$ transition. When the rigidity around fluorophores increases, the intermolecular interaction (Mizobe et al., 2006) and probability of internal conversion, in other words, radiationless relaxation between the states of the same multiplicity, decrease. Whereas, non-rigid structures, dangling bonds etc. lead to losing some of the absorbed energy by vibrational relaxations, leading to weak fluorescence intensity and low Quantum Yields (QY) (Chen et al., 2019). QY means how efficiently does absorbed light is converted into emitted light during fluorescence.

Temperature and Viscosity of solvent: Low temperature and high viscosity conditions are preferred to eliminate the probability of External Conversion and increase the fluorescence QY, accompanied by a decrease in the rate of molecular collision. External Conversion stands for the radiationless relaxation of excited molecules due to collision with other molecules such as solute or solvent.

pH: As the pH of the environment decreases, the pH-dependent substituent of the aromatic ring gets protonated. This protonation leads to the increase in resonance species of the excited molecule. An increase in resonance species stabilizes the excited state of that molecule (Skoog et al., 2018).

Concentration/ inner filter effect: When the fluorophore concentration is too high, the linearity between the concentration of analyte and fluorescence intensity diminishes. A particle emits light, and the emitted light is immediately captured by another molecule due to the close contact of the analyte molecules at these high concentrations.

1.2.4 The Mechanism of CD Fluorescence

Photoluminescence of CDs is the main property that is being exploited. Generally, emission wavelength and intensity characteristics of CDs are dependent on the excitation wavelength. As the excitation wavelength increases, emission shifts to the longer wavelengths accompanied by a decrease in Photoluminescence (PL) emission intensity (Tang et al., 2012). The reason of CD photoluminescence has been attributed to surface properties such as carbon excitons, emissive traps, aromatic conjugate structures, free zigzag region, heteroatom doping and surface passivation/functionalization. Sun *et al.* reported that after the passivation of CD surface with some polymeric materials such as poly(propionylethylenimine-co-ethylenimine) (PPEI-EI) and polyethylene glycol (PEG), they obtained a stronger PL emission due to stabilization of the existing surface defects (Sun et al., 2006). In general, down-conversion in PL properties is observed with CDs, meaning light is emitted at a longer wavelength than the excitation wavelength; namely a Stokes shift is observed (Figure 1.6). In up-conversion PL, light is emitted at a shorter wavelength than the excitation wavelength, anti-Stokes type emission (Haase, 2011).

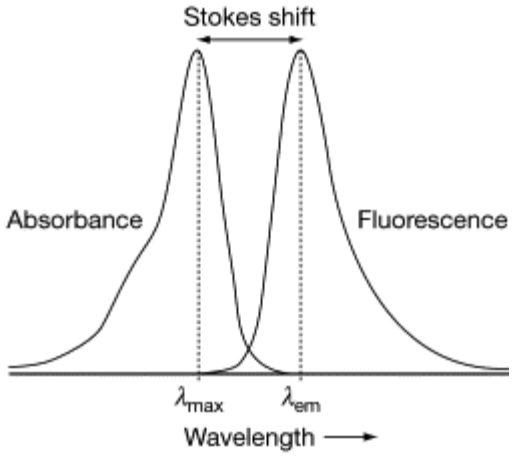

Figure 1.6: Stokes shift (Bhattacharyya et al.., 2011).

1.2.4.1 Bandgap Emission

The sp^2 carbon structures of CDs are dispersed in the sp^3 carbon skeleton. The π electron delocalization in sp^2 cluster leads to band gap separation. This delocalization and the separation between π electron states have a major role in determining the optical properties. When the particle size of CD is smaller than the Exciton Bohr radius, Quantum Confinement Effect (QCE) of conjugated π electrons take an important role in the emission color. The continuous energy bands of CDs turn into discrete energy levels. As the size of the material decreases, the band gap energy increases. Particularly for CDs with large conjugated π-domains, fluorescence is mainly derived from the QCE, in other words the size of the conjugated π-domain in the carbon core is responsible for the (π-π*) band gap opening, playing the major role in fluorescence emission (Yan, The fluorescence mechanism of carbon dots, and methods for tuning their emission color: a review, 2019). As the size of conjugated π-domain increases, the bandgap gets smaller and the energy of the photon to excite an electron from conduction to valence band decreases. This results in a red shifted emission. So, by adjusting size of conjugated π domain, the emission color of CDs can be tuned. One way of adjusting the size of the conjugated π-domain is using different reaction solvents, which creates different active sites to enhance the carbonization (Zhu Z. Z., 2019). Tian et al. demonstrated that using different solvents such as water, glycerol, and dimethylformamide affects the dehydration and carbonization processes during the high temperature and pressure, solvothermal

reaction. Each solvent results in carbon dots with different particles sizes and different dimensions of conjugated sp^2 domains, determining their emission colors (Tian, 2017). As the reaction temperature increases, the contribution of carbogenic core to the emission also increases (Zhu et al., 2013).

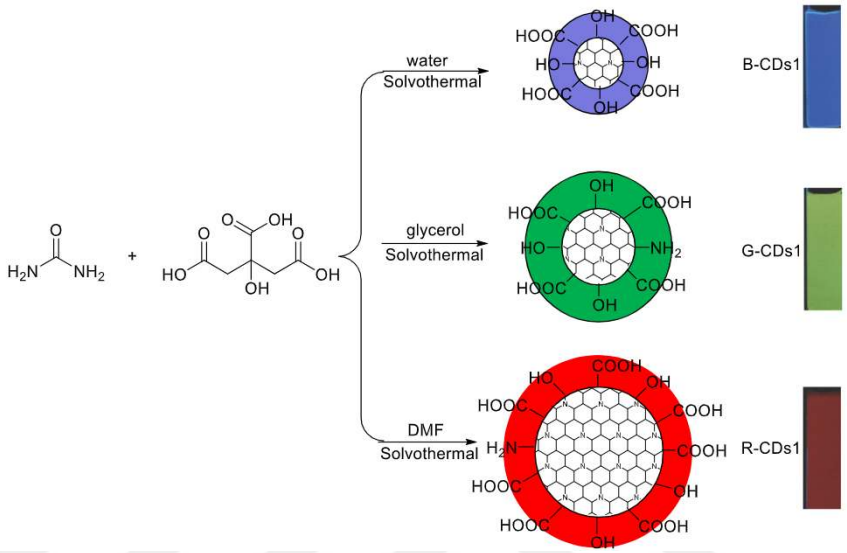

Figure 1.7: Different color emitting CDs obtained by changing reaction solvent. (Tian, 2017)

1.2.4.2 Surface/Intrinsic Defect State Emission

Apart from the traditional particle size dependent emission of the QD, fluorescence of CDs is dominated by the surface or intrinsic (sp^2 domain) defect sites (Figure 1.8). The surface of CDs is surrounded by various functional groups such as amide, carboxylic acid, hydroxyl, thiol, some chemical moieties having sp^2/sp^3 hybridized carbons or dangling bonds. The defects are generated by heteroatom doping during the synthesis. These defects can act as series of emissive traps or capture centers for excitons.

As we know, when a photon hits the CD surface and absorbed, the valence electron is excited to a higher energy level. As the energy of incoming light changes, each photon is absorbed by a different energy state and a bandgap. In other words, each photon is captured by a different trap center. As a result, fluorescence is obtained by the emission of dominant emissive traps (Sahu, 2012). Therefore, the emission can be tuned by varying the chemical groups on the carbon dot core/surface. Yang *et al.* suggest that the addition of different acids or bases to the reaction precursor results in CDs with multiple functional

groups and multiple emission centers. The different emission colors come from different growth and nucleation processes (Yang P. Z., 2019). In addition, pH treatment after synthesis leads to the domination of different luminescent centers that result from different defect states.

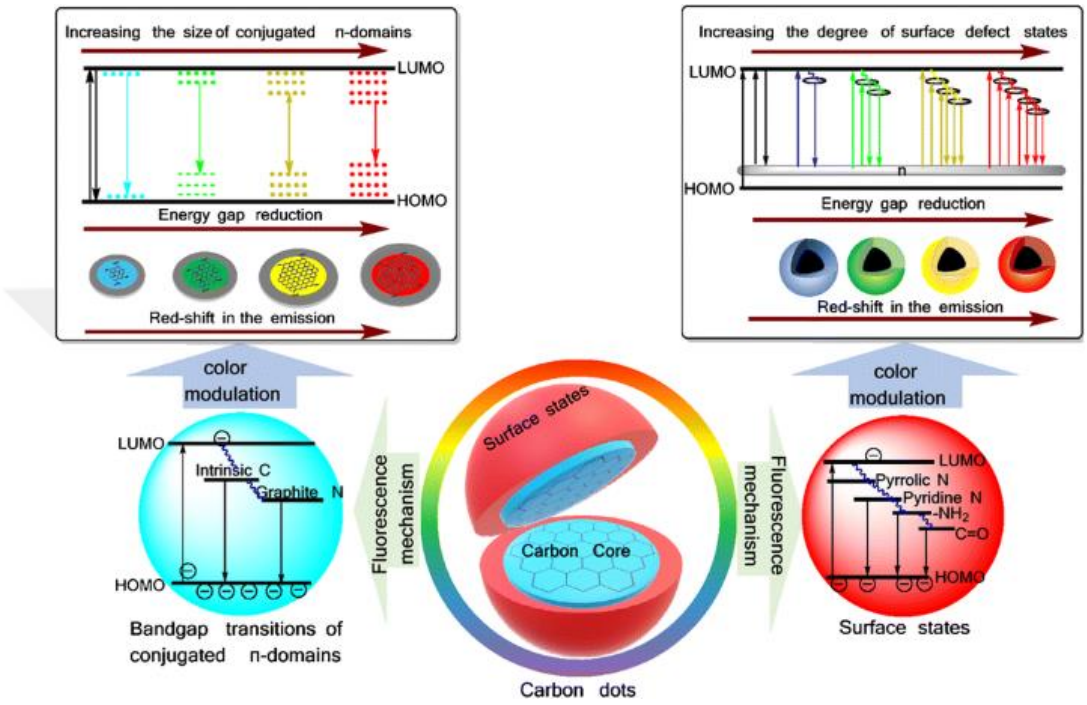

Figure 1.8: Modulation of bandgap by surface/intrinsic defects. (Yan et al., 2019)

Heteroatom Doping

Introducing an electronegative heteroatom (O, N, P, etc.), an impurity, to carbon dot modifies its electronic properties creating an n-type semiconductor (Xu et al., 2016). The heteroatoms readily donate electrons to the system and increases the local electron density. New energy levels in its bandgap lead to changes in luminescence color. Xu *et al.* mentioned that increase in nitrogen content and Yang *et al.* states that increase in graphitic nitrogen content and increase in electron density provides higher radiative recombination, thereby enhanced emission intensity and QY (Xu et al., 2015 and Yang et al., 2020). The more delocalized electrons result in a longer PL decay lifetime (Li et al., 2020). Moreover, these introduced heteroatoms on the CD surface provide better solubility and chemical reactivity (Kouznetsov, 2016).

Nitrogen Doping

As the size and structure of N is like the C atom, it can be easily incorporated to the carbon skeleton. The electronegative N atom provides extra electrons to the CD, which enhances the electron delocalization. N-CDs consist of four main nitrogen types, which are pyridinic, pyrrolic, graphitic and amine (Figure 1.9). The pyridinic-N bonds with two C atoms in a hexagonal array and the pyrrolic-N bonds with two C atoms in a pentagonal arrangement. This N containing moieties are mainly located at the edge of CDs, however, graphitic Ns are embedded inside the sp^2 region replacing by vacancies. Graphitic N bonds to three C atoms in sp^2 configuration creating intrinsic defects and the amines are located on the surface of CDs.

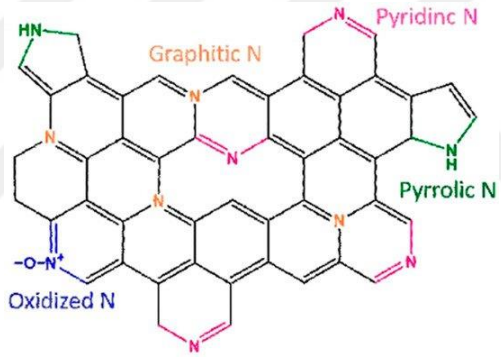

Figure 1.9: Different amine types in conjugated structure (Zhou, 2018).

Sudolská *et al.* claim that pyrrolic or pyridinic N cause a blue shift in emission, while graphitic N causes a red shift (Sudolská et al.,2017). Graphitic N generates mid-gap states within the HOMO−LUMO gap of the undoped systems, resulting in significantly red-shifted light absorption and fluorescence at longer wavelengths (Holá, 2017). The graphitic nitrogen increases the structure's rigidity, therefore reduces the non-radiative relaxation through molecular vibrations on CD surfaces. However, at the edges of the aromatic π-domains the pyrrolic and pyridinic N or pendant amine groups decrease rigidity, which give rise to vibrational modes, stronger non-radiative recombination channel and facilitated energy/charge transfer towards the external defect sites (Bhattacharyya et al., 2017). On the other hand, Permatasari *et al.* and Tetsuka *et al.* respectively, suggested that pyrrolic nitrogen and surface amine groups are shifting the

emission to a longer wavelength, by modifying the electronic structure of CDs (Permatasari et al., 2018 and Tetsuka et al., 2012).

Oxygen Doping

Surface oxidation increases the number of surface defects. Oxygen doping introduces new energy states lying lower than the energy of carbon-carbon double bonds (C=C). As the degree of oxygen incorporation increases, the number of excitons trapped by these oxygen-related defects increase (Bao, 2015). The gradual reduction in the bandgap leads to a redshift in emission (Liu et al., 2019). Mahasin *et al.* suggest that oxidation at sp^2 clusters can exert a stronger redshift in emission wavelength than oxidation at sp^3 carbons (Mahasin et al., 2014).

1.2.4.3 Molecular State Emission

The fluorescent molecules are small organic molecules that are bonded to the surface or core of the carbon. They can act as an individual chromophore and exhibit fluorescence emission directly. It is common to obtain these small molecules during the condensation and carbonization process of CD synthesis. Rogach *et al.* showed that molecular fluorophores have a significant influence on the optical properties of CDs (Rogach et al., 2017). At lower carbonization temperatures, molecular state emission dominates due to polymer-like CDs formed. On the other hand, at higher reaction temperatures, the carbon core plays a dominant role, consuming some part of the molecular fluorophore to form a crystalline carbon core (Song, 2014).

CHAPTER 2 CARBON DOTS FOR SECURITY INKS AND THE PROBLEM TO BE SOLVED

2.1 Introduction

2.1.1 Anti-Counterfeit Studies in the Literature

Counterfeiting in documents such as diplomas, banknotes, passports and in many industries such as food, oil, drug is very common. Over 1.7 trillion dollars annual loss account for the counterfeited products, exceeding 2% of total global current output (Gasiorowski, 2014). These illegal activities are not only unethical, but a great problem in insurance coverages, national economies and sometimes pose a risk for the public health and indeed worry the consumers (Geiger, 2012). Hence, for the prevention of counterfeiting, some technological solutions were developed. Barcodes, holograms and watermarks are examples that are already in use, which sometimes cannot escape reproduction. Since they are easy to duplicate (Sun et al., 2017).

To date, various fluorescent materials have been developed to be used as security ink, such as organic dyes, inorganic QDs, rare earth compounds etc. QDs and organic dyes were preferred due to narrow emission half bandwidth and adjustable photoluminescence (Kumar *et al.* as cited in Pang *et al.*). Organic dyes suffer from low photostability, photobleaching and small Stokes shift. QDs are usually expensive and not yet cleared completely for safety, although some examples made their ways to TVs, especially in food-contacting products, products that are in direct contact with the consumer and for the products that will end up in the environment (Pang, 2018).

2.1.1.1 Carbon Nanomaterials Based Luminescent Inks

As a general trend, aqueous and nitrogen doped carbon nanoparticles, such as carbon nanodots (CND) and graphene quantum dots (GQDs), are exploited as luminescent ink in the literature. Pang *et al.* suggested that N-doped CDs perform have higher QY than pristine CDs (Pang, 2018). These particles are chosen for better dispersion in water due to enhanced surface functional groups such as NH_2, NO_2, C=N *etc.*

The pioneer carbon dot-based inks (Figure 2.1) were prepared by blue emitting CDs (under UV light), having a QY nearly as high as organic dyes, *ca.* 80% (Zhu et al., 2013).

Figure 2.1: Figures created by blue emitting CD based ink (Zhu et al., 2013).

As a solvent water evaporates slowly and while drying, it maintains the structure and shape of the patterns. Instead of water, ethanol can also be used as a quick-drying and nontoxic solvent. Glycerol or water-soluble polymeric materials such as HEC (Hydroxyethyl cellulose) and PEG (Polyethylene glycol) can be used as a thickener and stabilizer to improve the ink's viscosity (Fu, 2021). This may stabilize particles to improve the loading content during application onto substrate also, the thick media avoids interaction between nanoparticles to avoid nonradiative energy transfer. Hydrophilic hydroxyl groups of the long chains of HEC, help to produce a homogeneous ink with aqueous CDs, having no effect on the fluorescence of material due to its transparent nature (Chen et al., 2019). PEG/HEC/glycerol concentration has a substantial effect on the viscosity of the ink.

A pH-dependent ink mixture was developed by Yang *et al.* from xylose, a carbohydrate, and m-PDA in acidified water, having multi-luminescent centers due to the presence of different chemical groups on its surface. However, N related (amine) surface defect states is the main reason for green emission. The aniline structure has a pKa of 4.6 thus, from pH 3-7 to pH 8-11 the CD surface gets deprotonated, and the emission changed from green to cyan due to the weakening of N related defect states and its corresponding luminescent centers. After printing a barcode figure onto filter paper and spraying with acid and base, it shows color switch from green to cyan respectively under UV light

excitation (Figure 2.2). This fluorescence reversibility was durable for 7 days (Yang et al., 2019).

(a) *(b)*

Figure 2.2: Barcode figure under UV light: (a) sprayed with dilute acetic acid, emitting green, (b) sprayed with dilute sodium hydroxide, emitting cyan (Yang et al., 2019).

CD based inks were continuing to be used in high level security printing for information storage and encryption (Anand, 2019). Fu *et al.* reported screen-printed and inkjet-printed, daylight invisible, pH-responsive Silicon-CD hybrid dots (0.64 wt% dispersion) on different substrates (Fu, 2021). By decreasing the pH from 10 to 2, the PL intensity of the CD decreases, accompanied by a redshift. They claim that the protonation of the surface amines leads to aggregation, resulting in PL quenching. This shows that the dispersion of the nanoparticles is pH responsive. But using hydroxyethyl cellulose (HEC) as binder prevents aggregation-induced CDs' quenching. [i] While the printed patterns emit cyan with hydrochloric acid vapor treatment, they recover and emit blue with ammonia vapor treatment under UV light. The applied patterns have fluorescence reversibility for over 30 times (Figure 2.3), without fading. While the printed patterns emit cyan with hydrochloric acid vapor treatment, they recover and emit blue with ammonia vapor treatment under UV light.

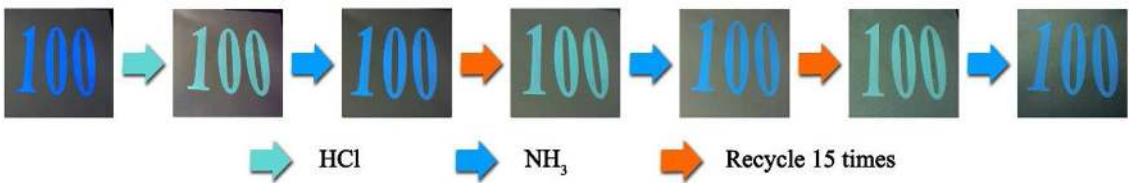

Figure 2.3: Fluorescent figure under UV light (Fu, 2021).

Later, Bhati *et al.* prepared a red-emitting Mg and N co-doped carbon dot, which had excitation independent emission at 667 nm (Figure 2.4) (Bhati, 2018).

Figure 2.4: Red-emitting fluorescent figures created by Mg-N co-doped CD ink (Bhati, 2018).

Lastly, fluorescent lifetime encoded CDs open a new path for the anticounterfeiting applications with luminescent materials in security inks. Kalytchuk *et al.* synthesized two CDs, from citric acid and ethylenediamine in water, at different reaction temperatures (220°C and 200°C) with the same emission properties. The synthesized CDs have fluorescence lifetime 13.2 ns and 7.9 ns, respectively for CDs_{slow} and CDs_{fast} in solution form. This difference between their PL lifetimes makes them suitable candidates for PL lifetime encoded security tag preparation. The CD-based inks were prepared by blending the two CDs with polyvinyl alcohol (PVA) as binders in 60, 200 and 400 ppm CD concentrations. Using different concentrations of these two types of CDs, a UV light visible "S" figure was written, decoded further by fluorescence lifetime imaging (FLI). In FLI mode, due to different fluorescence lifetimes of the synthesized CDs, the "K" figure was apparent (Figure 2.5) (Kalytchuk, 2018).

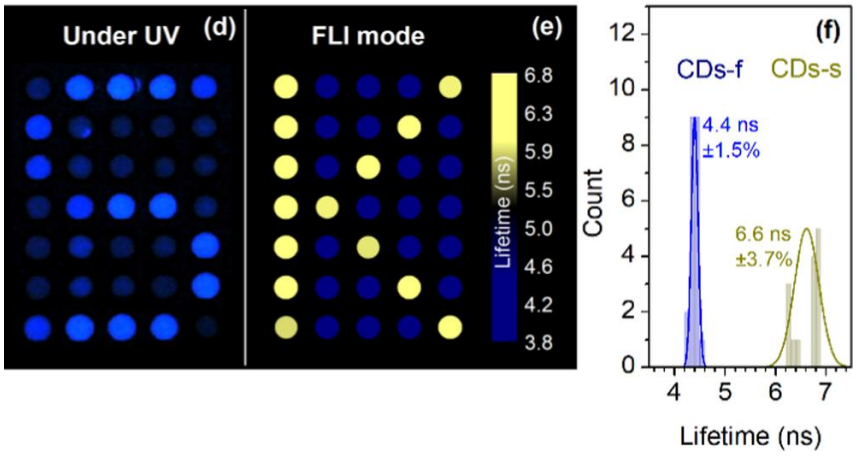

Figure 2.5: UV excitation and FLI mode encoded symbols (Kalytchuk, 2018).

2.1.2 Hydrophilic- Lipophilic Balance Index (HLB)

During preparation of aqueous CD ink mixtures, in addition to the carbon dots in water, some modifiers were used to adjust the hydrophilicity and hydrophobicity of the applied ink mixture. These are Span 80 and Tween 80 surfactants, as shown in Figure 2.6.

Surfactants are amphiphilic molecules containing hydrophilic and hydrophobic sections with usually alkyl groups with 8-22 carbons in their molecular structure (Nakama, 2014). Due to the oxo species, hydrophilic parts are soluble in water, whereas long alkyl chains are not soluble in water due to the hydrophobicity. Here, HLB Index of a surfactant expresses the balance of the hydrophilic-hydrophobic moieties. It has a range between 0-20. Surfactants with lower HLB are oil soluble (hydrophobic) and with higher HLB are water soluble. The HLB value of Tween 80 (Polyoxyethylene sorbitan mono-oleate) is 15 and HLB value of Span 80 (Sorbitan mono-oleate) is 4.3. As cited in Griffin et al., when emulsifiers are blended in different ratios (w:w) with respect to each other, HLB values are additive (Griffin, 1949). Span80 and Tween80 may be blended to afford a HLB index between 6-10, providing blends that are considered water dispersible. Below this HLB range the blend is hydrophobic (water in oil emulsion; w/o) and above is hydrophilic (oil in water emulsion; o/w).

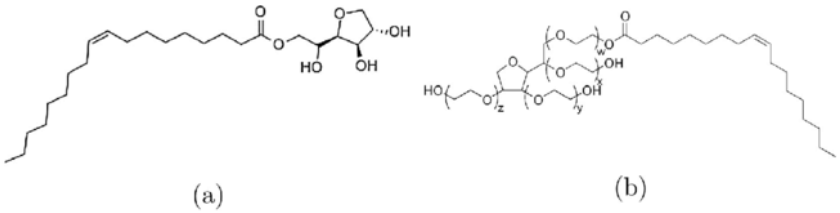

Figure 2.6: (a) Span80, (b)Tween 80 (Griffin, 1949).

2.1.3 Förster Resonance Energy Transfer (FRET)

FRET is a nonradiative energy-transfer process based on the dipole–dipole interaction (Lakowicz, 2006). When two materials are put in close distance with a proper orientation and if there is a spectral overlap between their emission and absorbance ranges, a nonradiative energy transfer occurs among these materials. One of these materials serves as a fluorescent donor and the other acts as an acceptor. The fluorescence

emission of the excited donor should match with the absorbance of the acceptor (West, 2018). The donor and acceptor can be accepted as dipole pair FRET tunneling from the excited donor to the acceptor brings an increase in the emission intensity of the acceptor and a decrease in the emission intensity of the donor. As can be seen in Equation 2.1, FRET efficiency (E) is inversely proportional to the sixth power of the distance (R) between donor and acceptor (Busnelli, 2013). Generally, the Förster distance is between 1.5 and 6.0 nm.

$$E = \frac{1}{1 + R^6/{R_0}^6}$$

Equation 2.1: FRET Efficiency Formula.

In the literature, different groups worked on forming FRET pair with CD nanoparticles as a fluorescent sensor probe. Chini *et al.* prepared CD-GQD pair and Wang *et al* prepared CD-Au nanoparticle pair (Chini et al., 2019 and Wang et al., 2019). In both studies, FRET efficiency was calculated as 30% and their TEM characterizations confirmed close enough spacing for FRET between the particles. Chini *et al.* mentioned that when GQD and CD solutions were prepared by simple mixing, GQD acts as a donor and CD acts as an acceptor, since the PL emission of the GQD overlaps with the absorbance of CD. Due to the FRET and nonradiative energy transfer from GQD to CD, the fluorescence of GQD was quenched by CD and the PL lifetime of the excited chromophore GQD decreased from 4.84 ns to 2.93 ns. The PL emission spectra of the FRET mixture contains a FRET peak, and a peak corresponds to the CD when excited at the absorbance maximum of GQD (Figure 2.7).

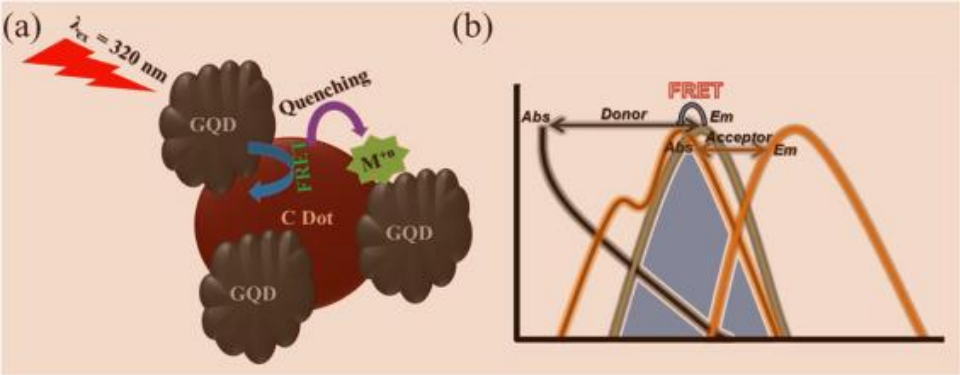

Figure 2.7: GQD-CD as FRET pair (Chini et al., 2019).

Wang *et al.*, followed a similar strategy with NCD-Au nanoparticles and this time N doped CD served as the FRET donor and Au nanoparticles as the acceptor through electrostatic interaction. This time, PL emission spectra of the FRET mixture contained two peaks that corresponds to the donor and the acceptor (Figure 2.8).

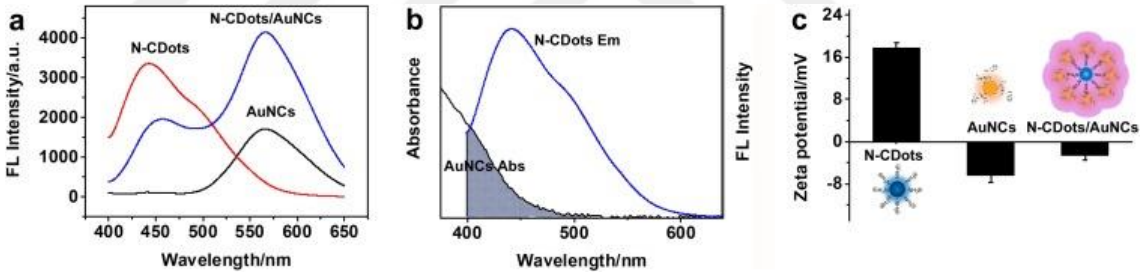

Figure 2.8: NCDs-AuNPs as FRET pair (Wang et al.., 2019).

However, spectral overlap between the emission and absorbance of the particles, is not always sufficient for FRET. Mandani *et al.* formed a composite by agglomerating the Rhodamine dye on the surface of CD particles by simple mixing, in which the dye molecules are electrostatically bind to the negatively charged CD surface. There is a spectral overlap between CD emission and RgB absorbance. At high enough concentration of the dye, the PL spectra of the composite showed the emission of both CD and the dye. However, increasing the RgB dye concentration in the composite, neither the emission intensity nor the PL lifetime of CD decreased, suggesting no FRET (Mandani, 2016).

2.1.4 The Proposal and Aim of the Thesis Work

In recent years, CDs have been under spotlight to provide sustainable nanotechnology in anticounterfeiting and security due to their unique and tunable optical, electronic, and chemical properties. They are used to develop hidden fluorescent inks and barcodes, which are hard to decode and back-engineer. Despite theory and several literature reports, developing a portfolio of CDs with a variety of emission colors, especially red, with strong emission intensity to create many optical barcodes is quite difficult. The practical materials are limited to mostly blue emitting CDs. The number of barcodes that can be written increases with the number of different colors emitted by different CDs. Hence, the purpose of this thesis project was to develop organic and water-soluble carbon dot nanoparticles that strongly emit light at different regions of the electromagnetic spectrum and maintain long term-stability to be used in security inks.

To fulfill the above objectives, all the CDs have been synthesized by the bottom-up synthesis approach, hydrothermal synthesis, as shown in Figure 2.9a. With the aid of temperature and pressure, precursor materials were first decomposed, then polymerized and lastly nucleated and grew to form carbon dot nanoparticles (Papaioannou, 2019), as shown in Figure 2.9b. Depending on the related carbon dot literature, to improve and/or redshift the emission of CDs, the chemistry of the C-precursors were varied to either change the conjugated carbon source or provide heteroatom doping (N, O, P).

Aromatic TNP, melamine and o- and p-PDA was used for N-doping, resorcinol was used for O-doping and phosphoric acid was used for P-doping in the design space. As non-aromatic compounds, PEI and maleic acid was used for N- and O-doping Table 2.1. Besides, post-synthetic modifications were studied on TNP-based CDs.

Table 2.1: List of Precursors:TNP (Wu, 2017), Melamine (Sigma Aldrich , 2021), Resorcinol (Sigma Aldrich , 2021), b-PEI (Sigma Aldrich , 2021) , o-PDA (Sigma Aldrich , 2021), p-PDA (Sigma Aldrich , 2021), phosphoric acid (Sigma Aldrich , 2021), Maleic acid (Sigma Aldrich , 2021)..

Precursor	Structure	N-doping	O-doping	P-doping
TNP	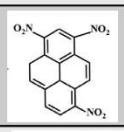	✓	✓	-
Melamine	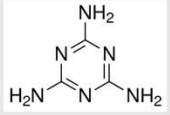	✓	-	-
Resorcinol	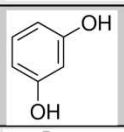	-	✓	-
Branched-PEI	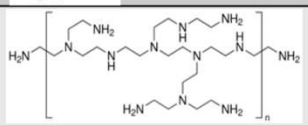	✓	-	-
o-PDA and p-PDA	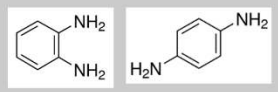	✓	-	-
Phosphoric acid	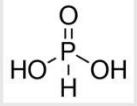	-	✓	✓
Maleic acid	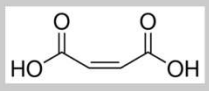	-	✓	-

In this study, CDs with four different emission colors, blue, cyan, yellow, and orange, were prepared to be used in inks and barcodes.

In the literature, there is a lack of organic carbon dot-based inks. This thesis can be viewed as a pioneering attempt to bridge the gap in developing organic soluble CD based inks and improve the aqueous CD tagged inks in terms of emission intensity, stability and number of possible barcodes

Developed aqueous CDs and organic soluble ones were used in aqueous and organic binders, to demonstrate their potential as fluorescent tags in such systems.

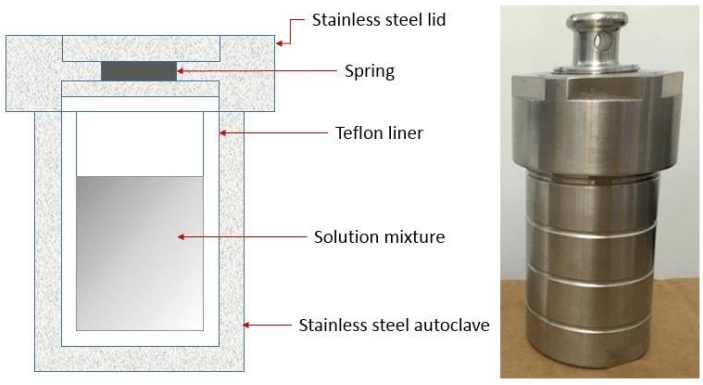

(a)

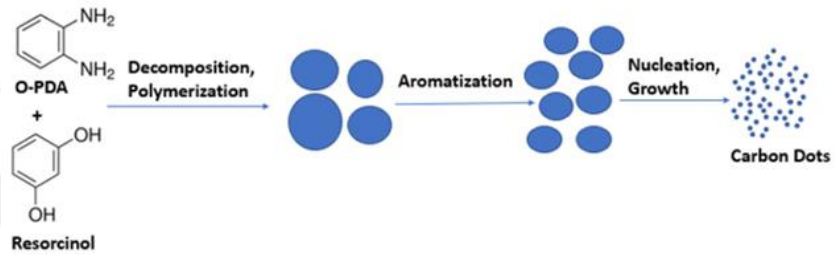

(b)

Figure 2.9:(a) Stainless Steel Autoclave (Wikipedia, 2016), (b) Carbon Dot Synthesis mechanism example.

CHAPTER 3 DEVELOPMENT OF CARBON DOTS FOR SECURITY INKS

While synthesizing organic and aqueous N, O, P doped CDs, we utilized different precursors to vary the color range of the synthesized CDs and specially to obtain red emitting CDs. Then we transferred the strong emitting ones to the ink.

3.1 Experimental

3.1.1 Materials

DMF and xylene were purchased from Merck (purity levels 99%, Darmstadt, Germany) and formamide was purchased from Biobasic (Canada). Hydrophilic PTFE filter (0.22 µm pore size, 25 mm diameter) was obtained from Chrom Fil. Dopamine, Resorcinol, Melamine, ortho phenylenediamine (o-PDA), para phenylenediamine (p-PDA) and Pyrene were obtained from Sigma Aldrich (Missouri, America). Branched Poly(ethyleneimine) solution (Mw 2000 kDa) and Maleic and Malonic acids were purchased by Sigma Aldrich (Missouri, America). Ortho-Phosphoric acid was obtained from Tekkim (purity levels 85%, Bursa, Turkey). Tetra ethylene glycol (TEG) and ethylene glycol (EG), sorbitan monooleate (Span 80) and Polyoxyethylene sorbitan mono-oleate (Tween 80) were provided by Sigma Aldrich (Missouri, America). All the reagents were analytical grade or highest purity.

3.1.2 Carbon Dot Nanoparticle Synthesis

3.1.2.1 Trinitropyrene based Carbon Dots

Synthesis of Trinitropyrene (TNP) as a Precursor

Trinitropyrene (TNP) is synthesized from pyrene in a 250 ml two neck round bottom flask. 20 ml concentrated sulfuric acid and 60 ml concentrated nitric acid is mixed in a

100 ml graduated cylinder and then poured onto 1.0 g pyrene, and the reaction was stirred for twenty-four hours at 80°C, 6000 rpm. After cooling down, the resulting TNP solution is poured onto 2000 ml room temperature distilled water, which is then filtered through a Buchner funnel to eliminate the unreacted pyrene precursor. TNP is washed with distilled water until the pH of the filtrate is adjusted to 5. TNP is dried in the oven.

TNP-Melamine (ss) CDs in xylene (CD01)

The N, O co-doped carbon dot is prepared by using TNP and Melamine as precursor materials and transformed into CDs without a solvent. 35 mg yellow TNP powder and 100 mg Melamine were mixed well in a 45 ml Teflon sealed autoclave reactor, then put into the oven at 180°C for 12 hours and became brownish yellow. To eliminate the byproducts, impurities and unreacted precursors, the CD (ss) is suspended in 10 ml cold ethanol and centrifuged in a 15 ml tube for 25 min at 5000 rpm for five times until the supernatant becomes colorless. Then the precipitate is collected and dried in the oven at 50°C, overnight. 20 mg CD is dissolved in 20 ml xylene (1000 ppm) and filtered from 0.22 µm PTFE syringe filter to eliminate the particles with larger size.

UV-Irradiated TNP-Melamine in xylene (AI-CD01)

TNP-Melamine CDs (CD01) in xylene was subjected to UV radiation for 1 h using a Rayonet containing 18 pieces of 11W UV (365 nm) lamp, as shown in Figure 3.1.

Figure 3.1: UV lamp.

3.1.2.2 bPEI based CDs

bPEI-Maleic acid CDs in water (CD24)

Similar to the synthesis procedure of Guo et al, 500 mg Maleic acid (solid, mp 130-135°C) and 500 mg 2 kDa bPEI (light yellow liquid, mp -16°C) have been dissolved in 13 ml water (Guo et al., 2019). This solution is transferred into 45 ml Teflon sealed autoclave reactor, then put into the oven at 180°C for 10 hours, after reaction the solution changed its color from light yellow into brown. Product was obtained as powder in solution form and used without further purification.

3.1.2.3 Resorcinol Based CDs

Resorcinol-oPDA in DMF (CD22)

460 mg Resorcinol (solid, mp 110°C) and 270 mg o-PDA (solid, mp 100-102 °C) have been dissolved in 25 ml DMF to prepare N, O co-doped CD. This solution is placed into 45 ml Teflon sealed autoclave reactor, then put into the oven at 180°C for 10 hours. After the reaction is completed, the solution was filtered through 0.22 µm PTFE syringe filter to eliminate the large size particles. Solvent was removed under vacuum and a gel-like structure has left behind. This structure can't be dissolved in ethanol to be centrifuged. CDs were used without further purification.

Resorcinol-pPDA in water (CD18)

368 mg Resorcinol (solid, mp 110°C) and 216 mg pPDA (solid, mp 138-143 °C) have been dissolved in 20 ml acidified water (with 2 drops of HNO_3). This solution is placed into 45 ml Teflon sealed autoclave reactor, then put into the oven at 200°C for 8 hours. After the reaction is completed, there was no change in color and, the solution was filtered through 0.22 µm PTFE syringe filter to eliminate the large size particles. CDs were miscible with ethanol, so the CDs were used without further purification.

Resorcinol-pPDA(ss) in DMF (CD29)

Resorcinol (solid, mp 110°C) and pPDA (solid, mp 138-143°C) was also transformed into CDs without a solvent and placed in a 45 ml Teflon sealed autoclave reactor, then put into the oven at 200°C for 8 hours, after the reaction the color of the solution has turned into black. 3 mg CD was dissolved in 3 ml DMF (1000 ppm) and filtered from 0.22 µm PTFE syringe filter.

Resorcinol-Melamine in DMF (CD12)

368 mg Resorcinol and 120.4 mg Melamine have been dissolved in 20 ml DMF and treated at 200°C for 8 hours in 45 ml Teflon sealed autoclave reactor. After the reaction was completed, the color was pale pink. The solution was passed through 0.22 µm PTFE syringe filter. The carbon dot solution was mixed with ethanol and centrifuged at 6000 rpm for 20 minutes to precipitate the CDs. Recovered CDs were added to ethanol and centrifuged one more time, then dried in vacuum oven.

3.1.2.4 Preparation of Aqueous Carbon Dot based Ink

During the preparation of such inks, some viscosity and hydrophilicity/hydrophobicity modifiers were used. The viscosity modifiers ethylene glycol (EG) and tetra ethylene glycol (TEG-viscosity increaser due to longer chain) were completely soluble in water. Span 80 was hydrophobic, and Tween 80 was hydrophilic surfactants, having HLB values of 4.3 and 15, respectively. [Span 80/Tween80] ratio was used as 4:3 (w:w) to fix the HLB index of the emulsifier blend to 8.9, which is between 6-10 on HLB scale and assumed as water-dispersible. During the preparation of a transparent binder 2 g EG, 1.5 g TEG, 0.4 g Span80 and 0.2 g Tween80 were added. Then 4 ml aqueous CD solution was added onto the prepared binder, covering the rest with distilled water up to a total of 10 g ink mixture. The prepared aqueous CD based ink mixture was shaken well with vortex and then either filled to an empty pen or to the cartridge of an inkjet printer to apply the ink mixture on paper. All the CD based ink

mixtures were prepared according to this recipe and applied onto paper, measured by 405 nm (blue) and 525 nm (green) sensors.

3.1.2.5 Preparation of Organic Carbon Dot based Ink

CDs suspended in organic solvents were loaded into a commercial binder consisting of ethyl and buthyl acetate and cyclohexanone or in commercial transparent nail polish, in different concentrations.

3.1.2.6 Preparation of Organic Carbon Dot Mixture-based Solution

1000 ppm carbon dot solutions were mixed in different ratios (w:w), by keeping the total nanoparticle amount the same, to form CD mixtures. These mixtures were diluted then UV Absorbance and PL measurements were performed. This procedure was repeated three times by preparing new CD mixtures to calculate the standard deviation for each combination. The ratio of the PL emissions intensities received at 405 nm and 525 nm excitations were determined.

3.1.2.7 Preparation of Organic Carbon Dot Mixture-based Ink

1000 ppm CDs were loaded in the same ratios (w:w) to the commercial nail polish then applied onto a non-fluorescent paper and dried at dark. This procedure was repeated three times by preparing new CD mixtures to calculate the standard deviation for each combination. The emission intensities of the CD mixture-based inks were tracked by 405 nm and 525 nm sensors. The ratio of the PL emissions intensities received at 405 nm and 525 nm excitations were determined.

3.1.3 Characterization

Carbon dots were characterized by means of morphological, structural and optical properties using various analytical methods. Absorbance spectra of CDs in the range of 300-800 nm was determined from their solution by using Shimadzu UV-vis spectrometer. Hydrodynamic particle size and distribution and charges were determined by using a

Malvern ZS-Zetasizer. Size and morphology of the CDs were determined by transmission electron microscope (Hitachi HT7800 and Hitachi HF5000), with an accelerating voltage 100 kV. Fast Fourier Transform (FFT) was performed on HRTEM images, giving the diffraction pattern of the region of interest. Measurements were performed using 500 ppm CDs solutions dropped on a C-coated Cu grid. Functional group analysis of CDs was performed by Fourier Transform Infrared Spectroscopy (Thermo Scientific iS10 FT-IR) in the range of 600-4000 cm^{-1} using the dried samples. To detect the differences in chemical bonds and oxidation state of corresponding elements in CDs high resolution X-ray photoelectron spectroscopy spectrum (XPS-Thermo Scientific K-Alpha) was recorded for C1s, N1s and O1s energy levels of CDs with Al Kα (1486.3 eV) monochromatic radiation. The sp^3 C was set to 284.5 eV as a reference signal. The crystallographic structure of materials was determined by X-Ray Diffractometer (XRD-Bruker D8 Advance) between the angles 10-90° with an operating voltage of 40 kV and Cu Kα radiation (λ=1.54 Å). The photoluminescence emission characteristics of particles were determined by Photoluminescence Spectroscopy (PL- Horiba Fluorolog-3) in the range of 300-800 nm. The Photoluminescence Quantum Yield (QY) and Time-Resolved Fluorescence (PL Lifetime) was measured by Edinburgh Instruments FLS1000 Spectrometer. For QY measurements the sample is diluted into a concentration with an absorbance below 0.1-0.05. QY was measured with an integrating sphere by dividing the area under the PL curve of sample to solvent. The PL Lifetime was measured by 377 nm excitation source.

3.2 Results and Discussion

3.2.1 Synthesis of Carbon Dots

3.2.1.1 TNP-based Carbon Dots

Hydrothermal synthesis of TNP in xylene was developed by our partner Quantag A.Ş TNP is a conjugated precursor material, providing both N- an O-doping to the carbon skeleton or surface/edges of the carbon dot. Unsaturated cyclic carbon molecules are preferred for CDs synthesis to provide more sp^2 domains and fully conjugated network.

TNP-CDs synthesized in different solvents display different optical properties. TNP-CD in xylene looks orange, whereas TNP-CD in water is yellowish green under 365 nm UV light. As can be seen in Figure 3.2, under 420 nm excitation TNP in xylene emitted light at longer wavelength (586 nm) with the highest emission intensity with respect to CDs produced in DMF and water, with increasing polarity.

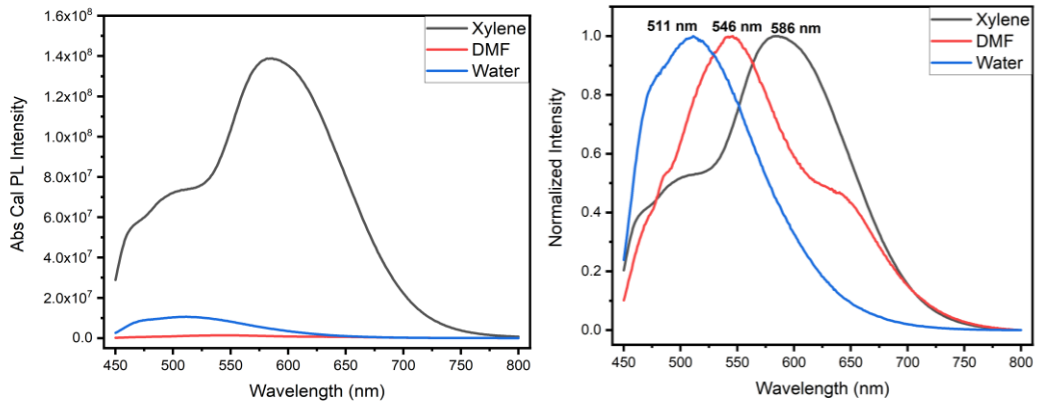

(a) *(b)*

Figure 3.2:(a) Photoluminescence spectra of TNP-CDs synthesized in different solvents (b) normalized PL spectra of these TNP-CDs. Excitation wavelength is 420 nm.

Since N-doping is suggested to red shift the emission wavelength of CDs (Geng, 2018), branched polyethyleneimine (b-PEI, 2 kDa) was added to the current TNP-CD recipe. The b-PEI, as shown in Figure 3.3.a, is a polymer containing branched ethylene diamine groups as repeating units with lone pair electrons on nitrogen atoms. However, b-PEI is completely saturated and lacks conjugated double bond structures. Besides, Hu *et al.* suggested that b-PEI produces blue emitting CDs (Figure 3.4) (Hu et al., 2014). Overall, TNP-bPEI based CDs displayed blue emission under UV excitation, suggesting that branched PEI as a N-dopant was not successful in shifting the emission to longer wavelengths.

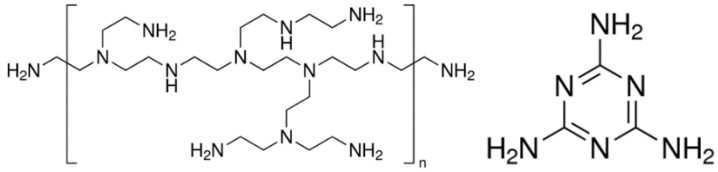

(a) *(b)*

Figure 3.3: Chemical structures of amines: (a) Branched Polyethyleneimine (Sigma Aldrich , 2021), (b) Melamine (Sigma Aldrich , 2021).

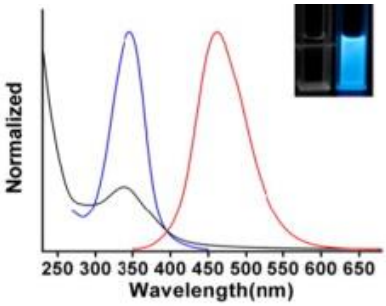

Figure 3.4: Black line: Normalized UV-vis Absorption, Blue line: Normalized Excitation at 360 nm, Red line: Normalizied Emission at 460 nm, image in the upper right corner represents day and UV light colors

(Hu et al.,2014).

Next, an alternative N-dopant with an aromatic triazine structure, melamine, was added to TNP recipe (Figure 3.3.b). Melamine provides both conjugated sp^2-sp^2 N and C atoms along with primary aromatic amines. Melamine was hydrothermally reacted with TNP in solid state to improve the nitrogen doping to the sp^2 domains of carbon skeleton and to obtain redshift in emission. TNP-Melamine CDs were dissolved in different solvents such as water, xylene and DMF. Except water, TNP-Melamine was soluble in xylene and DMF (Figure 3.5.a and Figure 3.5.b), and emit yellow and green respectively under UV light. This behavior is called as solvochromic effect. In different solvents with the changing dielectric constant of the medium (water having the highest dielectric constant), Van der Waals interactions and H-bonding between the CD surface and surrounding changes and cause changes in the emission characteristics.

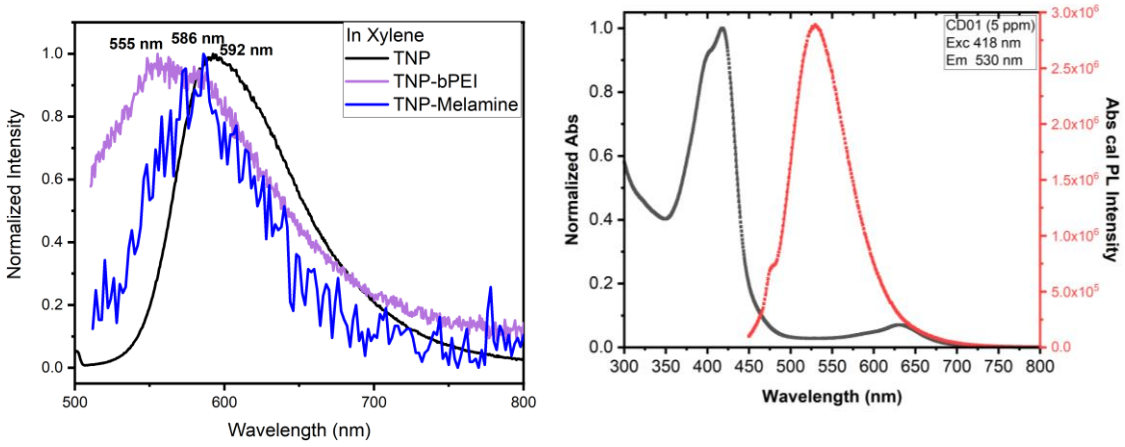

(a) *(b)*

Figure 3.5: (a)Normalized Photoluminescence spectra comparison of TNP derivatives in xylene. Excitation wavelength: 500 nm, (b) Normalized Photoluminescence spectra of TNP-Melamine in DMF. Excitation wavelength: 418 nm.

Overall, N-doping of TNP-CD with b-PEI downshifted the emission peak from 592 to 555 nm, and to 586 nm with melamine at 500 nm excitation with reduced intensity. Under UV light, the color of the TNP-CD, TNP-melamine and TNP-bPEI in xylene are orange, yellow and blue, respectively (Figure 3.6).

Figure 3.6: Color change under UV light for: TNP, TNP-Melamine, TNP-b-PEI in xylene.

Yet, at least at the studied ratios, neither b-PEI nor melamine caused a red-shifted emission of the TNP-CD but starting with TNP and using b-PEI or melamine, three different colored CDs were obtained.

Overall, TNP- Melamine in xylene was used in the rest of the studies as yellow emitting CDs.

3.2.1.2 B-PEI based CDs

As mentioned in the previous section, blue emitting aqueous CDs can be synthesized from b-PEI (Figure 3.4). Addition of conjugated structures can help to shift the emission to longer wavelengths. Therefore, maleic acid with C=C bond (Guo, 2019) was added to the synthesis of CDs from b-PEI, which also brought in O-atoms and for comparison another dicarboxylic acid which lacks C=C bond, malonic acid, was also tested as an O-dopant (Figure 3.7). Although malonic acid introduces more oxygen dopant (0.019 moles) rather than maleic acid (0.017 moles), b-PEI-maleic acid CDs emit cyan and b-PEI-malonic acid CDs emit blue under UV light (Figure 3.8b). Due to doping less oxygen to carbon skeleton and having a more conjugated structure, in other words having more electron delocalization in the system, maleic acid was found to be a better red shifter with respect to malonic acid recipe. Under 380 nm excitation, emission maxima of b-PEI-malonic acid CD was 489 nm and the broad emission maxima of b-PEI-maleic acid CDs was 552 nm, with 4.5 times reduction in emission intensity (Figure 3.8a).

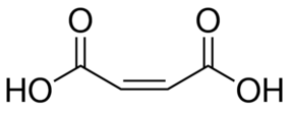

(a)

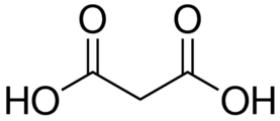

(b)

Figure 3.7: Chemical structures of: (a) Maleic acid (Sigma Aldrich , 2021), (b) Malonic acid (Sigma Aldrich , 2021).

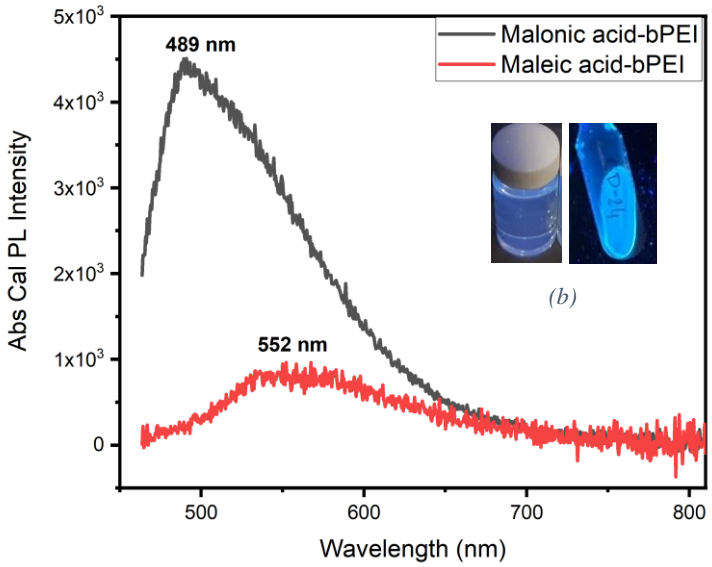

(a)

(b)

Figure 3.8: (a) Photoluminescence spectra comparison of Malonic acid –bPEI and Maleic acid –bPEI in water. Excitation wavelength: 380 nm, (b)UV light images of bPEI-Malonic acid CD and bPEI-Maleic acid CDs, respectively.

Overall, b-PEI/Maleic acid in water was used in the rest of the studies as cyan emitting CDs.

3.2.1.3 Green to Red Dot

Jiang *et al.* synthesized blue, green and red emitting carbon dots from m-PDA, o-PDA and p-PDA (C and N sources), respectively, in ethanol (Jiang et al.,2015). Phenylenediamine (PDA) is an aromatic molecule with two primary amine groups, hence, nucleophilic lone pair electrons and electron deficient C-atoms. In the literature, o-PDA and p-PDA, as shown in, are accepted as green and red emitters respectively. Based on the studies of Jiang *et al* and Lin *et al*., CDs from o-PDA and p-PDA were prepared here in DMF (Jiang et al., 2015 and Lin et al., 2017). Although, green-yellow and red emissions were reported in the mentioned references for CDs synthesized in DMF solvent, we have obtained green and orange emissions under UV light from o-PDA and p-PDA based CDs (Figure 3.10b). DMF was used as reducing agent to create more lone pairs before fusion and having a higher amount of conjugation during the synthesis. Emission maxima of o-PDA and p-PDA CDs in DMF were at 521nm and 572 nm at 400nm excitation, with 10 times decreasing intensity (Figure 3.10a).

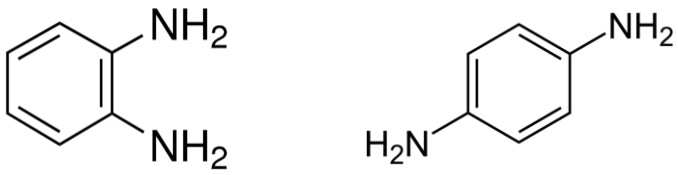

(a) *(b)*

Figure 3.9: Chemical structures of phenylenediamine derivatives: (a) o-PDA, (b) p-PDA.

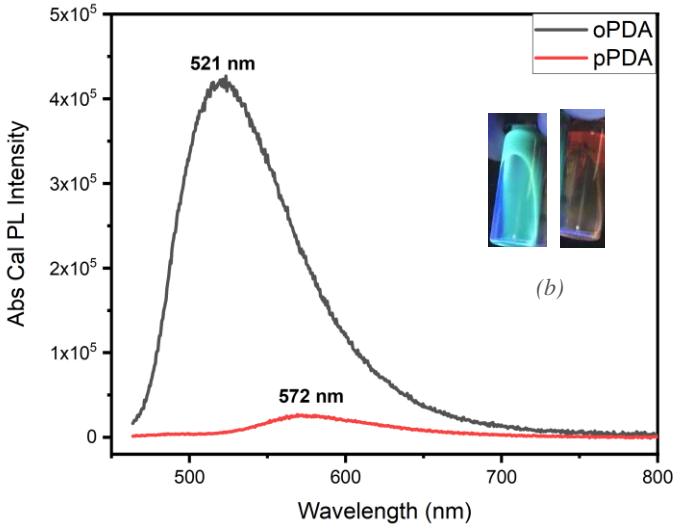

(b)

(a)

Figure 3.10: (a) Photoluminescence spectra comparison of o-PDA and p-PDA in DMF. Excitation wavelength:400 nm, (b) UV light images of o-PDA and p-PDA CDs, respectively.

3.2.1.4 Modifications on the Route to Red Dot

o-PDA / Dopamine CDs

Depending on the previous results with phenylenediamine molecules, o-PDA is combined with Dopamine in acidified water (Lu, 2017). Dopamine (Figure 3.11a) is an aromatic molecule containing O and N atoms. In our case, under 432 nm excitation, emission with a peak maximum at 523 nm was obtained (Figure 3.12a). However, in the reference, under 425 nm excitation, emission with a peak maximum at 710 nm and a shoulder at 665 nm was obtained (Figure 3.13a). Moreover, in our case white emission under 365 nm light was obtained (Figure 3.12c), whereas red emission was obtained in

reference article (Figure 3.13b). The difference in emissions might result from the acid type (in the literature HCl and in our case HNO_3 was used) that was used in the pH adjustment of the reaction mixture and transferring the CDs into ethanol to take their PL emission in the reference article. Repeating the same recipe in DMF instead of water gave yellowish green emission (Figure 3.12d). Indeed, absorbance and emission profile of these CDs in water and DMF were very similar (Figure 3.12.b). Dopamine-oPDA in water might contain CDs with different emissions due to different band-gap sizes (different particle sizes) or various surface functional groups but Dopamine o-PDA in DMF might not contain such differences. This might lead to their different emissions under UV light excitations. Although the reaction time of Dopamine-oPDA in DMF CDs (8 hours) was different than oPDA in DMF CDs (4 hours), with the addition of Dopamine into recipe, under UV light there is a shift from green to yellowish green. Dopamine might result in a CD with a larger conjugated sp^2 domain.

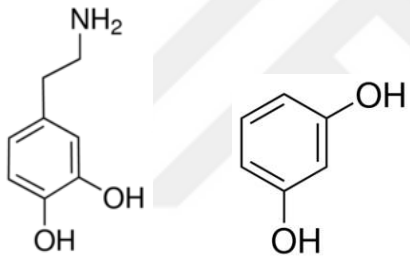

(a) *(b)*

Figure 3.11: Chemical structures of: (a) Dopamine (Sigma Aldrich , 2021), (b) Resorcinol (Sigma Aldrich , 2021).

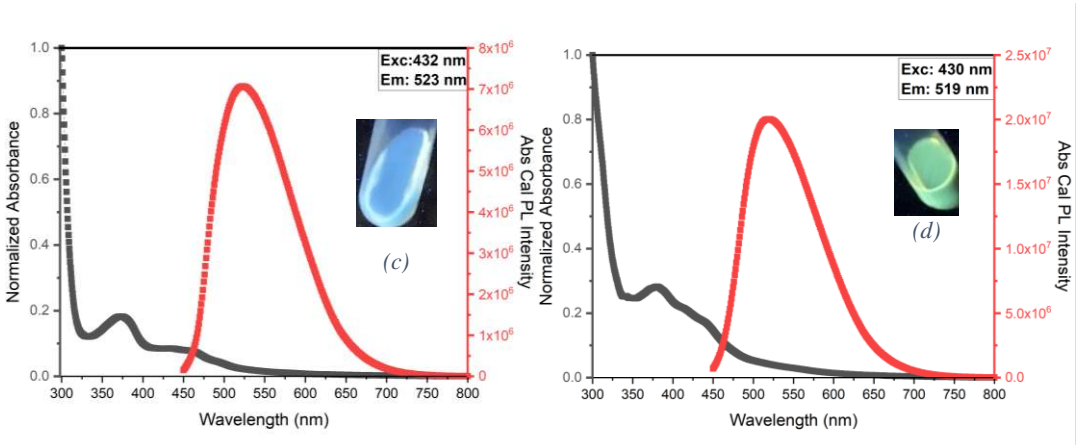

(a) *(b)*

Figure 3.12: Photoluminescence spectra of Dopamine- oPDA in: (a) water. Excitation wavelength: 432 nm, (b) DMF. Excitation wavelength: 430 nm, (c) UV light image of Dopamine-oPDA in water, (d) UV light image of Dopamine-oPDA in DMF.

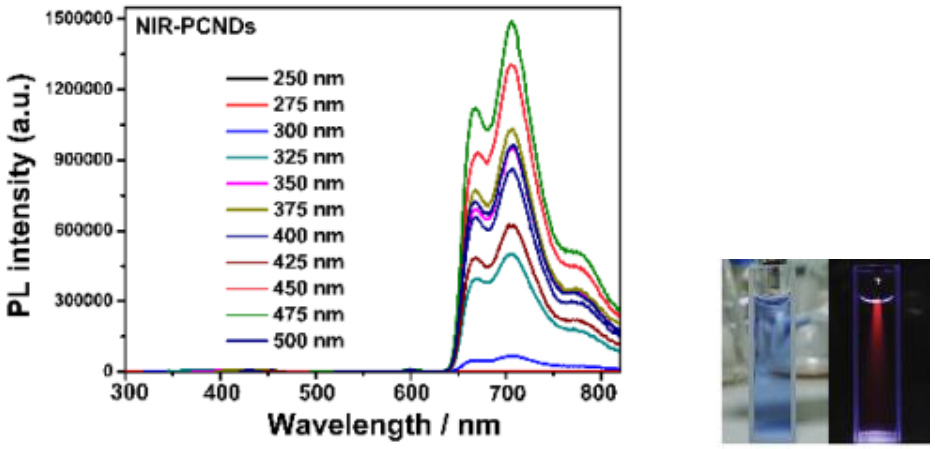

(a) *(b)*

Figure 3.13: (a) Photoluminescence spectra of NIR-PCNDs under different excitation wavelengths, (b) Day and UV light images of NIR-PCNDs.

o-PDA/Resorcinol CDs

As an alternative to Dopamine, Resorcinol (Figure 3.11b) which is also an aromatic diol without the amine, was tested in aqueous o-PDA recipe. This provided yellow emitting CDs under 365 nm UV light, which indeed shifted the o-PDA-CD emission to longer wavelength.

Same recipe was repeated in DMF and formamide instead of water because DMF and formamide were expected to act as reducing agent and increase the lone pair electrons, increase graphitic nitrogen, and lead a redshifted emission. Reaction in DMF provided a yellow emissive CD with a dramatically stronger intensity and formamide provided blue emissive CDs (Figure 3.14). Emission peak maxima shifted from 569 nm to 518 and 472, respectively for water, DMF and formamide. In DMF recipe, more electrons were excited to higher energy levels and then fluoresce during electron-hole recombination, thus resulted in a superior emission intensity.

Overall, o-PDA/Resorcinol in DMF was used in the rest of the studies as yellow emitting CDs.

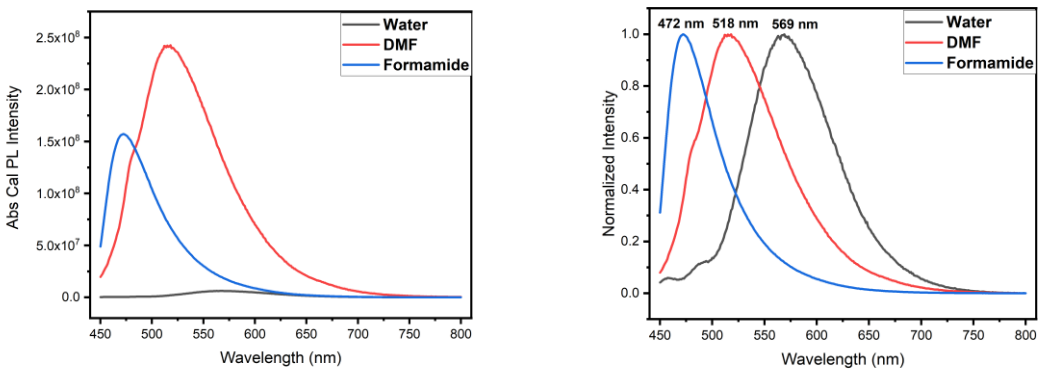

(a) *(b)*

Figure 3.14: Resorcinol- o-PDA in different solvents: (a) Photoluminescence spectra, (b) Normalized Photoluminescence spectra. Excitation wavelength: 400 nm.

Despite higher N/O ratios provided in Dopamine-o-PDA in DMF (1.3) than Resorcinol-o-PDA in DMF (0.60), both CDs had similar emission profile. This explains that aliphatic amine group in the Dopamine doesn't provide further integration and graphitization and Resorcinol is a good substitute of Dopamine.

p-PDA/Resorcinol CDs

As it was mentioned previously, p-PDA is known as red-shifter in the literature. Thus, p-PDA/Resorcinol based CDs were also produced in several solvents: water, (solid state synthesized and then suspended in) DMF, formamide. In formamide it has the most intense, red-shifted, and broadest PL emission peak at 607 nm (Figure 3.15). The broad emission lines suggest that it might contain different color emissive CDs, emitting blue under UV light. Whereas, in DMF and water, it has weaker bluish white emission (Figure 3.15c), respectively at 452 nm and 422 nm.

Overall, compared to p-PDA in DMF, addition of Resorcinol leads to a blueshift from 572 nm to 452 nm.

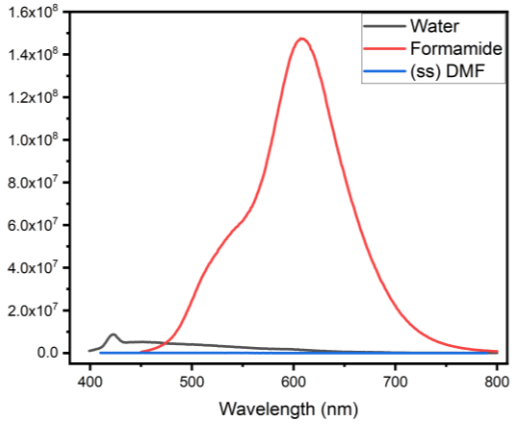

(a)

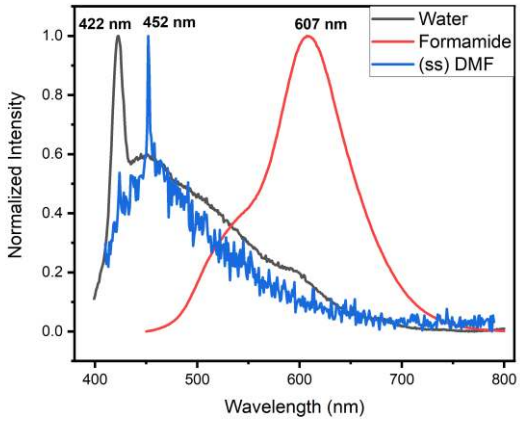

(b)

(c)

Figure 3.15: Resorcinol- p-PDA in different solvents: (a) Photoluminescence spectra, (b) Normalized Photoluminescence spectra. Excitation wavelength:400 nm, (c) UV light images of CDs in DMF, water, formamide, respectively.

Since Resorcinol-p-PDA CDs in water was seem bluish white under UV light, the excitation dependent emission of these CDs was investigated. As shown in Figure 3.16a, dominant luminescent center of CDs has changed under different excitations. Similar study was performed with a Fluorescence Microscope using different excitation/emission filters to separate the emissions from the CDs at different channels. Under 404, 465, 519,

561 and 673 nm excitations, CD18 was emitting from violet to red, (Figure 3.16b, c, d, e, f, g). This suggests that like in many examples in the literature, fractionation of CDs via column chromatography may fractionate the as synthesized CDs into CDs that emit light in different parts of the EMR spectrum with different emission colors.

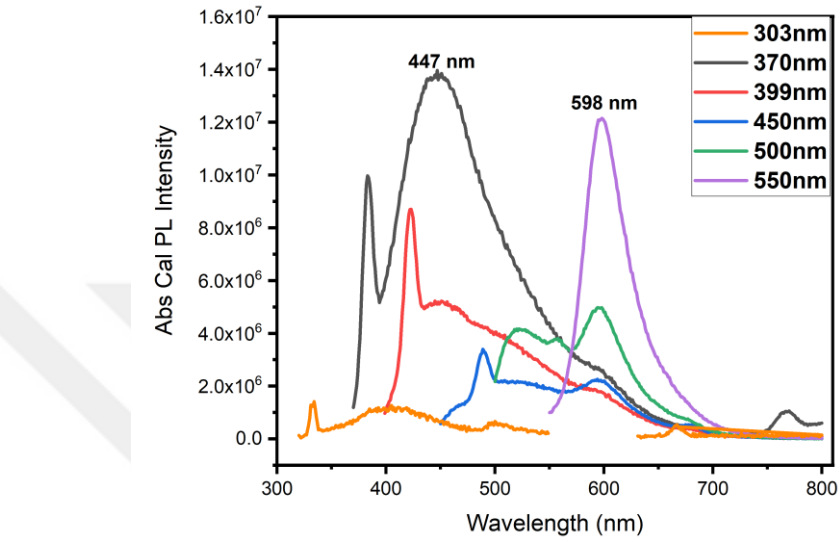

(a)

(b) *(c)* *(d)* *(e)* *(f)*

Figure 3.16: Resorcinol- p-PDA in water: (a) Photoluminescence spectra in different excitation wavelengths; FL Microscope images (b) violet, (c) blue, (d) green, (e) orange, (f) red.

Overall, p-PDA/Resorcinol in water was used in the rest of the studies as bluish white emitting CDs.

Melamine-based CDs

As an alternative to aromatic phenylenediamines, melamine with aromatic N-atoms and three amine substituents, was tested. Melamine was combined with Resorcinol in DMF to improve the nitrogen doping of the conjugated carbon skeleton. The as-synthesized CD has excitation-dependent emission with decreasing intensity (Figure 3.17a) from blue to red.

Melamine and the red-shifter p-PDA was also tested. p-PDA/Melamine CDs were prepared in DMF, having excitation independent emission at 583 nm (Figure 3.17e). Addition of Melamine to p-PDA lead to a shift from 572 nm to 583 nm (Figure 3.17c), due to the π–π stacking and H-bonding among precursor molecules.

Overall, p-PDA/Melamine in DMF was used in the rest of the studies as yellow emitting CDs (Figure 3.17d) and Resorcinol/Melamine in DMF as bluish white emitting CDs (Figure 3.17b).

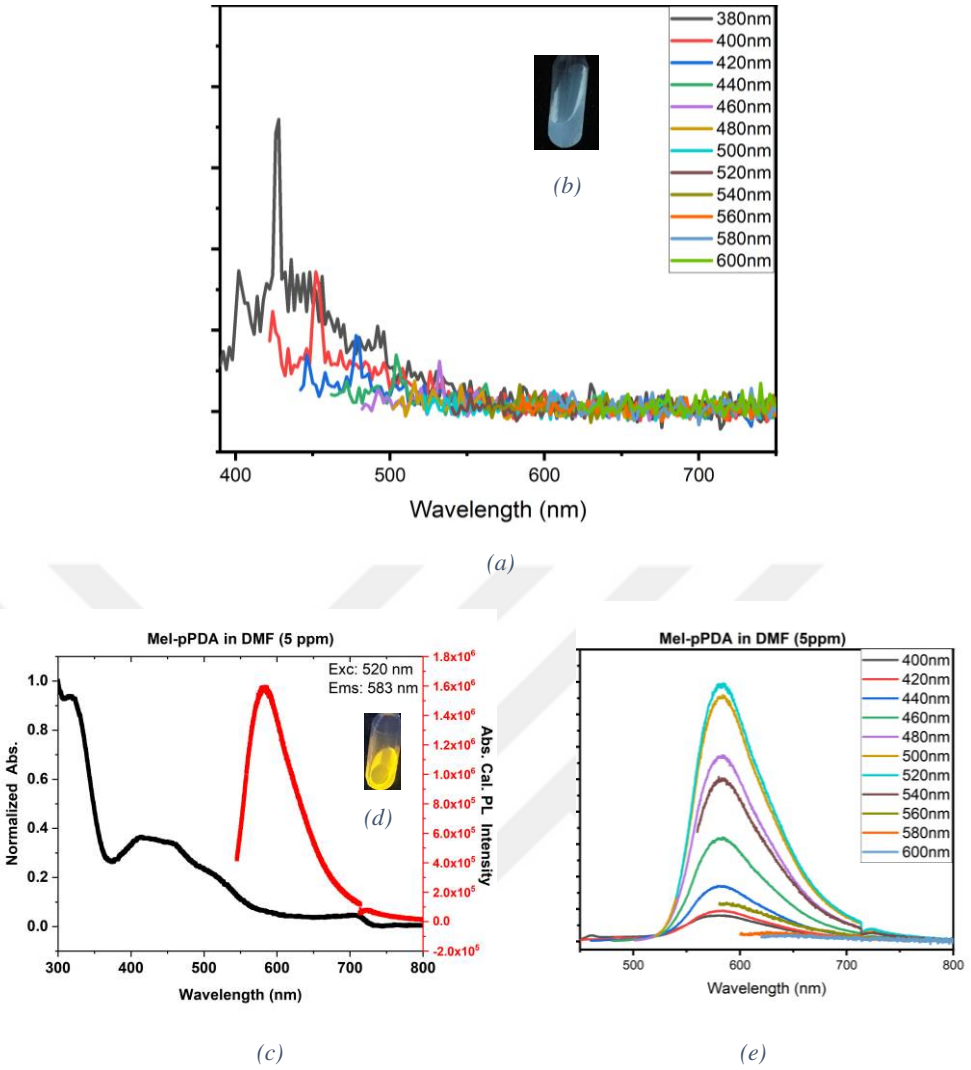

Figure 3.17: (a) Excitation Dependent Photoluminescence spectra of Resorcinol-Melamine in DMF CDs, (b) UV light image of Resorcinol-Melamine CDs, (c) Photoluminescence spectra of Melamine- p-PDA in DMF. Excitation wavelength: 520 nm, (d) UV light image of Melamine-p-PDA CDs, (e) Excitation Dependent Photoluminescence spectra of Melamine-p-PDA in DMF CDs.

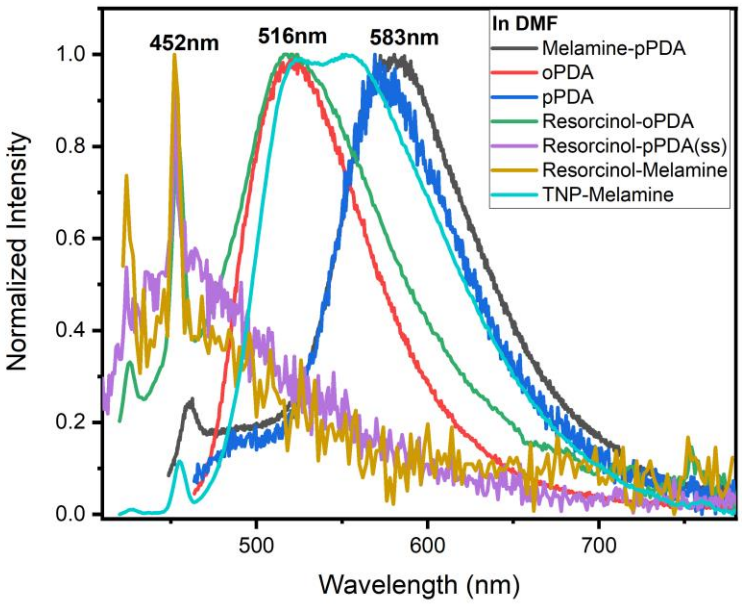

Figure 3.18: Normalized Photoluminescence spectra comparison of different CD recipes in DMF. Excitation wavelength: 400 nm.

As can be seen in Figure 3.18, the particles that were either directly synthesized in DMF or after solid state synthesis dissolved in DMF, were compared to understand the logic in varying the precursors on the route to the red dot. Under 400 nm excitation both p-PDA and Melamine-p-PDA recipes have similar emission profiles (572 nm and 583 nm respectively), indicating that addition of a conjugated amine source "Melamine" into the p-PDA in DMF recipe yielded a little redshifted emission with an increasing intensity. After the synthesis of Resorcinol-o-PDA in DMF, we developed the idea that combining the conjugated molecule Resorcinol, either with p-PDA or Melamine would lead to a redshift in emission than the Resorcinol-o-PDA recipe by knowing that p-PDA was known as red shifter also p-PDA in DMF emitted at a longer wavelength than o-PDA in DMF recipe (521 nm and 572 nm respectively). However, Resorcinol-p-PDA (ss) and Resorcinol-Melamine recipes emitted nearly at 452 nm and Resorcinol-o-PDA emitted at 516 nm. We assumed that the spatial orientation / conformation of Resorcinol was more favorable with o-PDA rather than p-PDA and Melamine in terms of having better integration and conjugation sites during the molecular fusion step of carbon dot synthesis. Moreover, three sets with similar structures were compared, these were TNP-Melamine and Resorcinol-Melamine; Resorcinol-o-PDA and o-PDA; Resorcinol-p-PDA (ss) and p-

PDA. These comparison for each set showed that adding or altering one molecule in recipe with Resorcinol led to a broader emission line (larger FWHM). Resorcinol has resulted in excitation wavelength dependent emission, creating oxygen doping related defects. For TNP-Melamine and Resorcinol-Melamine, Resorcinol-p-PDA (ss) and p-PDA sets addition of Resorcinol has blue-shifted the emission, but for Resorcinol-o-PDA and o-PDA it leads to an increase in emission intensity rather than a shift.

3.2.1.4 Red Dot

As shown in Figure 3.19c, depending on the related literature, only by changing the acid from H_3PO_3 to H_3PO_4, p-PDA was synthesized in acidified water, providing phosphor and oxygen doping (Chen et al., 2017). CDs emitted red under UV light (Figure 3.19b). In the related literature and in our reaction condition (Figure 3.19a) the N/O ratio was 0.031 and 0.024, respectively, leading only a little change in emission point.

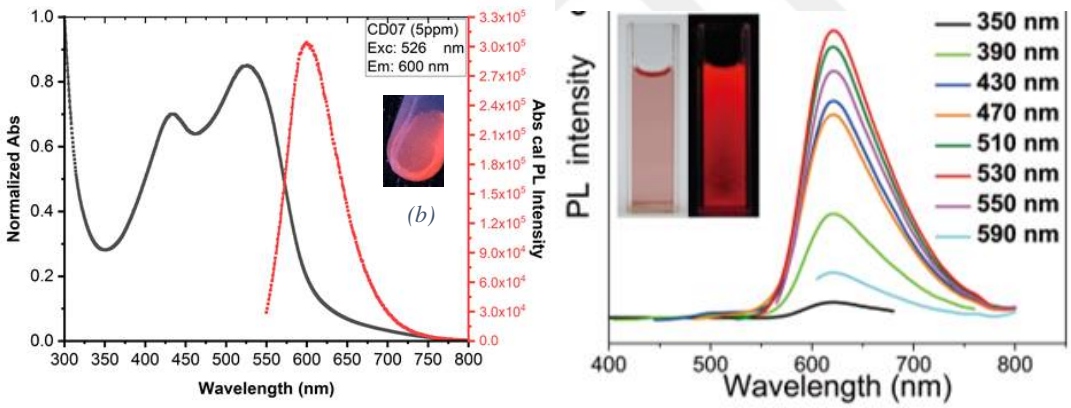

Figure 3.19: (a) Photoluminescence spectra of p-PDA-phosphoric acid in water. Excitation wavelength: 526 nm, (b) UV light image of CDs, (c) Photoluminescence spectra of p-PDA-phosphorous acid in water (Chen et al., 2017).

The hydrothermal synthesis conditions of each of the above-mentioned particle was summarized in Table 3.1. The carbon dots that were either used in aqueous or organic based ink preparation have been mentioned in 3.1.2 Carbon Dot Nanoparticle Synthesis, in detail. The rest of the particles were given to highlight the design path of CDs synthesis.

Table 3.1: Synthesis recipes of different carbon dots.

PRECURSORS	SOLVENT	REACTION TEMPE_ RATURE (°C)	TIME (hour)	COLOR UNDER UV LIGHT (365nm)
TNP	Xylene	180	16	Orange 
TNP	Water	180	16	Yellowish green
TNP-bPEI	Xylene	220	10	Blue 
TNP-Melamine (ss)	Xylene	180	12	Yellow 
TNP-Melamine (ss)	DMF	180	12	Green 
Maleic acid-bPEI	Water	180	10	Cyan 
Malonic acid-bPEI	Water	180	10	Blue 
oPDA	DMF	180	12	Green 
pPDA	DMF	180	12	Orange 
Dopamine-oPDA	Water	200	8	White 
Dopamine-oPDA	DMF	200	8	Yellowish green 
Resorcinol-oPDA	Water	200	8	Yellow
Resorcinol-oPDA	DMF	200	8	Yellow 
Resorcinol-oPDA	Formamide	200	8	Blue 
Resorcinol-pPDA	Water	200	8	Bluish-white 
Resorcinol-pPDA	Formamide	180	10	Blue 
Resorcinol-pPDA(ss)	DMF	200	8	Bluish-white 
Resorcinol-Melamine	DMF	200	8	Bluish-white 
Melamine-pPDA	DMF	200	8	Yellow 
pPDA-phosphoric acid	Water	180	24	Red 

Among the above particles organic soluble CD01, CD12, CD22, CD29, CD33 and water soluble CD18 and CD24 were ideal candidates. It was observed that they have emission in different parts of the electromagnetic spectrum. Apart from the single CD-based security inks, some organic CDs emitting different colors were combined in different ratios to create CD mixture-based optical barcodes. The emission color of CD01 under 365 nm light was yellow. To investigate the effectiveness of the after treatments in improving the emission property, the 1000 ppm CD01 solution was UV light irradiated and the CD surface was photo-modified.

3.2.2 Comparison of CD01 and AI-CD01 Particles

In the TEM analysis, CD01 nanoparticles are noticeable as dark spots (Figure 3.20.a), which were nearly spherical. The reduced FFT image of CD01 (Figure 3.20.b) is deprived of a well resolved ring structure, indicating poor crystalline or amorphous nature (Asghar, 2017). Spherical AI-CD01 particles appeared in Figure 3.20.c, and Figure 3.20.d showed the presence of a nonperiodic arrays.

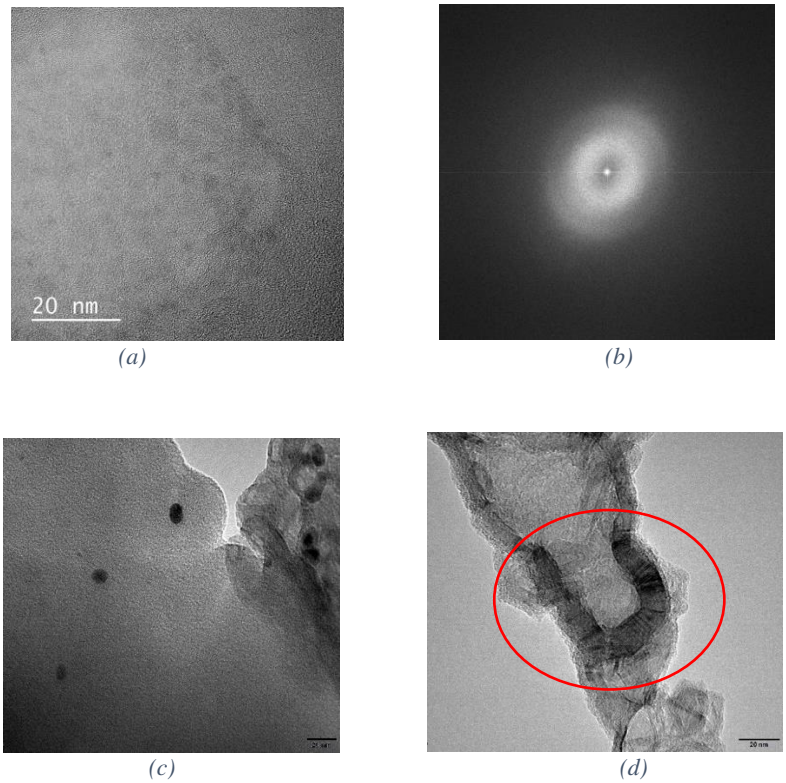

Figure 3.20: (a) TEM image of CD01, (b) Reduced FFT image of CD01, (c) and (d) TEM images of AI-CD01.

The synthesis method displays an important role in terms of crystallinity. Different parameters such as synthesis technique, time and temperature affect the crystal formation. As cited in the Raman spectrum of the related literature, increasing the reaction time provided higher level of crystallinity (Papaioannou, 2019). As an after treatment, the UV light irradiation might modify the size, shape or chemical structure of CD01.

In the XRD of CD01 there are some peaks between 20°-30° (Figure 3.21.a) and in AI-CD01 there is a sharp peak at 28.7° (Figure 3.21.b), indicating the diffraction of 002 plane of graphite (Wang, 2019). There wasn't a broad hump confirming the XRD pattern of amorphous carbon (Siddique, 2018). While both particles' TEM images (Figure 3.20) provided amorphous nature, their XRD spectrum provided crystallinity (Figure 3.21). This explained the coexistence of crystalline and amorphous nature. There are less diffraction peaks in the XRD spectra of AI-CD01 than CD01. The reason might be less defined crystal structure but more importantly containing more defects.

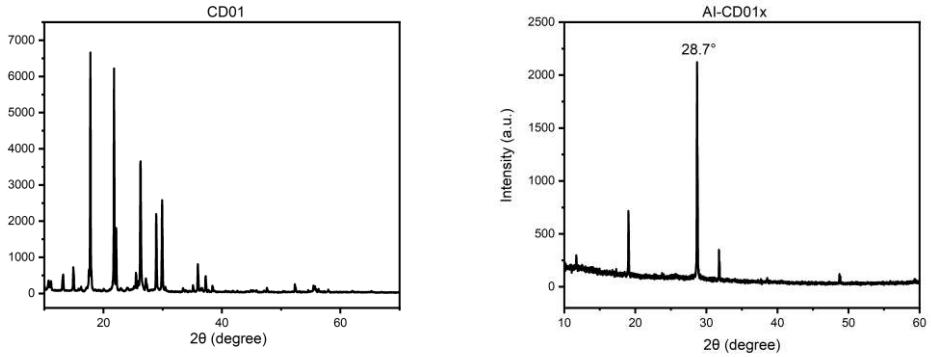

(a) *(b)*

Figure 3.21:XRD images: (a) CD01, (b) AI-CD01.

Based on the DLS results in Table 3.2, the number based hydrodynamic size of CD01 was 6.52 nm. The intensity based hydrodynamic sizes were 28.1, 246.2 and 3667 nm. All the CD solutions were filtered through 0.22 µm PTFE filter and particles larger than its pore size couldn't get through. It is important to note that the scattering intensity is directly related to the sixth power of the radius. Despite the larger sized aggregates or dust occupy a lower percentage, due to the higher scattering intensity, they appeared in the intensity- based distribution. The number based hydrodynamic sizes of AI-CD01 were

3.60 nm (and 41.36 nm)[1] and the intensity based hydrodynamic sizes were 3.99 nm (and 52.25 nm)[1], which agreed with the scale of the TEM images (Figure 3.20.c,d). After UV irradiation due to changes on CDs surface, the interaction of the nanoparticles with its surrounding has changed. We predicted that the decrease in the nanoparticle size, via UV irradiation, resulted from the increase in the surface defect sites.

Table 3.2: DLS comparison of CD01 and AI-CD01.

Sample Name	PDI	Size Distribution by Number (nm)	Size Distribution by Intensity (nm)
CD01	0.309	6.52±2.17	28.1±20.2
AI-CD01	0.723	3.60±0.595 (and 41.36±8.93)[1]	3.99±0.539 (and 52.25±11.2)[1]

The FTIR spectras of CD01 and AI-CD01 were stacked (Figure 3.22), to observe what did the UV light irradiation cause in the molecular structure of CD01. It is important to mention that some common peaks corresponding to bond streching or bending remained quantitatively in the same strength (%transmisttance) in both samples, nevertheless some of the bonds has either changed their strength or formed/destroyed during the phototreatment.

[1] The sizes with a superscript (1) correspond to the last measurement among three subsequent size measurements. The first two measurements have agreed on the sizes as stated in table.

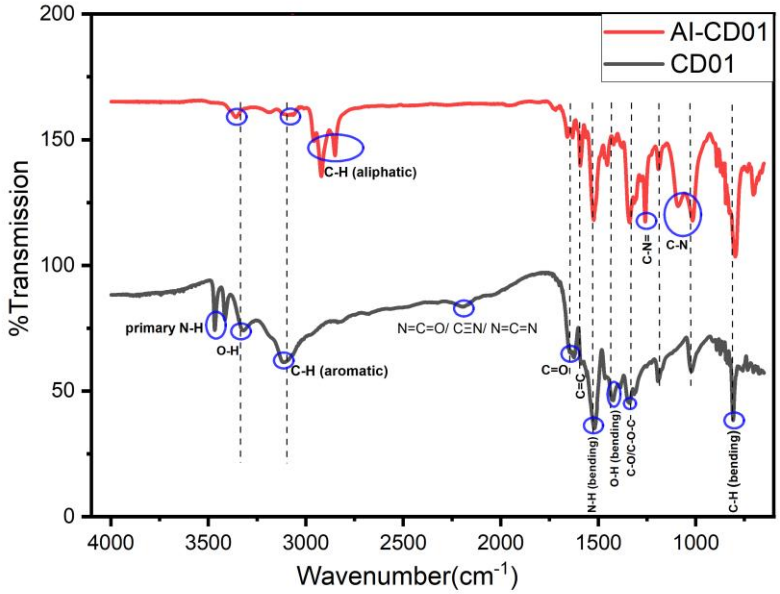

Figure 3.22: FTIR comparison of CD01 and AI-CD01.

In Figure 3.22, FTIR provides confirmatory evidence on the presence of the C-O streching vibrations peak at 1339 cm^{-1}. After irradiation the strength of C-O bonds have increased. At 1620-1650 cm^{-1}, there are two peaks corresponding to C=O bond streching of carbonyl, carboxyl or amide group (Han, 2020). The two peaks at 1592 and 1454 cm^{-1} are characteristic benzene ring vibrations (C=C), corresponding to the sp^2 skeleton and they increased after irradation. The two peaks at 1016 and 1092 cm^{-1} are C-N streching vibrations of either pyrrole, amine or amide (Naghshbandi, 2020). Three peaks at 808, 1423 and 1518 cm^{-1} were attributed to the C-H, O-H and N-H bendings, respectively (Chandra, 2014). The C-N= bond stretching at 1340 cm^{-1} has formed after irradiation. In AI-CD01, peaks around 2800-2900 cm^{-1} resulted from the hydrogens of the methyl groups (aliphatic C-H) which are attached to the benzene ring, coming from xylene. CD01 has vibrations at 3113 cm^{-1}, 3320 cm^{-1} and two bands at 3414 and 3467 cm^{-1}, respectively corresponding to =C-H, O-H and two primary amine asymmetric stretches. At 2185 cm^{-1} CD01 has a streching corresponding to C≡N or N=C=N or N=C=O, which is diminished in AI-CD01 (Sigma Aldrich , 2021).Going from CD01 to AI-CD01, the number of =C-H and O-H bonds were decreased also N-H bonds were destroyed.

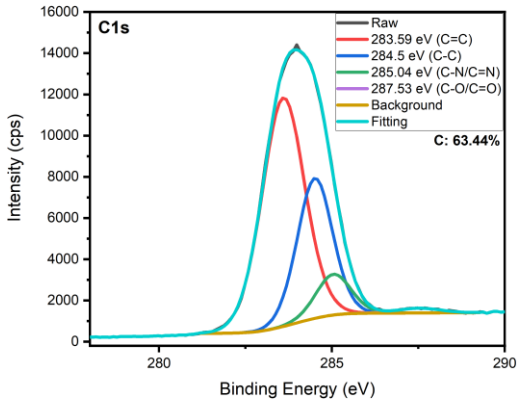

(a)

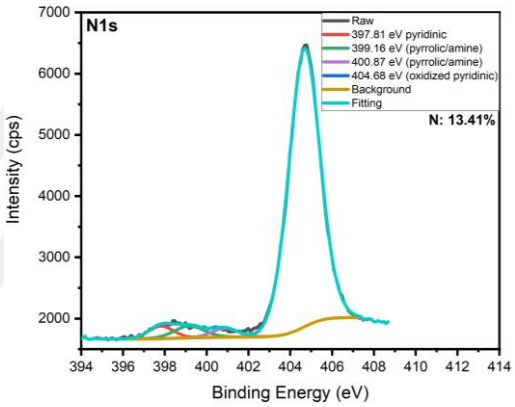

(b)

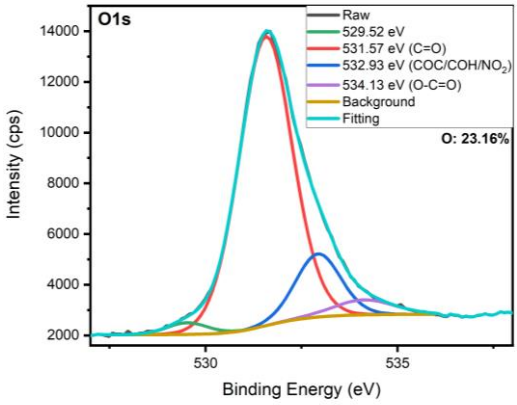

(c)

Figure 3.23: XPS analysis of TNP: High resolution spectrum of (a) C1s, (b) N1s, (c) O1s.

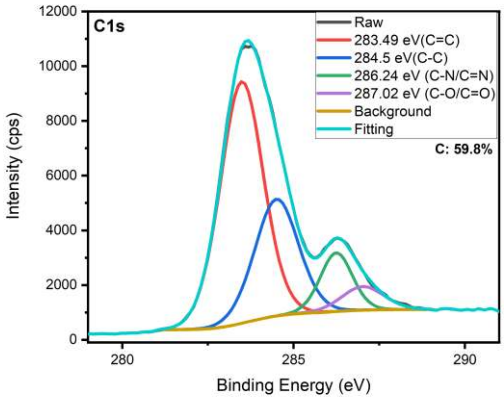

(a)

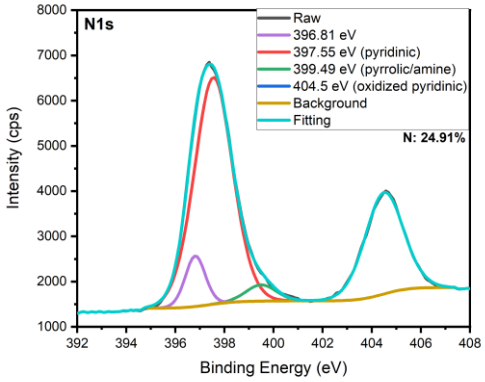

(b)

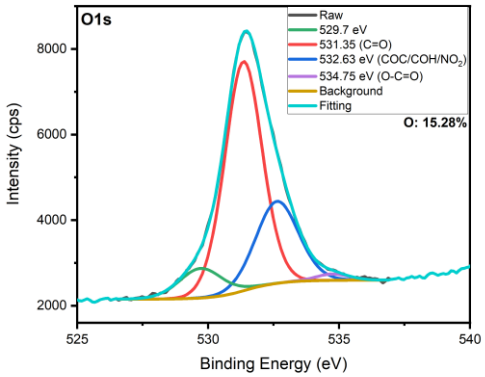

(c)

Figure 3.24: XPS analysis of CD01: High resolution spectrum of (a) C1s, (b) N1s, (c) O1s.

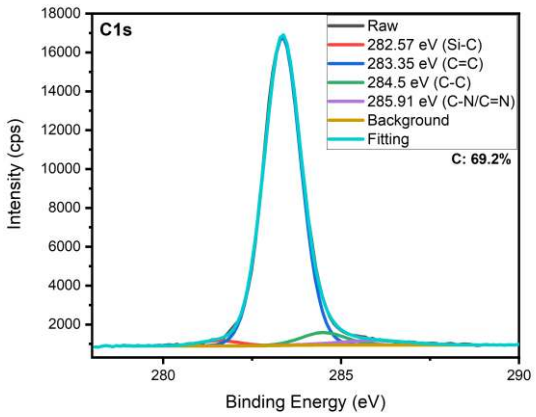

(a)

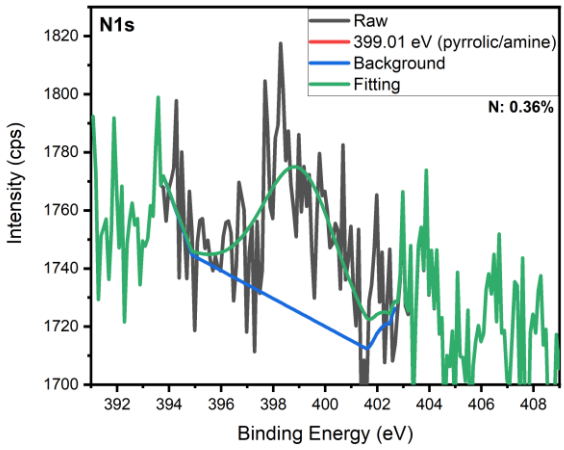

(b)

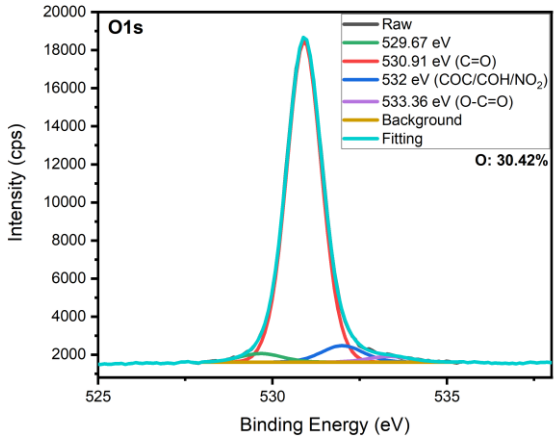

(c)

Figure 3.25: XPS analysis of AI-CD01: High resolution spectrum of (a) C1s, (b) N1s, (c) O1s.

The surface functional groups and chemical composition of CDs were further enlightened by high resolution XPS spectrum of C1s, N1s and O1s. The XPS spectrum of the precursor TNP, the synthesized CD01 and AI-CD01 was shown in Figure 3.23, Figure 3.24, Figure 3.25, respectively. The atomic percent of each element was shown in the corresponding spectrum. (Permatasari et al., 2016 and Khan et al., 2017)

The N-doping concentration of TNP precursor was 21.1% and has increased to 41.7% for the synthesized CD01. Then the N concentration decreased into 0.52%. Meanwhile, starting from precursor TNP to CD01 and to AICD01, the O-doping concentration changed from 36.5 %, 25.6% and to 44%. This indicates that through hydrothermal reaction of precursor TNP with Melamine, the nitrogen atoms on Melamine have successfully incorporated into CD01 structure. After 1 hour irradiation most of the nitrogen has turned into oxygen. Going from CD01 to AI-CD01, the 3.4-fold decrease in the C-N/C=N in C1s spectra (~285 eV) and 2.8-fold increase in the C-O/C=O in O1s spectra (~531 eV) confirms the oxidation degree of AI-CD01 was higher CD01, meaning that there are more oxygen related defects in AI-CD01 (Khan et al., 2017). It is assumed that UV light irradiation acts as the continuation of the CD synthesis process. As CD solution was irradiated for one hour, the interaction between the CDs proceeded to grow the conjugated sp^2 domain and increase the C=C graphitization (~283 eV), which is already confirmed by FTIR, while decreasing sp^3 C-C/C-H (284.5 eV) (Papaioannou, 2019). Meanwhile the deconvolution of the high resolution N1s spectra of CD01 and AI-CD01, shows the decrease in the nitrogen related defects from four different peaks into one peak at ~399 eV (Figure 3.24.b and Figure 3.25.b) (Matsoso et al., 2016 and Qu et al. 2014 and Rabchinskii et al., 2020). The weakening of that N-H peak from CD01 to AI-CD01 indicates that there is less amount of amine group on the surface of AI-CD01 (Figure 3.25.b), which was already confirmed by their FTIR (Figure 3.22). Also, the deconvolution of the high resolution O1s spectra of both particles, shows a peak at ~534 eV corresponding to carboxylate group (O=C-O) (Figure 3.24.c and Figure 3.25.c) (Emrooz, 2021). The carboxylate has strengthened from CD01 to AICD01. The strengthening of the carboxylate/carbonyl group and the weakening of amine group brought the idea that some amides (O=C-N) on the CD01 surface has turned into carboxylate during UV irradiation.

In the literature, there is not a consensus on the photo-modification of carbon dot's structure. Like Tan *et al.*, the first time example of photochemical oxidation of CDs, our findings indicate that the carbonyl bonds (C=O) increased after UV irradiation, assuming that the number of oxygen related defect energy trapping (DET) states in between HOMO-LUMO levels increased (Tan et al., 2014). Meanwhile very current research by Stepanova *et al.*, confirmed the PL intensity enhancement after the photo-irradiation (Stepanova, 2021). In another study by Li *et al.*, due to photoreduction of the CD surface, PL emission intensity in visible region decreases and in UV region increases with a blueshift (Li X. Y., 2019). As opposed to our results, they claimed that surface functional groups of the carbon dot (C=O, C-O and O-H) were decreasing in number due to photoreduction.

To learn more about the optical properties of the materials, UV Absorbance and Photoluminescence measurements were performed. To determine the emission characteristics of CD01 and AICD01, the emission under different excitation wavelengths was measured. It was recorded that under 480 nm excitation wavelength CD01 gave the emission with highest intensity at 565 nm whereas under 520 nm excitation wavelength AI-CD01 gave the emission with highest intensity at 596 nm. The day light and UV (365 nm) light images appeared as yellow and orange respectively for CD01 and AI-CD01. The emission intensity of the CD01 continued to increase up to 9 weeks however emission intensity of AI-CD01 increased more than 9 weeks. In Figure 3.26, a closer look to the UV-vis absorbance spectrum of CD01 and AI-CD01 showed a redshift from 416 nm to 481 nm after irradiation of CD01 solution. The 2.8-fold increase in carbonyl groups (C=O) and increase in carbonyl related defect energy trapping states lead to a stronger interaction between the excited $\pi^*_{(C=O)}$ and $n_{(O)}$. Due to this stronger interaction between $\pi^*_{(C=O)}$ and $n_{(O)}$ and having a larger sp^2 domain (C=C) resulted in a narrower bandgap and a prominent redshift in absorbance of the AI-CD01.

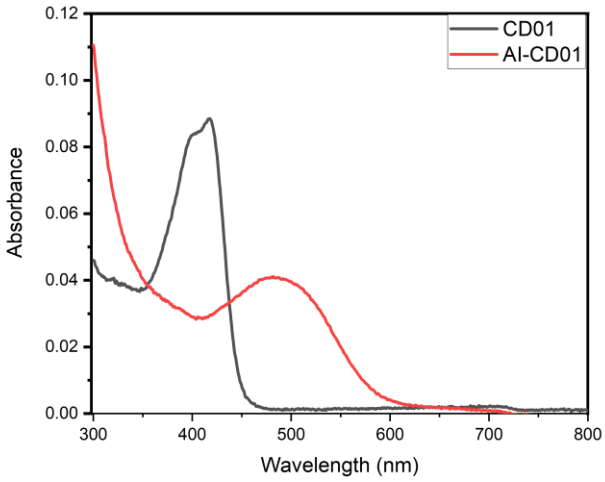

Figure 3.26: UV Absorbance comparison of CD01 and AI-CD01.

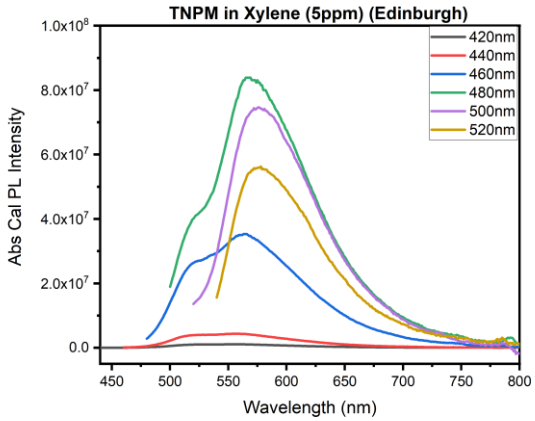

(a)

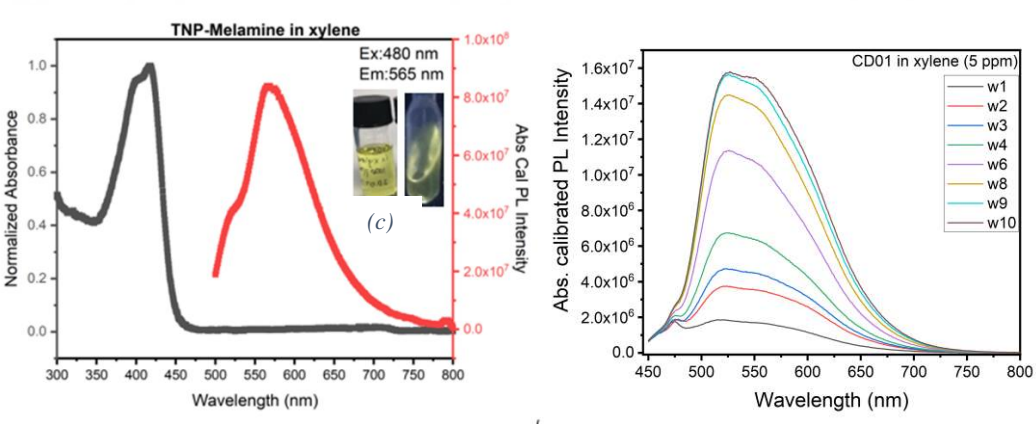

(c)

(b) *(d)*

Figure 3.27: TNP- Melamine in xylene (CD01): (a) PL under different excitation wavelengths, (b) PL. Excitation: 480 nm, (c) Image under day and UV light respectively, (d) PL stability

Table 3.3: Fluorescence Lifetime of CD01.

Sample Name	Emission Point (nm)	Major Event (%)	Decay Time (T1) (ns)	Minor Event (%)	Decay Time (T2) (ns)	Average Decay Time (ns)
CD01	426	67.56	1.24	32.44	4.93	2.44
	520	67.42	2.2	32.58	4.39	2.91

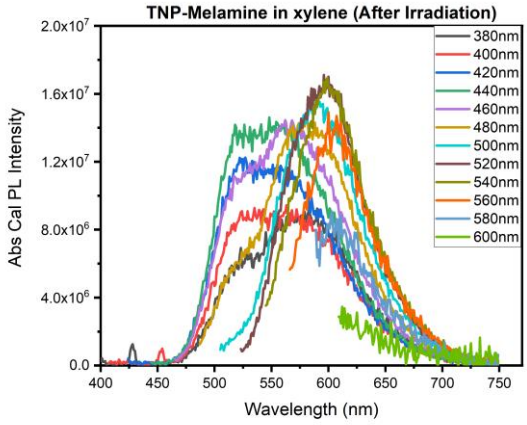

(a)

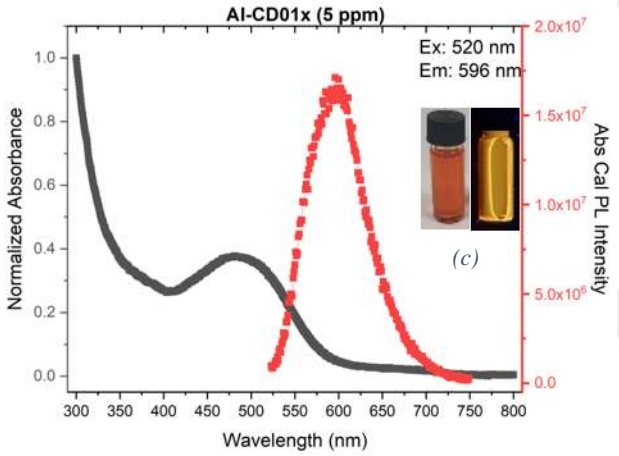

(c)

(b)

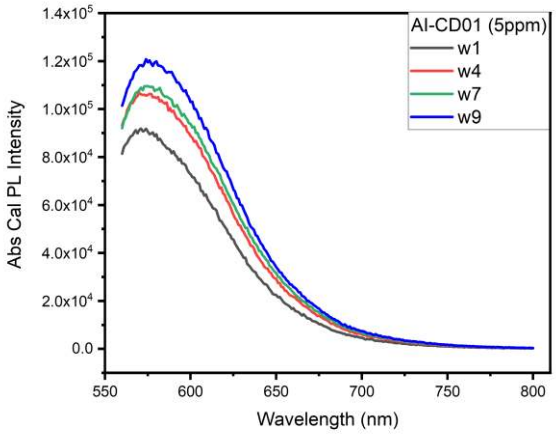

(d)

Figure 3.28: AI- CD01: (a) PL under different excitation wavelengths, (b) PL. Excitation: 520 nm, (c) Image under day and UV light respectively, (d) PL stability.

Table 3.4: Fluorescence Lifetime of AI-CD01.

Sample Name	Emission Point (nm)	Major Event (%)	Decay Time (T1) (ns)	Minor Event (%)	Decay Time (T2) (ns)	Average Decay Time (ns)
AI-CD01	520	57.89	4.27	42.11	2.09	3.35

CD01 has a Quantum Yield of 8.18% between 545-577 nm and 2.1% in broader range between 545-637 nm. These slightly low Quantum yields result from the absence of a further surface passivation process. AI-CD01 has a QY of 41.6% between 537-709 nm. Containing higher amount of oxygen atom than CD01, leads to higher electron density in n energy level (n_O) and higher electron delocalization in conjugated sp^2 domain. In other words, the number of charge carriers, that will recombine will be more than CD01, resulting in higher QY.

Time Resolved Fluorescence of CD01 was measured at 426 and 520 nm, shown in Table 3.3 and of AICD01 was measured at 520 nm, shown in Table 3.4, by using 377 nm resource. Double exponential line was fitted to the decay curve. By observing the fluorescence average lifetime change from 2.91 ns (CD01) to 3.35 ns (AI-CD01) and the change in the major PL decay event from faster decay to slower one, it is obvious that there occurred a PL mechanism change with photooxidation. The radiative decay of the particles has two contributors: fast decaying direct band to band transition (aromatic core/carbon skeleton) and slow decaying indirect surface/defect state transition (Gómez, 2021). As it was previously mentioned, the XRD spectra of AI-CD01 (Figure 3.21.b) contains less diffraction peaks, meaning AI-CD01 has more defect sites. In this case we assume that the PL emission of CD01 has the major contribution (67.42%) from fast excitonic band to band transition (2.2 ns) and minor contribution (32.58%) from the slow and indirect recombination through surface/defect states (4.39 ns). AI-CD01 has the major contribution (57.89 %) from slow and indirect recombination through surface/defect states (4.27 ns) and minor contribution (42.11%) from fast excitonic band to band transition (2.09 ns).

To summarize the optical behaviors of CD01 and AI-CD01 in detail, both particles and the reference red particle of Quantag were excited in two different wavelengths, these

are 400 and 520 nm respectively, shown in Figure 3.29. As can be seen from the figures, under 400 nm excitation AI-CD01 has ~10-fold higher emission intensity than CD01 and reference particle. Under 520 nm excitation AI-CD01 still had superior emission intensity than CD01 meanwhile having a closer emission intensity to the reference particle. These CDs and reference particle were further used as security tags and their emissions were measured by optical sensors having 405 nm and 525 nm source, which was discussed in section: Security Tag Applications of Organic based CDs.

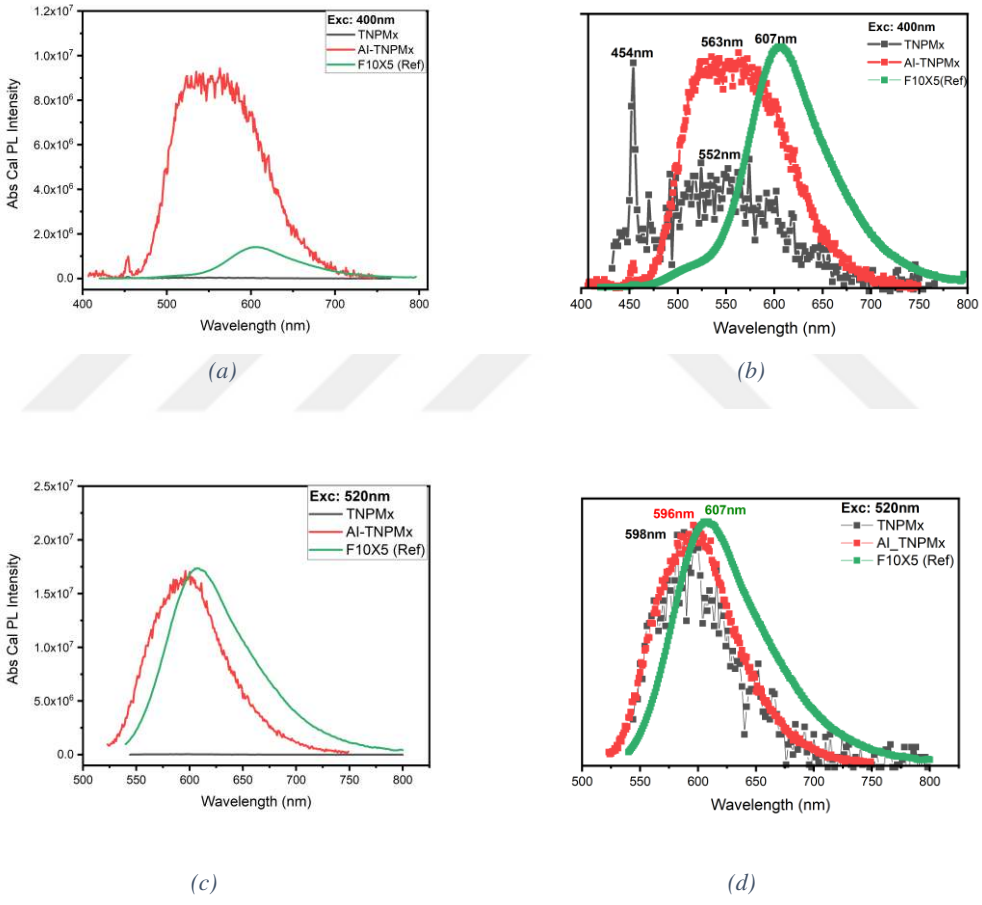

Figure 3.29: Comparison of CD01, AI-CD01 and Reference Red (F10X5): (a) PL. Excitation: 400 nm, (b) Normalized PL. Excitation:400 nm, (c) PL. Excitation:520 nm, (d) Normalized PL. Excitation: 520 nm.

According to XPS results, the increase in the O/C atomic ratio might increase the contribution of oxygen related defect energy trapping states to the radiative

recombination. Higher electron density in n energy state (n_O) provided a stronger PL emission (Jin et al., 2013).

3.2.3 Comparison of Other Particles

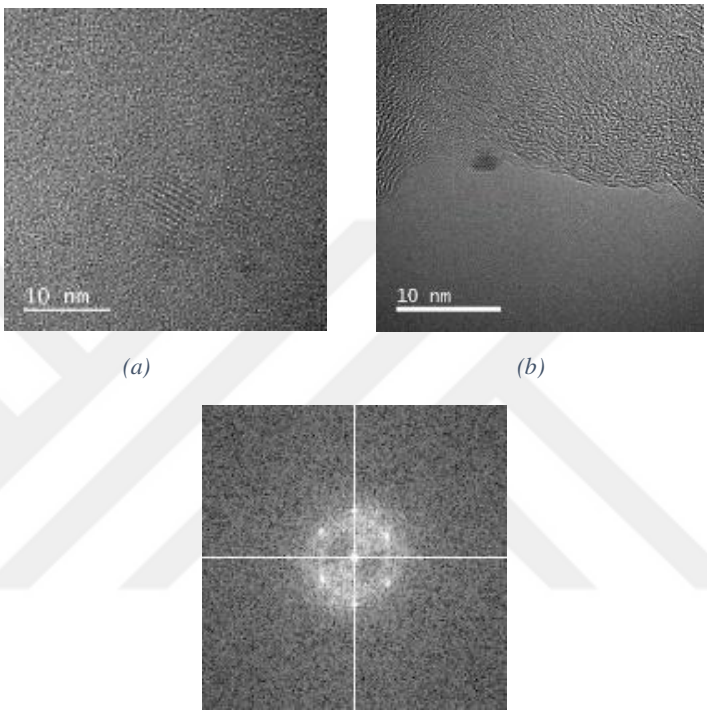

(a) *(b)*

(c)

Figure 3.30: CD12: (a) and (b) TEM images, (c) Reduced FFT image.

The morphologies and structures of the carbon nanoparticles were investigated by TEM. The dark spots in the images correspond to the carbon nanoparticles. The crystalline nature of CD12 (Figure 3.30.a and b) was verified by the well resolved ring structure in its FFT image (Figure 3.30.c). Only CD12 (Figure 3.30.a) and CD22 (Figure 3.31.b) showed spherical shape. However, the others (CD18, CD24, CD29, CD33) displayed long and ribbon-like lattice fringes, with particle sizes comparable to their hydrodynamic sizes (Table 3.5: DLS comparison of CD12, CD33, CD22, CD29, CD18 and CD24.).

It seemed that in TEM images of CD18 (Figure 3.31.a), CD24 (Figure 3.31.c), CD29 (Figure 3.31.d) and CD33 (Figure 3.31.e), all the particles were merged. Among those

carbon dots, p-PDA was the common precursor, but the shape and assembly of these nanoparticles can't be ascribed to p-PDA. Since in the p-PDA based nanoparticle literature, the particles were well dispersed and have spherical shapes (Jia, 2019 and Ding et al., 2016 and Lee, 2021). The Figure 3.31.b showed CD22 particles, each consists of closely spaced graphene layers, that were separated by the surrounding media. The Figure 3.31.d- e displayed that CD29 and CD33 consist of large ribbon-like graphene sheets.

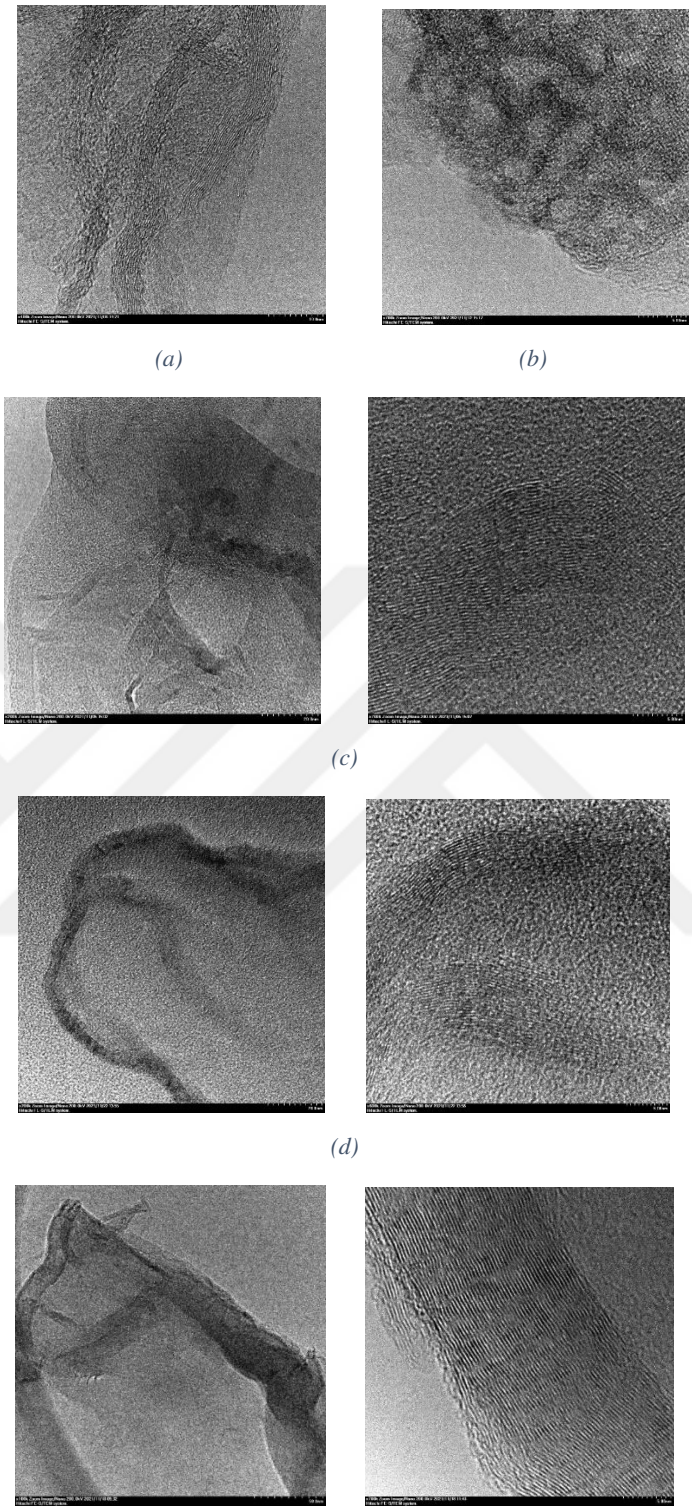

(a) *(b)*

(c)

(d)

(e)

Figure 3.31: TEM images of: (a) CD18, (b) CD22, (c) CD24, (d) CD29, (e) CD33.

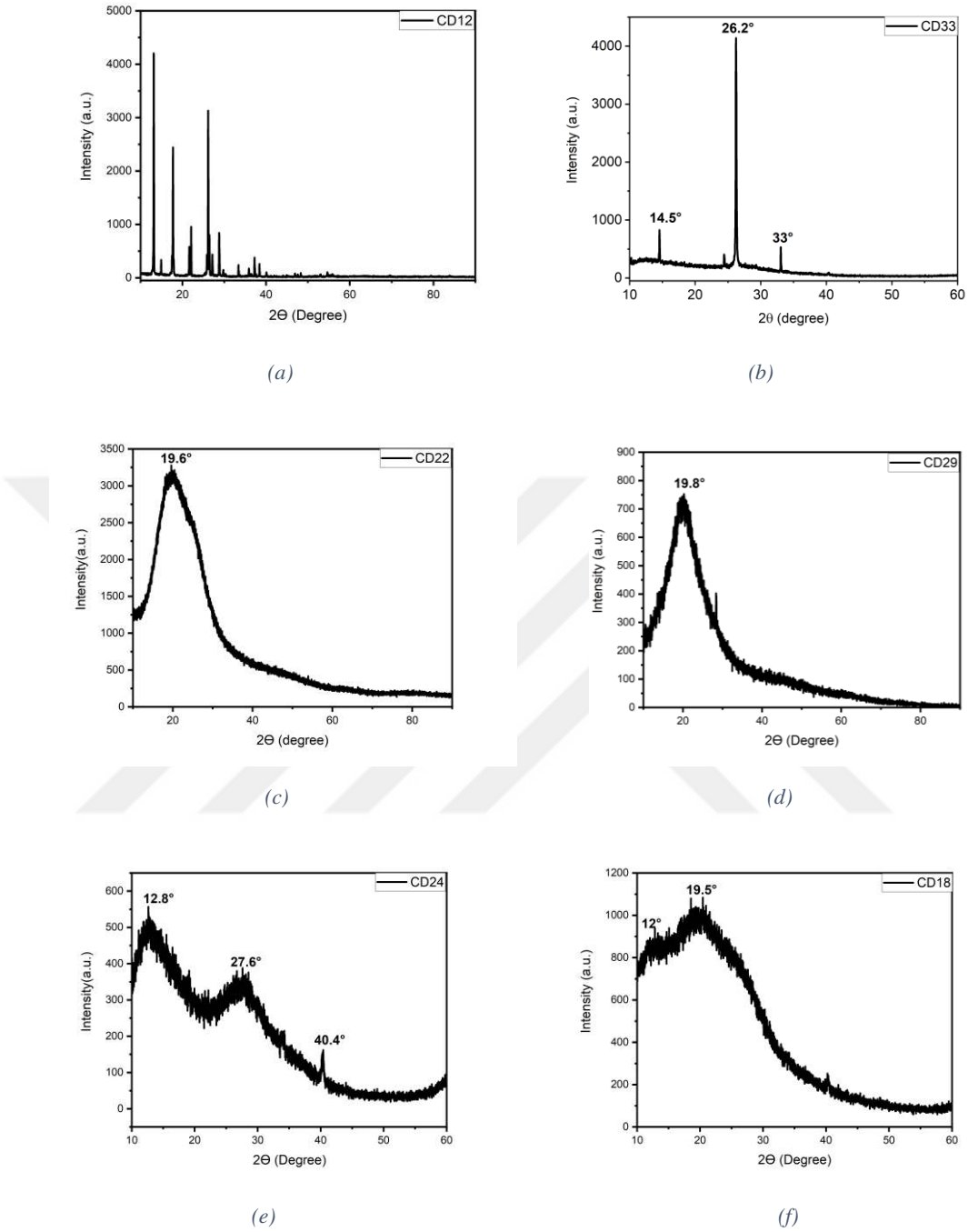

Figure 3.32: XRD spectra of: (a) CD12, (b) CD33, (c) CD22, (d) CD29, (e) CD24, (f) CD18.

For all the carbon dot samples, the XRD peaks (between 12°-40°) indicate the existence of crystalline lattices in their structure, which is consistent with their TEM images. In Figure 3.32, the XRD spectra of CD22, CD29, CD24 and CD18 exhibited broad single peaks centered respectively at 19.6°, 19.8°, 27.6° and 19.5°. The positions of these Bragg angles correspond to the diffraction of (002) plane of graphite with an

interplanar spacing of 3.34 Å (Puvvada, 2012). In CD12 and CD24, the peaks at ca. 40° derived from the diffraction of (100) or (101) plane of graphite and in CD24, CD18 and CD33 the peaks ca. at 12°-14° came from the diffraction of (001) plane of graphite (Ostyn, 2019).

Table 3.5: DLS comparison of CD12, CD33, CD22, CD29, CD18 and CD24.

Sample Name	PDI	Size Distribution by Number (nm)	Size Distribution by Intensity (nm)	Zeta Potential (mV)
CD12	0.754	33.04 ± 6.162	47.12 ± 12.05	-
CD33	0.602	232.1 ± 56.58	259.2 ± 57.57	-
CD22	1.000	97.75 ± 18.81	110.7 ± 18.01	-
CD29	0.673	125.0 ± 46.63	185.8 ± 63.94	
CD18	0.523	30.79 ± 9.647	40.78 ± 9.818	+21.9 ± 1.81
CD24	0.772	292.4 ± 108.4	393.1 ± 138.5	+31.8 ± 2.20

According to the DLS data, shown in Table 3.5, CD24, CD29 and CD33 contained some aggregated nanoparticles, which were consistent with their TEM images (Figure 3.31.c,d,e). The surface charges of the aqueous carbon dot nanoparticles were determined by the Zeta Potential as +21.9±1.81 mV and +31.8±2.20 mV, respectively for CD18 and CD24. We assumed that these cationic charges resulted from the pyridinic/pyrrolic amine groups on the surface of the CDs or from the primary amines, which were not so observable in the FTIR data in the range 3300-3550 cm^{-1} (Wang et al., 2021).

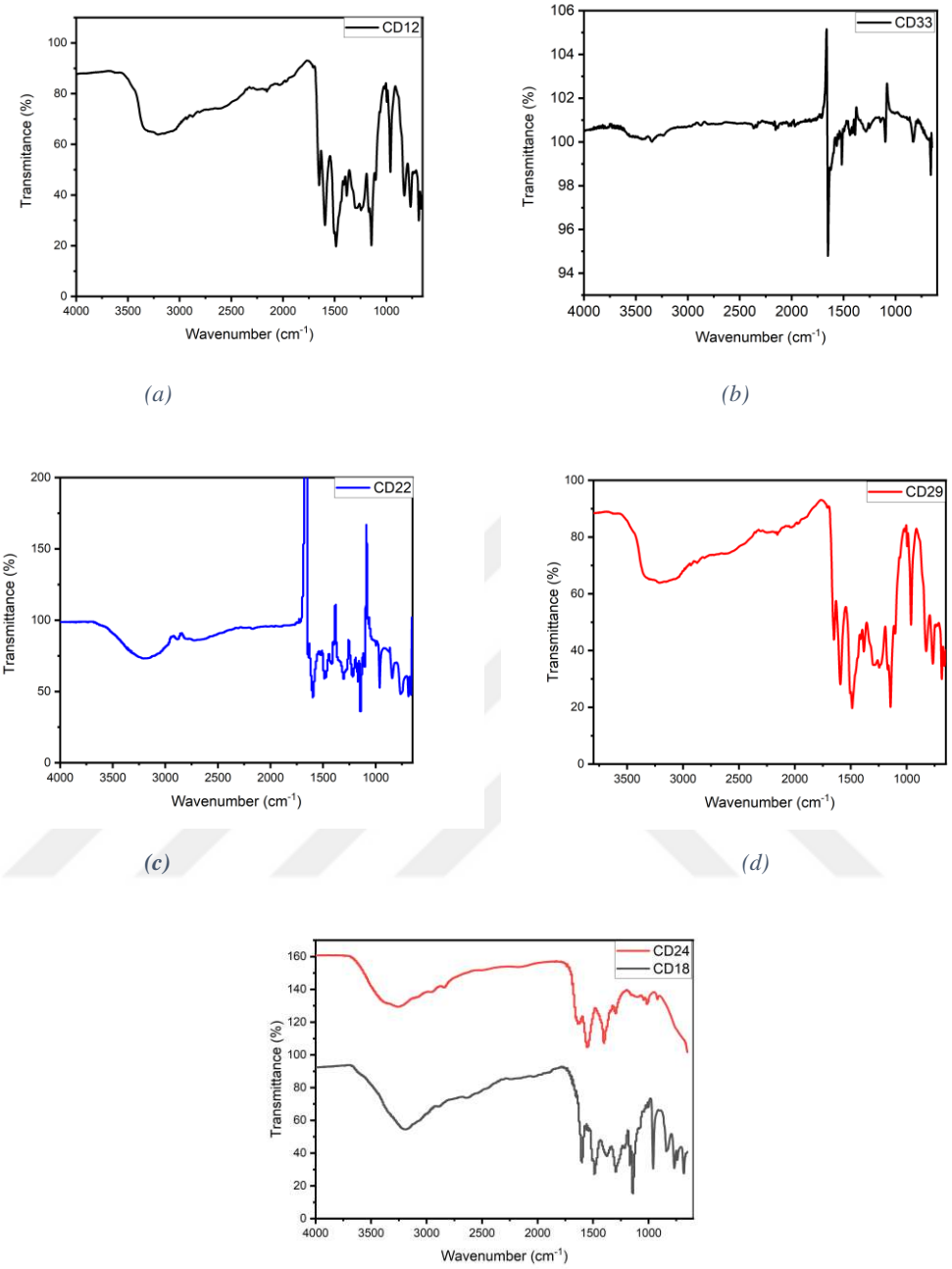

Figure 3.33: FTIR spectra of: (a) CD12, (b) CD33, (c) CD22, (d) CD29, (e) CD18 and CD24.

According to FTIR spectrums of carbon dot nanoparticles in Figure 3.33, the broad and strong peak spanning from 3700 to 3000 cm^{-1} and centering at nearly 3200-3300 cm^{-1} stands for O-H stretching vibration of carboxylic acid on the CD surfaces. The stretching of the primary N-H was not observable due to the overlap with O-H bond stretching (Sodipo et al., 2018). The peaks at around 2840, 1650, 1630, 1590, 1500, 1380, 1300,

1140 cm^{-1} represent the asymmetric stretching of C-H, C=O, C=N, C=C, C-H bending, C-O, C-N stretching and C=C bending respectively (Dager, 2019). Among the organic CDs (CD12, CD22, CD29, CD33) in CD22 and among the aqueous CDs (CD18, CD24) in CD18, the C=O stretching was weaker. Except from the aqueous based CDs (CD18, CD24) and CD33, the C=C bond stretching was apparent at 1590 cm^{-1} in the FTIR spectra of CD22, CD29, CD12. None of them contained triple bond (C≡C, C≡N) since there wasn't any vibrational frequency between 2000-2500 cm^{-1}.

According to their high resolution XPS spectrum, CD18 contains 5 different carbon types (Figure 3.37). The peak at ~289 eV is attributed to the carboxylic acid (Figure 3.37.a), which enhances the water solubility. The presence of graphitic (quaternary) N at ~401 eV in N1s (Figure 3.37.b) and presence of C=N/C-N at ~285 eV in C1s (Figure 3.37.a) confirm successful doping of nitrogen into CDs. The peaks at ~406 eV in N1s (Figure 3.37.b) and ~534 eV in O1s (Figure 3.37.c) were attributed to the N-O bond, resulting from the reaction of Resorcinol and p-PDA in aqueous environment (H_2O was the solvent) (Yang, 2020). Both the water and the aromatic are oxygen sources.

By keeping precursor, the same but changing the solvent from water to DMF, it was obvious in N1s spectra (Figure 3.38.b) that CD29 lacked the growth of N-O bond. Using an amide structure as solvent has improved the N-doping from 7.28% to 9.84%.

Going from CD29 to CD22 (Figure 3.38.c and Figure 3.35.c), the oxygen content has increased from 10.52% (CD29) to 13.39% (CD22), thus CD22 has a more redshifted and stronger emission intensity than CD29. Therefore, we assumed that the spatial orientation / conformation of Resorcinol was more favorable with o-PDA rather than p-PDA (Figure 3.18).

Due to the larger dimensions of the CDs (Table 3.5), compared to CD01 and AI-CD01 (Table 3.2), and the vertical depth resolution of the XPS is only 10 nm, sp^2 carbon (C=C bond) at ~283 eV was only present in CD18 and CD29 C1s spectrum (Figure 3.37.a and Figure 3.38.a) up to 2-3% extent (Nunney, 2011). Although rest of the CDs (CD12, CD22, CD24, CD33) also show crystallinity in their TEM images (Figure 3.30.a-b, Figure 3.31.b, Figure 3.31.c, Figure 3.31.e), their related C1s spectrum don't display sp^2 carbon (C=C).

By changing the precursor Resorcinol into N-doping aromatic Melamine (Melamine-pPDA in DMF), the nitrogen content has risen from 9.84%.to 13.94% and the oxygen content has decreased from 10.52% to 9.95%. Since CD33 emits at a longer wavelength with stronger intensity than CD29 (Figure 3.18), we assumed that the spatial orientation / conformation of p-PDA was more favorable with Melamine rather than Resorcinol. Thus, Melamine has a better integration and conjugation with p-PDA during the molecular fusion step of carbon dot synthesis. However due to larger hydrodynamic size of CD33 (Table 3.5), the conjugated carbon core is not observable.

In the high resolution N1s spectra of CD12 (Resorcinol-Melamine in DMF), the N-O peak at ~404 eV resulted from the conjugated oxygen source Resorcinol (Figure 3.34.b). Also, the C-O/C=O bond is relatively higher than CD29 (Figure 3.34.a). These results indicate that the conformation of the Resorcinol varied while reacting with different N sources: Melamine and p-PDA and resulted in different bonds formation.

The branched structure of the b-PEI led to the presence of graphitic (quaternary) N (Figure 3.36.b) at ~401 eV in N1s.

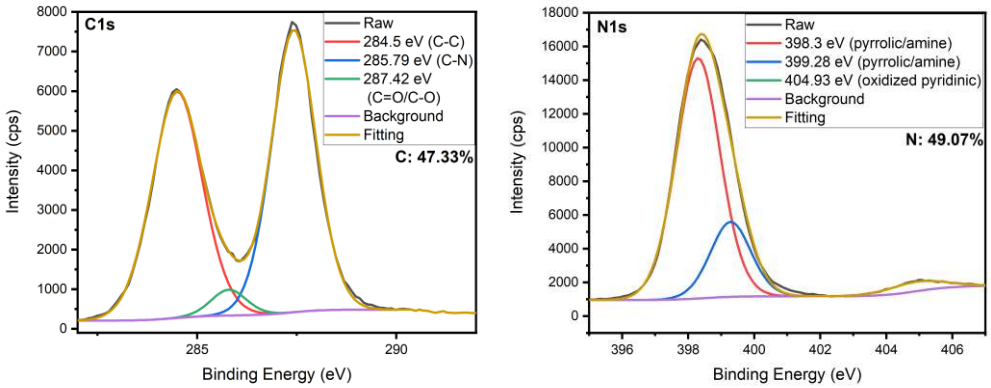

(a) *(b)*

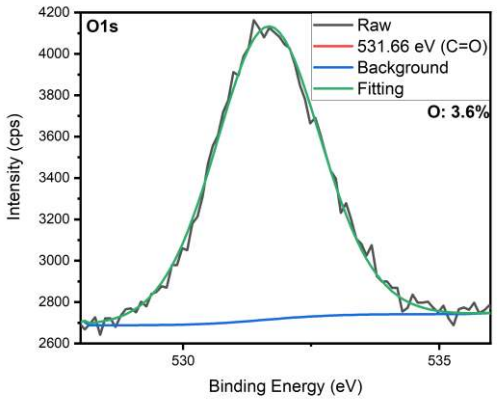

(c)

Figure 3.34: XPS analysis of CD12: High resolution spectrum of (a) C1s, (b) N1s, (c) O1s.

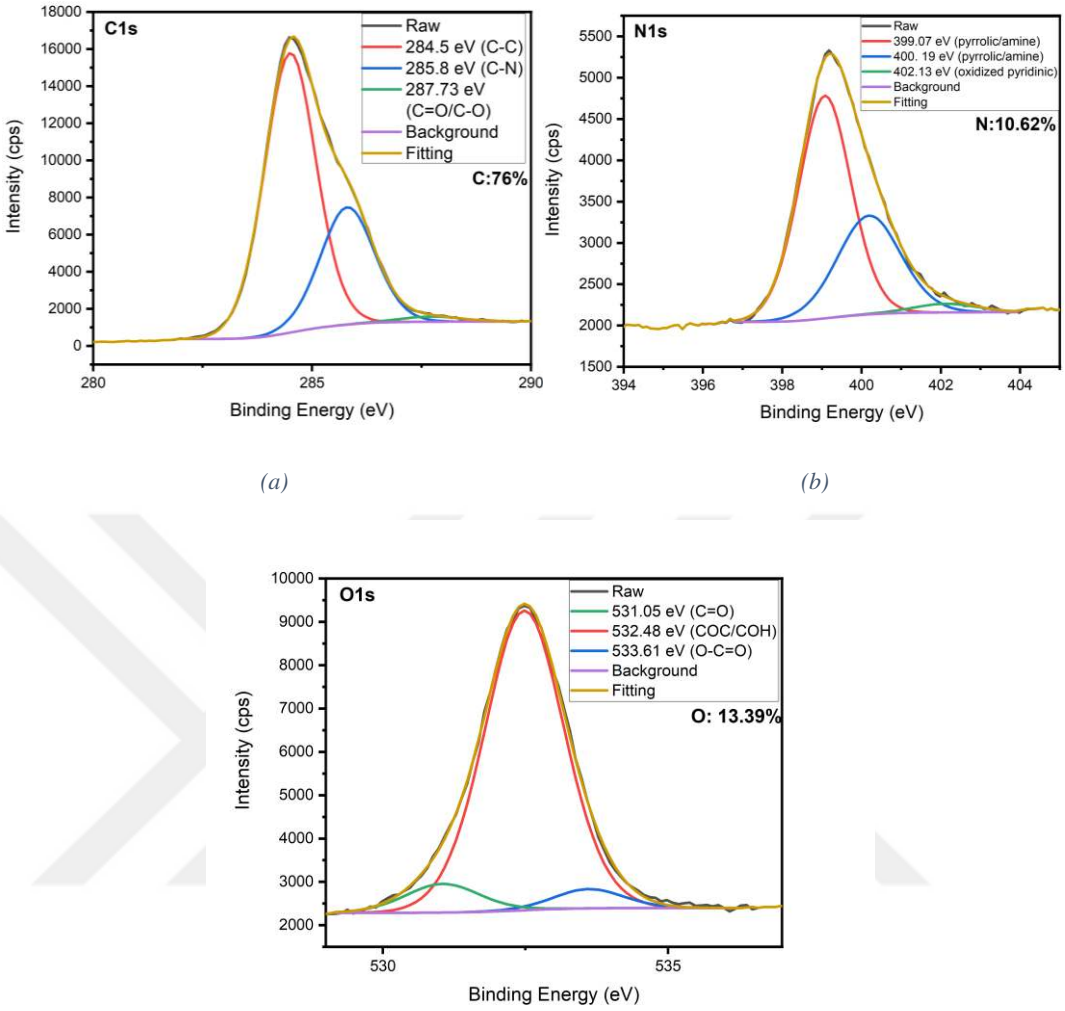

(a) *(b)*

(c)

Figure 3.35: XPS analysis of CD22: High resolution spectrum of (a) C1s, (b) N1s, (c) O1s.

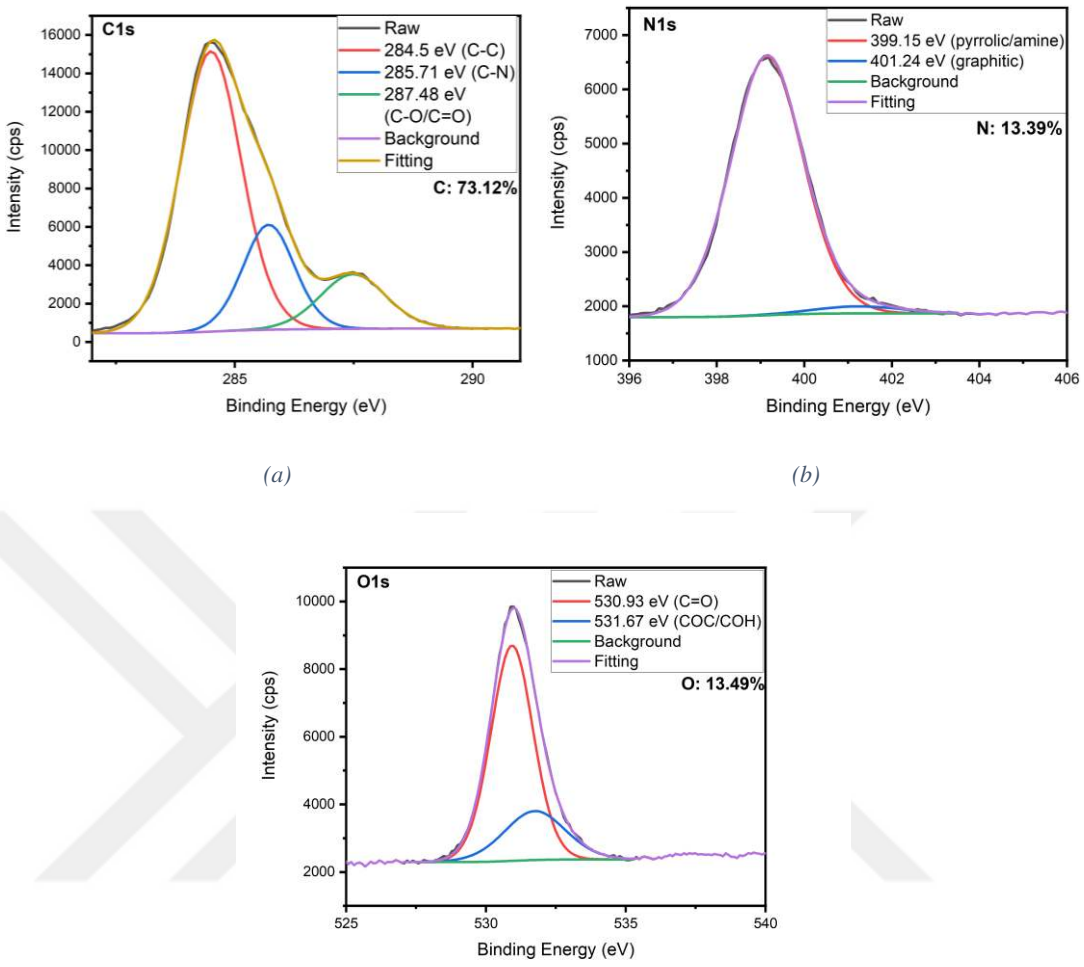

(a) *(b)*

(c)

Figure 3.36: XPS analysis of CD24: High resolution spectrum of (a) C1s, (b) N1s, (c) O1s.

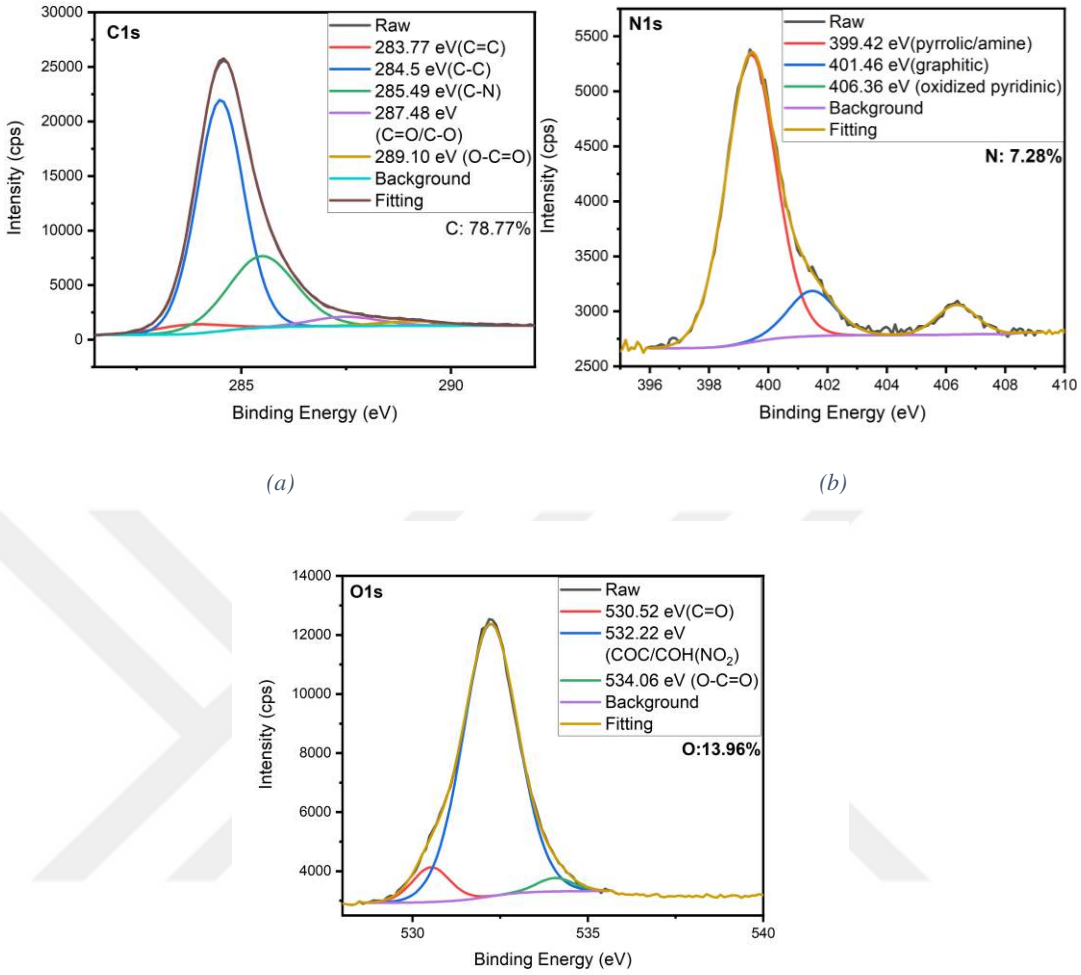

(a) *(b)*

(c)

Figure 3.37: XPS analysis of CD18: High resolution spectrum of (a) C1s, (b) N1s, (c) O1s.

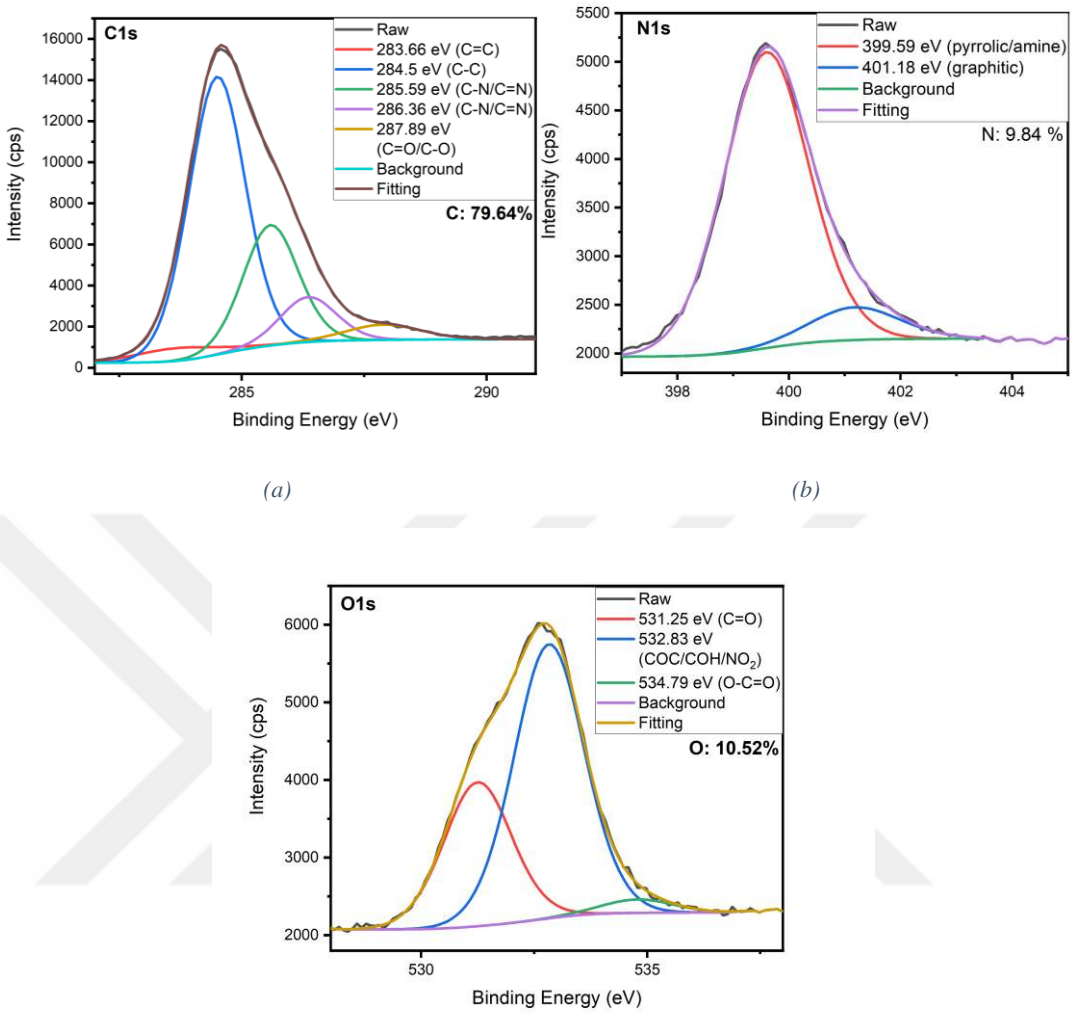

(a) *(b)*

(c)

Figure 3.38: XPS analysis of CD29: High resolution spectrum of (a) C1s, (b) N1s, (c) O1s.

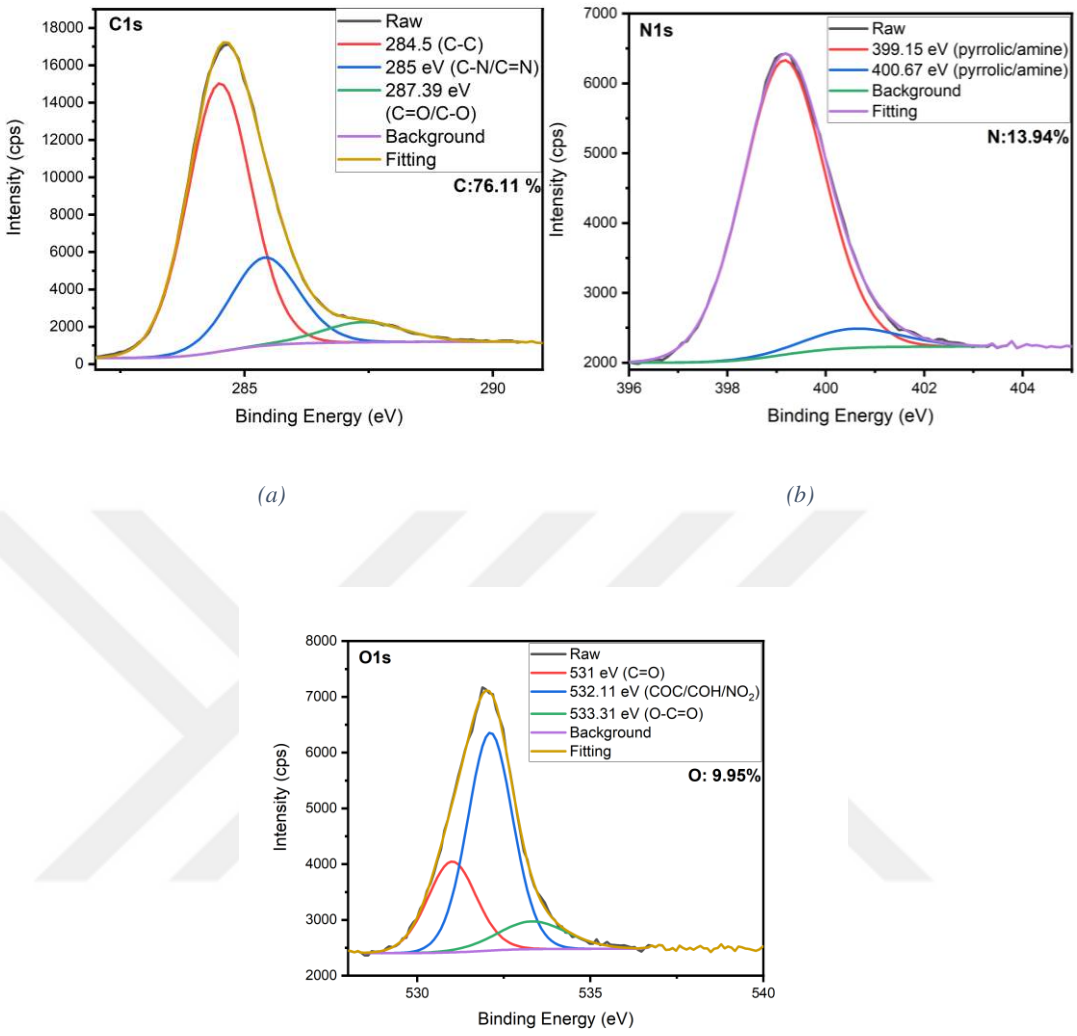

(a) *(b)*

(c)

Figure 3.39: XPS analysis of CD33: High resolution spectrum of (a) C1s, (b) N1s, (c) O1s.

To determine the emission characteristics of carbon dot nanoparticles photoluminescence analysis were performed, shown in. It was recorded that under 303 nm excitation wavelength (Figure 3.40.a). CD22 gives the emission with highest intensity at 440 and 513 nm (Figure 3.40.b). After the synthesis, the emission intensity of the CD nanoparticle started to decrease and stabilized in week 8 (Figure 3.40.d). The particle has a Quantum Yield of 14% between 320-530 nm and 12% in broader range between 320-600 nm. The average time that an excited state electron spends before going back to ground state is 2.4 ns, shown in Table 6. Under 365 nm light CD22 emits yellow (Figure 3.40.c).

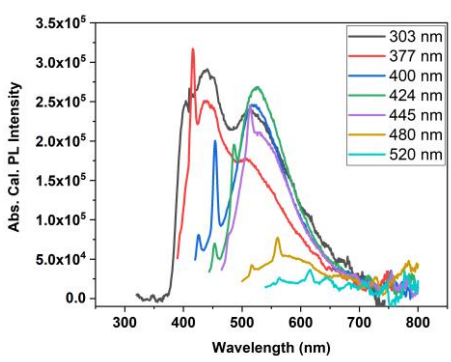

(a)

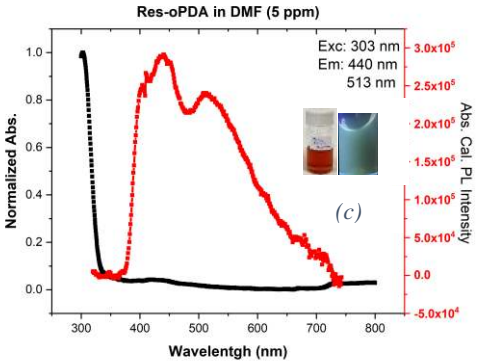

(c)

(b)

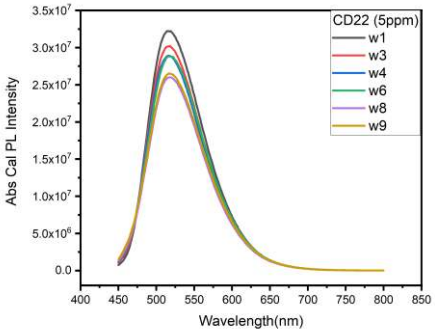

(d)

Figure 3.40: Resorcinol- oPDA in DMF (CD22): (a) PL under different excitation wavelengths, (b) PL under 303 nm excitation, (c) Image under day and UV light respectively, (d) PL stability.

It was recorded that under 400 nm excitation wavelength, CD29 gives the emission with highest intensity at 452 nm (Figure 3.41.b). The average time that an excited state electron spends before going back to ground state is 7.4 ns, shown in Table 3.6. Under 365 nm light CD29 emits bluish white (Figure 3.41.c).

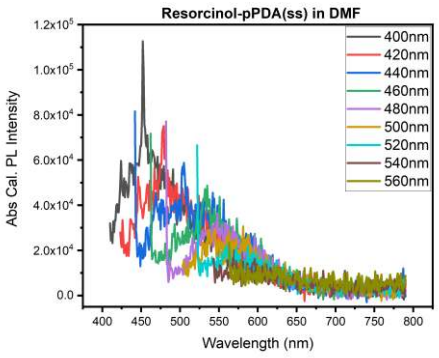

(a)

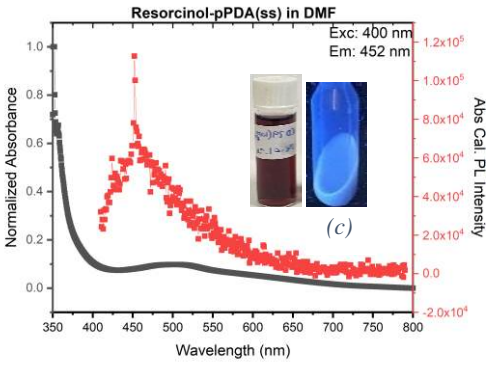

(c)

(b)

Figure 3.41: Resorcinol- pPDA(ss) in DMF (CD29): (a) PL under different excitation wavelengths, (b) PL under 400 nm excitation, (c) Image under day and UV light respectively.

It was recorded that under 380 nm excitation wavelength, CD12 gives the emission with highest intensity at 428 nm (Figure 3.42.b). After the synthesis, the emission intensity of the CD nanoparticle started to increase and stabilized in week 9 (Figure 38.d). The particle has a Quantum Yield of 79% between 280-800 nm. The average time that an excited state electron spends before going back to ground state is 6.3 ns, shown in Table 3.6. Under 365 nm light CD12 emits bluish white (Figure 3.42.c).

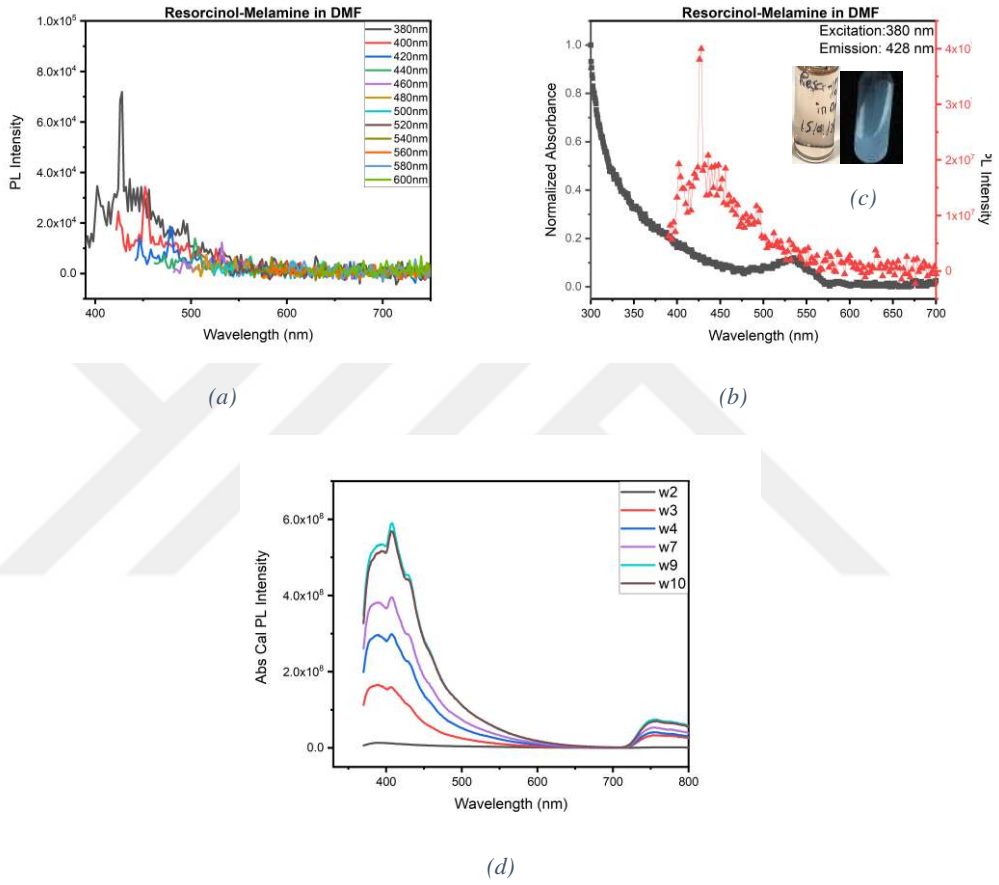

Figure 3.42: Resorcinol- Melamine in DMF (CD12): (a) PL under different excitation wavelengths, (b) PL under 380 nm excitation, (c) Image under day and UV light respectively, (d) PL stability.

It was recorded that under 580 nm excitation wavelength, CD18 gives the emission with highest intensity at 604 nm (Figure 3.43.b). After the synthesis, the emission intensity of the CD nanoparticle started to increase up to 3 weeks and then decreased and stabilized in week 8 (Figure 39.d). The particle has a Quantum Yield of 0.12% between 550-700 nm. The average time that an excited state electron spends before going back to ground state is 9.2 ns, shown in Table 3.6. Under 365 nm light CD18 emits bluish white (Figure 3.43.c).

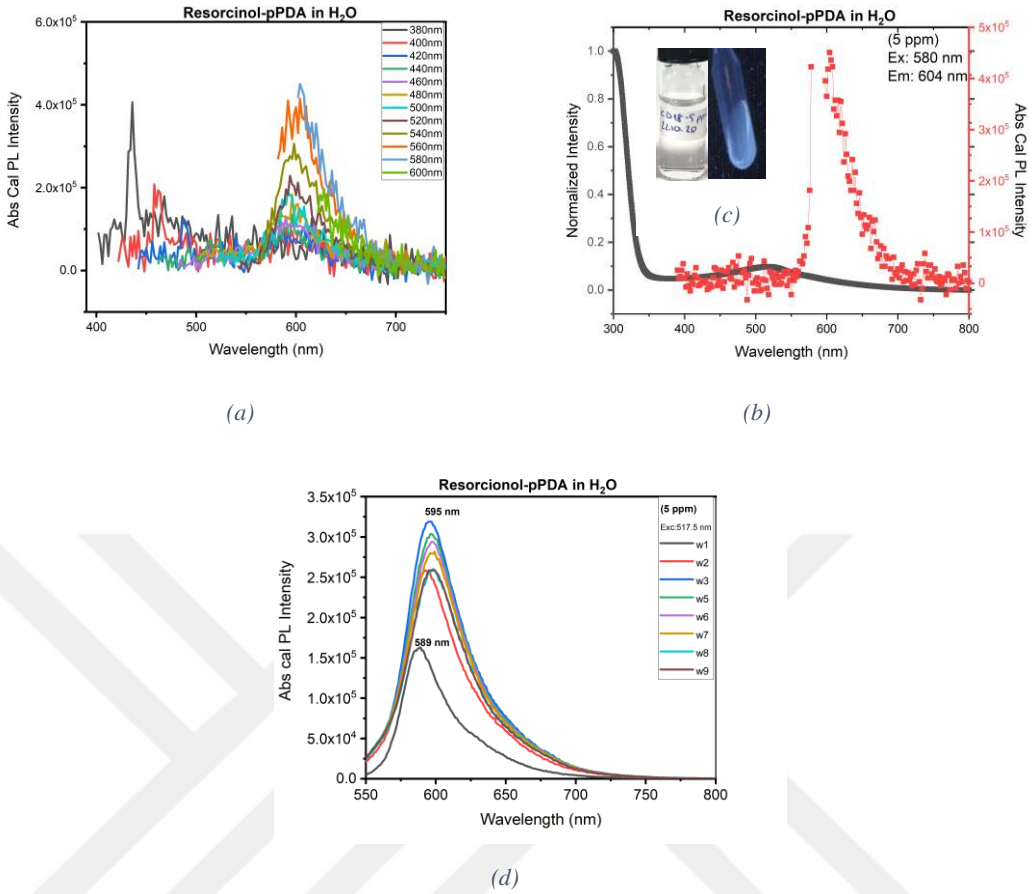

Figure 3.43: Resorcinol-pPDA in water (CD18): (a) PL under different excitation wavelengths, (b) PL under 580 nm excitation, (c) Image under day and UV light respectively, (d) PL stability.

It was recorded that under 380 nm excitation wavelength, CD24 gives the emission with highest intensity at 450 nm (Figure 3.44.b). After the synthesis, the emission intensity of the CD nanoparticle started to decrease and then stabilized in week 8 (Figure 40.d). The particle has a Quantum Yield of 1.19% between 400-550 nm. The average time that an excited state electron spends before going back to ground state is 7.1 ns. Under 365 nm light CD24 emits cyan (Figure 3.44.c).

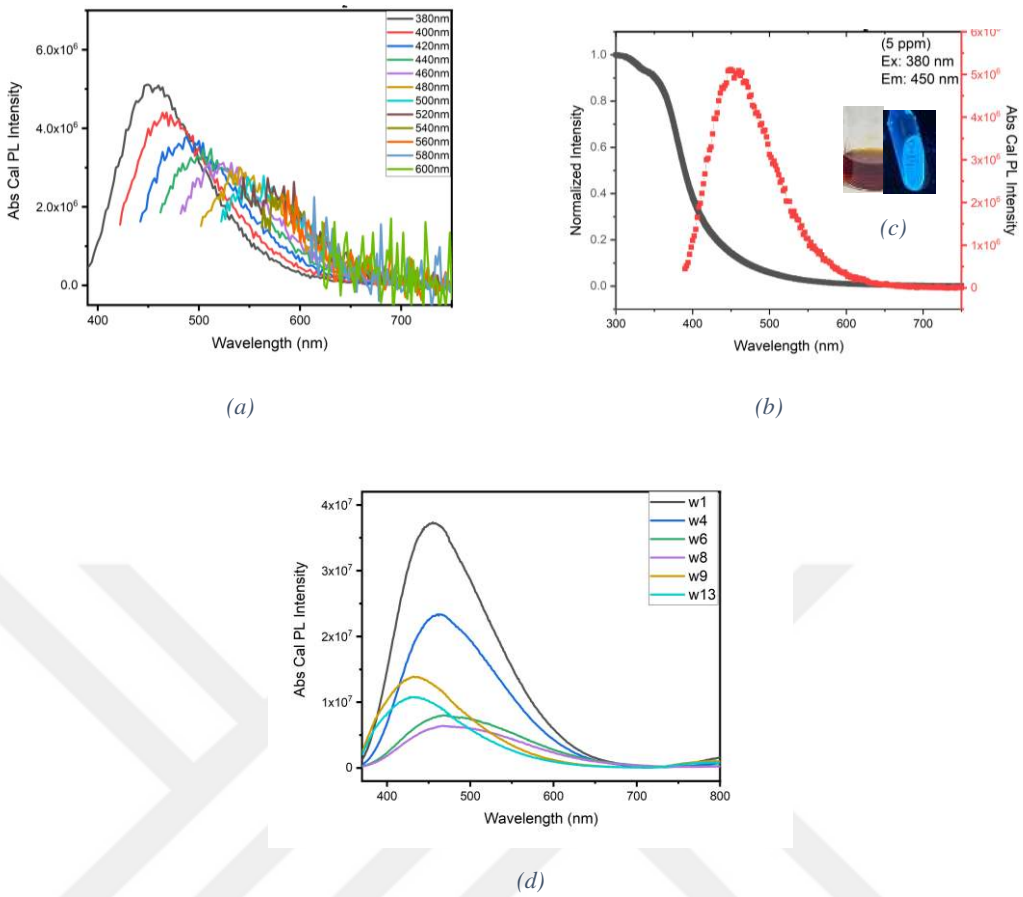

Figure 3.44: bPEI- Maleic acid in water (CD24): (a) PL under different excitation wavelengths, (b) PL. Excitation: 380 nm, (c) Image under day and UV light respectively, (d) PL stability.

It was recorded that under 520 nm excitation wavelength, CD33 gives the emission with highest intensity at 583 nm (Figure 3.45.b). The particle has a Quantum Yield of 11.03% between 530-680 nm. The average time that an excited state electron spends before going back to ground state is 7.1 ns, shown in Table 3.6. Under 365 nm light CD33 emits yellow (Figure 3.45.c).

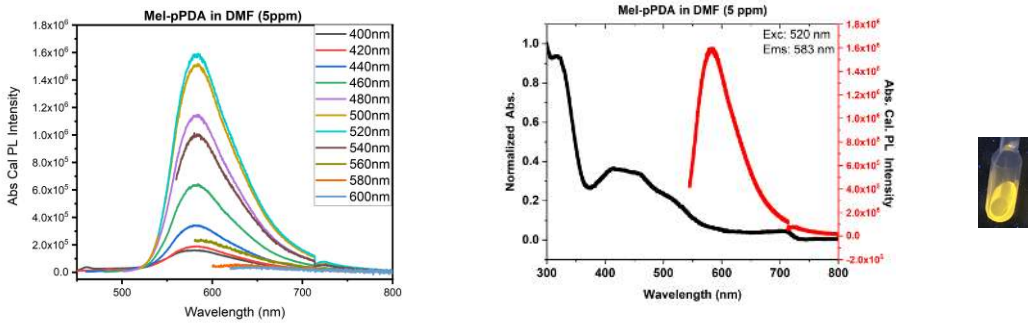

(a) *(b)* *(c)*

Figure 3.45: Melamine- pPDA in DMF (CD33): (a) PL under different excitation wavelengths, (b) PL. Excitation: 520 nm, (c) Image under UV light.

As can be observed in Figure 3.41.a, Figure 3.42.a, Figure 3.44.a, CD29, CD12 and CD24 exhibited excitation wavelength dependent emission. As cited in Crista et al., different synthesis techniques yield difference in PL origin and among different bottom-up synthesis routes, hydrothermal reaction is the one that has highest contribution from the surface states emission (Crista, 2020). Energy of different photons satisfied different energy bandgaps, corresponding to different defect states and surface functional groups. As a result, each defect state acted as a different luminescent center and depending on the energy of the incoming light, different luminescence centers dominate the emission behavior.

Table 3.6: FL Lifetime of CD12, CD33, CD22, CD29, CD18 and CD24.

Sample Name	Emission Point (nm)	Major Event (%)	Decay Time (T1) (ns)	Minor Event (%)	Decay Time (T2) (ns)	Middle Event (%)	Decay Time (T3) (ns)	Average Decay Time (ns)
CD12	520	67.79	8.2	32.21	2.39	-	-	6.33
CD33	578	86.06	11	4.59	213	9.35	3.47	19.56
CD22	438	71.09	1.34	28.91	4.99	-	-	2.40
CD29	520	64.47	9.78	35.53	3.04	-	-	7.39
CD18	450	80	10.66	20	3.15	-	-	9.16
CD24	450	75.1	8.62	24.9	2.7	-	-	7.15

3.2.4 Security Tag Applications of Organic based CDs

CD01 in solution form has an excitation independent emission, giving the maximum emission intensity at 565 nm under 480 nm excitation. As it was expected from CD01 based ink on paper, measuring with 405 nm sensor gave the optimum emission at 600 nm. Carbon dot nanoparticles were dispersed in commercial binder in different concentrations, such as 100 ppm, 200 ppm and 1000 ppm to see the effect of CD concentration on photoluminescence behavior. 1000 ppm loading of the nanoparticle has 2.5 times greater intensity than the 100 ppm loading and 1.5 times greater intensity than 200 ppm loading. No concentration-based quenching was observed in emission. As it was observed in the Figure 3.47.b., the emission intensity of the ink mixture has increased for 72 days, afterwards started to decrease. Tracking the emission of CD01 based ink in above-mentioned emission channels, yielded higher emission intensities compared to the Quantag Reference Red dot-based ink mixtures (Figure 3.47.a).

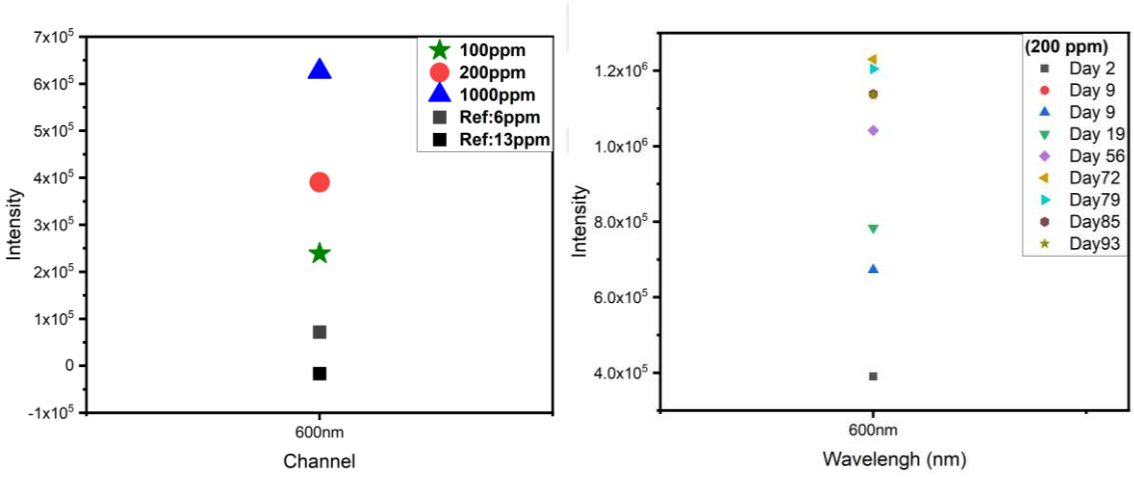

(a) *(b)*

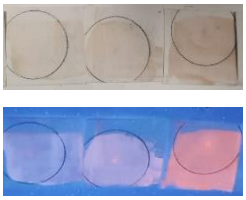

(c)

Figure 3.47: (a) Emission comparison of inks containing different CD01 loadings with respect to Reference red (F10X5) based inks, (b) Stability of 200 ppm CD01 loaded ink, (c) Day and UV light images of 100 ppm, 200 ppm and 1000 ppm CD01 loaded inks, respectively from left to right.

AI-CD01, in solution form has an excitation independent emission, giving the maximum emission intensity at 596 nm under 520 nm excitation. As it was expected from AI-CD01 based ink on paper, measuring with 525 nm sensor gave the optimum emission lines at 615 nm and 650 nm. It was put to the commercially available binder in different concentrations, these were 100 ppm, 200 ppm and 400 ppm. It was obvious that 200 ppm loading of the nanoparticle has 1.5 times greater intensity than the 100 ppm loading, however CD concentration over 200 ppm has led to quenching of the emission. As it was observed in the Figure 3.48.b., the emission intensity of the ink mixture has increased for 129 days, afterwards started to decrease. Tracking the emission of AI-CD01 based ink in above-mentioned emission channels, yielded higher emission intensities compared to the Quantag Reference Red dot-based ink mixture (Figure 3.48.a).

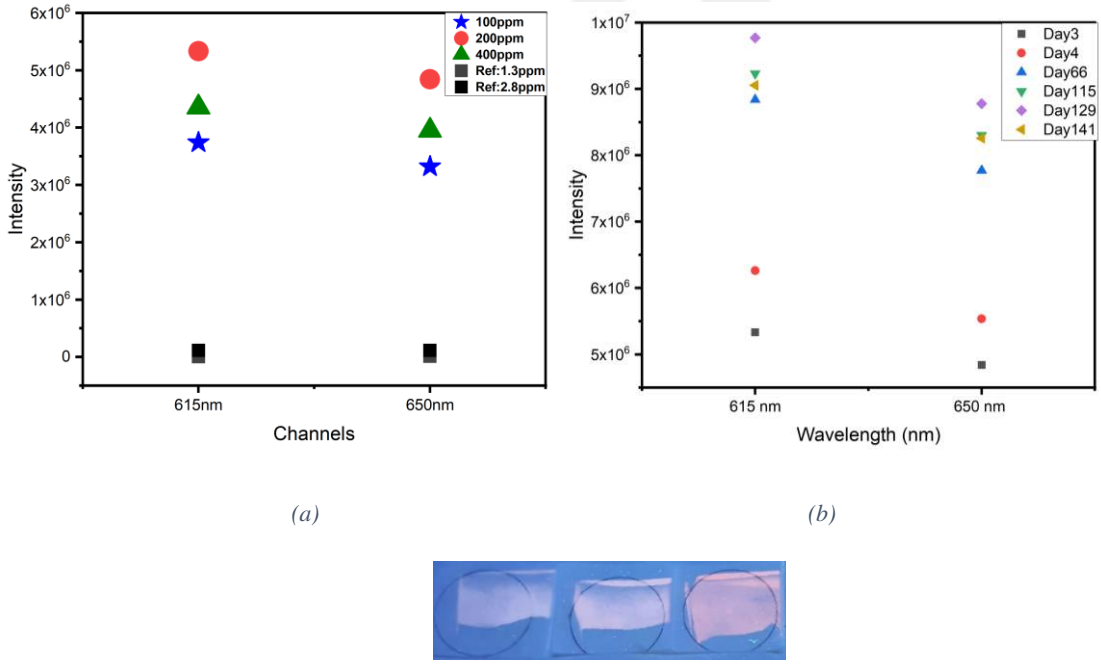

(a) *(b)*

(c)

Figure 3.48: (a) Emission comparison of inks containing different AI-CD01 loadings with respect to Reference red (F10X5) based inks, (b) Stability of 200 ppm AI-CD01 loaded ink, (c) UV light images of 100 ppm, 200 ppm and 400 ppm CD01 loaded inks, respectively from left to right.

CD12, in solution form has an excitation dependent emission, giving the maximum emission intensity at 428 nm under 380 nm excitation. As it was expected from CD12 based ink on paper, measuring with 405 nm sensor gave the optimum emission lines at

500 nm and 600 nm. It was applied to the commercially available binder in different concentrations, these were 100 ppm and 600 ppm. It was obvious in Figure 3.49.a., that 600 ppm loading has led to quenching of the emission due to inner-filter effect. As it was observed in the figure, the emission intensity of the 100 ppm CD12 based ink mixture has increased for 64 days, afterwards started to decrease (Figure 3.49.b). Tracking the emission of CD12 based ink in above-mentioned emission channels, yielded higher emission intensities compared to the Quantag Reference Red dot-based ink mixture at day 64 (Figure 3.49.a).

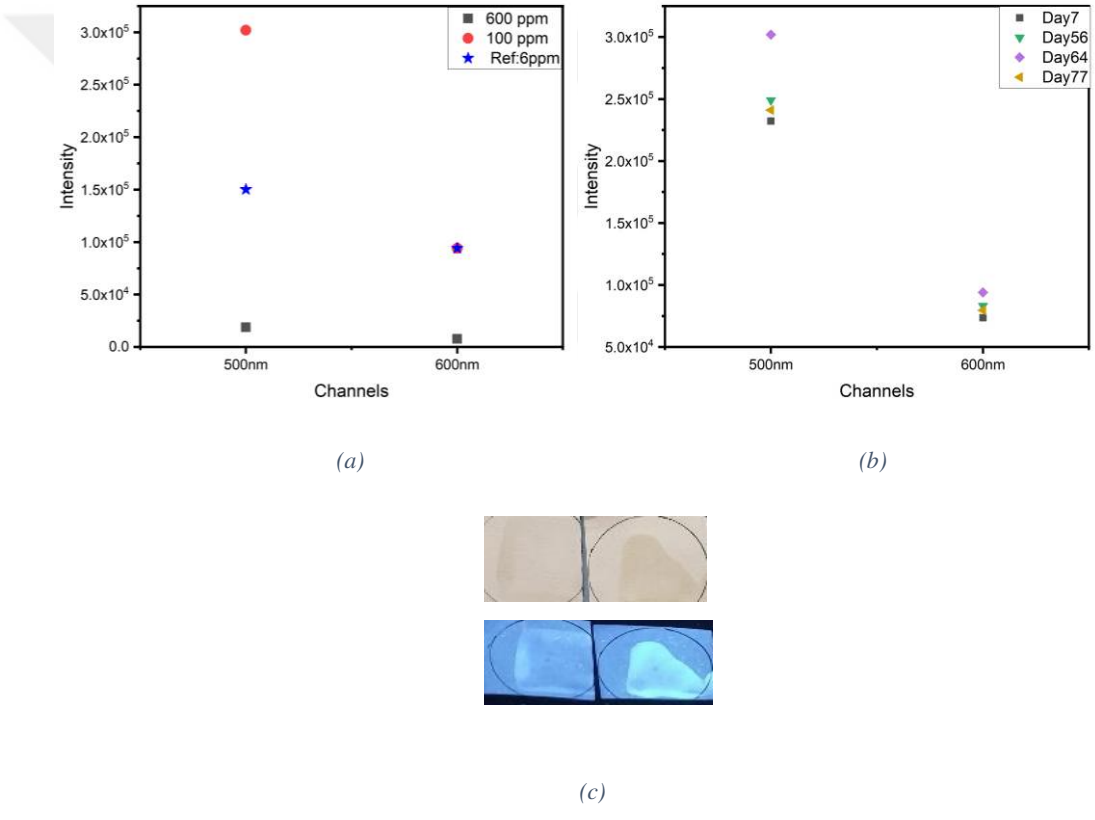

(a) *(b)*

(c)

Figure 3.49: (a) Emission comparison of inks containing different CD12 loadings with respect to Reference red (F10X5) based inks at day 64, (b) Stability of 100 ppm CD12 loaded ink, (c) Day and UV light images of 100 ppm and 600 ppm CD12 loaded inks, respectively from left to right.

CD33 has an excitation independent emission, giving the maximum emission intensity at 583 nm under 520 nm excitation. It was applied to the commercially available binder in different concentrations, respectively 60, 100 and 200 ppm. As it was expected

from CD33 based ink on paper, measuring with 525 nm sensor gave the optimum emission lines at 615 nm and 650 nm.

Even though 100 ppm has a comparable emission intensity with 60 ppm, concentrations above 60 ppm have been quenched (Figure 3.50.a). As it was observed in Figure 3.50.b. the emission intensity of the 60 ppm carbon dot loading has decreased for 18 weeks, nonetheless the emission still didn't quench. Tracking the emission of CD33-based ink in above-mentioned emission channels, yielded higher emission intensities compared to the Quantag Reference Red dot-based ink mixture at 60 and 100 ppm CD concentrations, however 200 ppm CD concentration yielded lower emission intensity than the reference (Figure 3.50.a).

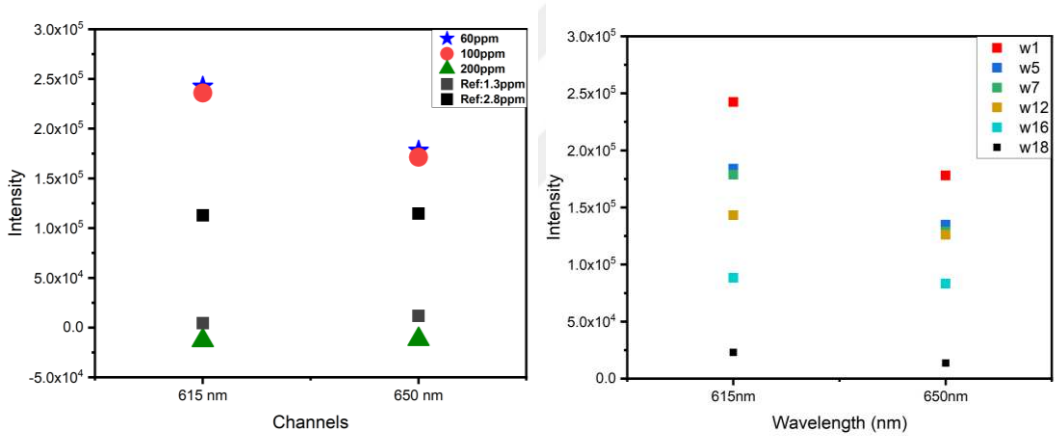

(a) *(b)*

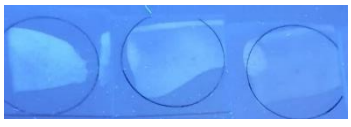

(c)

Figure 3.50: (a) Emission comparison of inks containing different CD33 loadings with respect to Reference red (F10X5) based inks, (b) Stability of 60 ppm CD33 loaded ink, (c) UV light images of 60 ppm, 100 ppm and 200 ppm CD01 loaded inks, respectively from left to right.

Among the different yellow/orange emitting carbon dots such as CD01, AICD01 and CD33, only CD01-based ink was tracked at 600 nm emission channel. The inks based on the other two CDs were tracked at 615 and 650 nm emission channels. Among the three

CDs at 100 ppm loading, AI-CD01-based ink has 10 times greater emission intensity, confirming the PL emissions of the CDs in solution form. In general, 100 ppm CD concentration in commercial binder could be evaluated as a safer upper limit for fluorescent security tagging applications, without any concentration quenching effect. Nearly all the CDs, especially AI-CD01 had superior stability in paper applied ink form rather than their solution forms. This indicated that the commercial binder avoids interaction among the nanoparticles and quenching. CD01 and CD12 exhibited longer stability in binder than the Quantag Reference Red dot which has increasing intensity for 58 days at 500 nm and 600 nm (405 nm sensor). However, AI-CD01 and CD33 exhibited shorter stability in binder than the Quantag Reference Red dot, which has increasing emission intensity for more than 175 days at 615 nm and 650 nm (525 nm sensor).

3.2.5 Security Tag Application of Aqueous based CDs

In section 3.1.2 Carbon Dot Nanoparticle Synthesis, there was three motivations for preparing a binder structure. The first motivation was having enough hydrophilicity for dispersing the aqueous carbon dots in the binder also having enough hydrophobicity for preventing complete wetting by the cellulose paper. The second one was having enough viscosity, enabling easy application onto the paper and the third motivation was preparing a binder formulation being colorless under daylight and UV light, in the absence of the aqueous carbon dot.

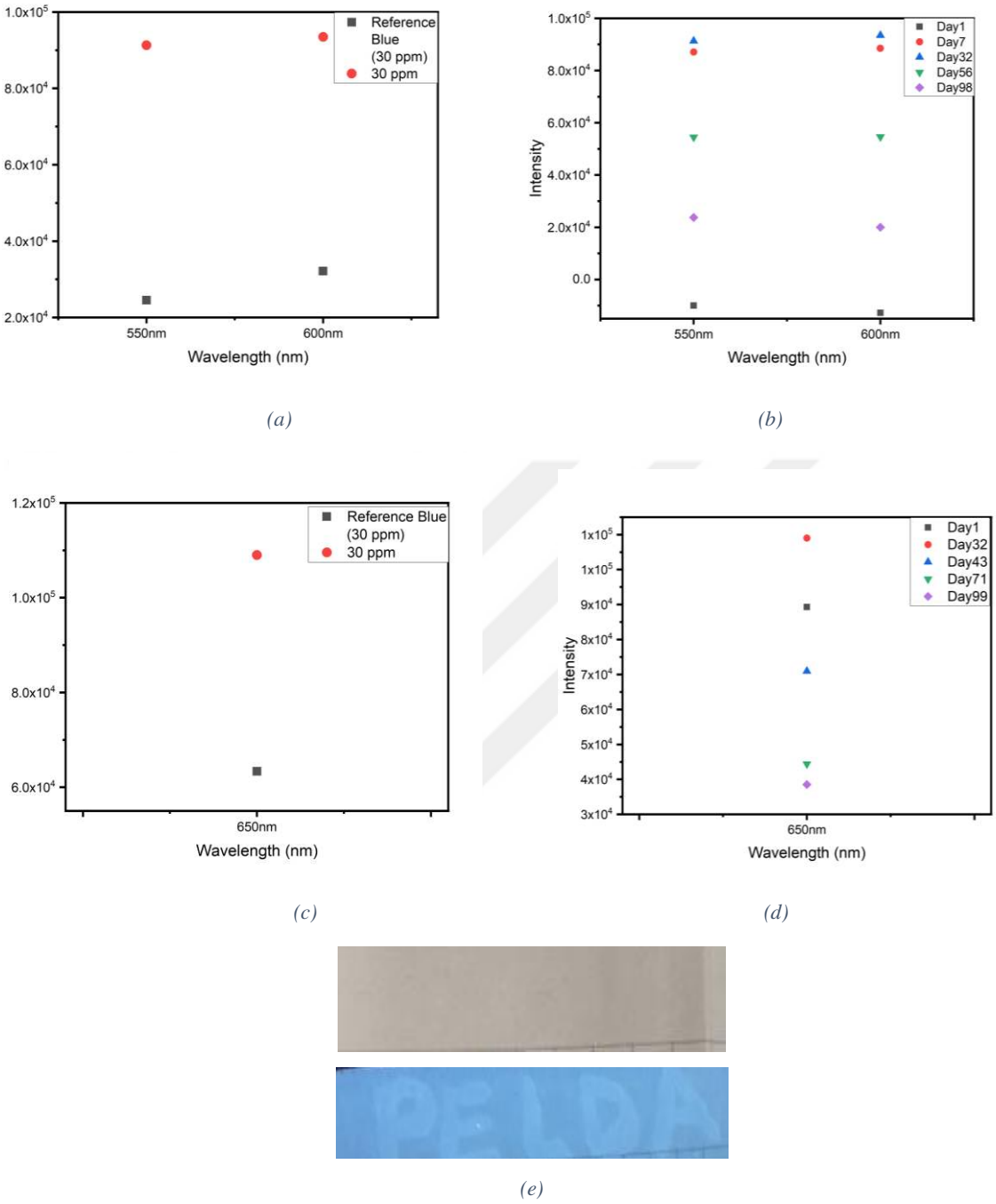

Figure 3.51: Emission comparison of 30 ppm CD18 loaded ink with respect to 30 ppm Reference Blue based ink, (a) with 405 nm sensor, (c) with 525 nm sensor. Stability of 30 ppm CD18 loaded ink (b) with 405 nm sensor, (d) with 525 nm sensor. (e) Day and UV light image of 30 ppm CD18 loaded ink.

In the prepared ink mixture, the dispersion of CD18 was 30 ppm (0.003 wt%). CD18, in solution form has an excitation independent emission, giving the maximum emission

intensity at 604 nm under 580 nm excitation. As it was expected from CD18 based ink on paper, measuring with 405 nm sensor gave the optimum emission lines at 550 nm and 600 nm (Figure 3.51.a) and measuring with 525 nm sensor gave the optimum emission line at 650 nm (Figure 3.51.c). Tracking the emission of CD18 based ink in above-mentioned emission channels, yielded higher emission intensities compared to the Quantag Reference Blue dot-based ink mixture at day 32. In the prepared ink mixture, the dispersion of CD24 was 30 ppm (0.003 wt%). CD24, in solution form has an excitation dependent emission, giving the maximum emission intensity at 450 nm under 380 nm excitation. As it was expected from CD24 based ink on paper, measuring with 405 nm sensor gave the optimum emission lines at 500 nm, 550 nm and 600 nm (Figure 3.52.a). Tracking the emission of CD24 based ink in above-mentioned emission channels, yielded higher emission intensities compared to the Quantag Reference Blue dot-based ink mixture at day 40.

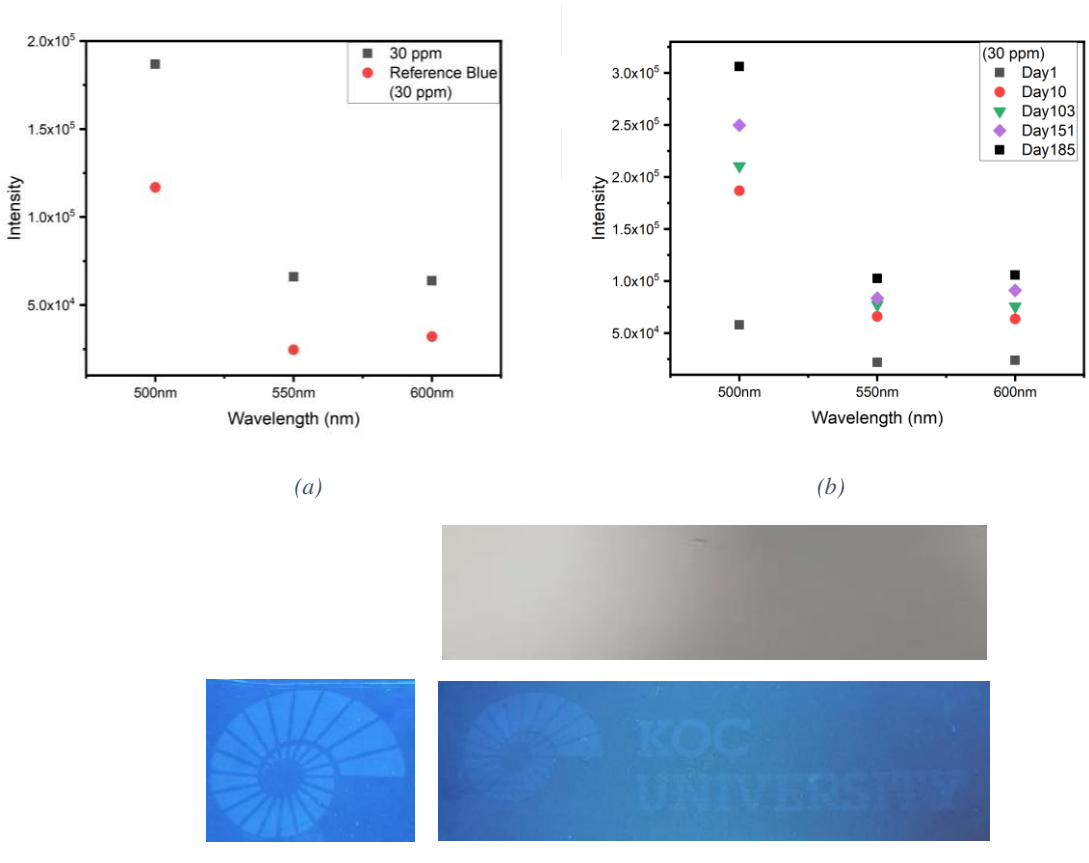

Figure 3.52: (a) Emission comparison of 30 ppm CD24 loaded ink with respect to 30 ppm Reference Blue based ink with 405 nm sensor, (b) Stability of 30 ppm CD24 loaded ink, (c) Day and UV light images of 30 ppm CD24 loaded ink.

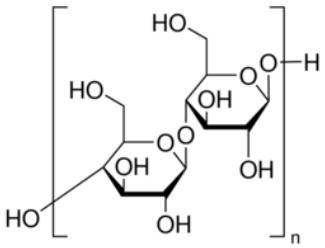

Figure 3.53: Cellulose structure (Sigma Aldrich , 2021).

CD18 and CD24 were nitrogen doped nanoparticles, having p-PDA and b-PEI as precursors, respectively. As it was assumed by their positive Zeta potentials (Table 3.5) and confirmed by their FTIR analysis (Figure 3.33.e), these particles have either pyridinic, pyrrolic (C=N) or primary amine groups on their surface, leading to a better dispersion in water. We knew that cellulose (paper material in Figure 3.53) is a polymer with hydrophilic ends, resulting in complete absorption of water molecules. To minimize the full wetting of cellulose paper surface by the CD-based inks, the inks were prepared having some hydrophobic nature fulfilling the first motivation. As cited in the related literature, we obtained blue emission from the printed patterns under UV light, independent of the color of emission in solution form (Pang, 2018). This might be resulted from using paper as a substrate, a different substrate might provide a different color of emission and wettability.

It is important to note that having a thin ink mixture would lead to applying less nanoparticle on the paper in each drop or brushstroke. We have observed that the prepared ink mixtures had enough viscosity due to the well-adjusted TEG/EG ratio in binder and they could easily be applied onto the paper, fulfilling the second motivation. These chemicals adjust the thickness of mixture and behave as stabilizer. In the literature there were some alternatives such as glycerol and the water-soluble polymers PEG and HEC (Fu, 2021). While water was evaporating, the form and shape of the figures set and remained the same due to having a binder material. We can develop the claim that the well-adjusted thickness of binder prevents the aggregation induced quenching, resulting from the Van der Waals interactions and hydrogen bonding between carbon dot nanoparticles. Since CD18-based ink on paper had an increasing emission intensity for 32 days (Figure 3.51.b and Figure 3.51.d) but only 3 weeks in solution form. Likewise, CD24-based ink on paper had an increasing emission intensity for more than 185 days

(Figure 3.52.b) but had a decreasing emission intensity which stabilized in week 8 in solution form.

Binder, in the absence of carbon dot, was transparent. Meanwhile, both CD18 and CD24 based printed patterns were invisible under daylight but became visible under UV light. With same nanoparticle dispersion (40 ppm), the commercial reference blue dot-based ink was slightly visible under UV light.

To eliminate the fluorescence of the commercial binder (used for organic based CDs) and to continue to have a viscous media, we replaced the commercial binder with a commercial transparent nail polish as binder material while loading the CD mixtures into it.

3.2.6 Security Tag Applications of CD mixtures

3.2.6.1 CD22-CD29

Under UV light, CD22 and CD29 emitted yellow and bluish white, respectively. As can be seen in Figure 3.54.a., under 405 nm excitation CD22 and CD29 have emissions respectively at 531 and 467 nm and under 525 nm excitation in Figure 3.54.b. they have emissions respectively at 623 and 576 nm. The motivation was combining two particles emitting different colors of radiation and investigating the crosstalk between them, as the emission or excitation of one particle may excite the other one. Particles were combined in varying ratios and under 405 nm and 525 nm excitations, the optical behavior of carbon dot mixtures were investigated to create optical barcodes.

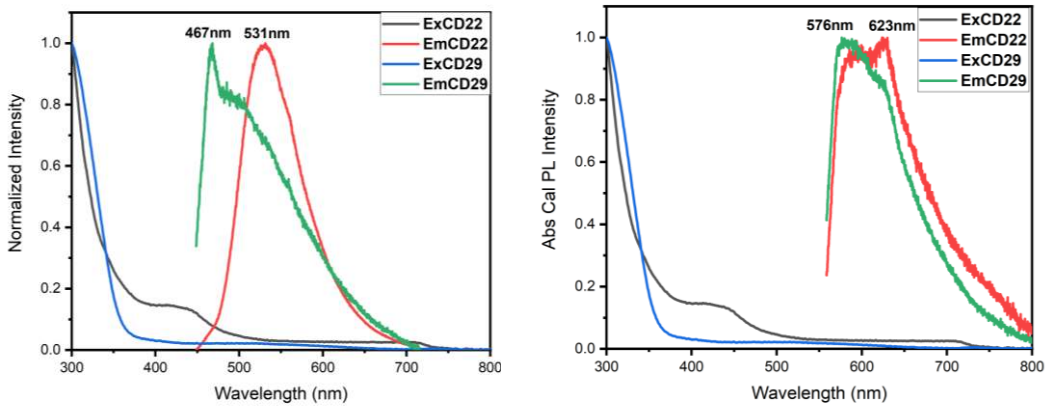

(a) *(b)*

Figure 3.54: PL Crosstalk of CD22 and CD29: (a) under 405 nm excitation, (b) under 525 nm excitation.

The below three graphs represented the PL emission of the CD mixtures (1-5, 2-4 and 3-3 ratios) under 405 and 525 nm excitation wavelengths with varying emission intensities at each point (Figure 3.55).

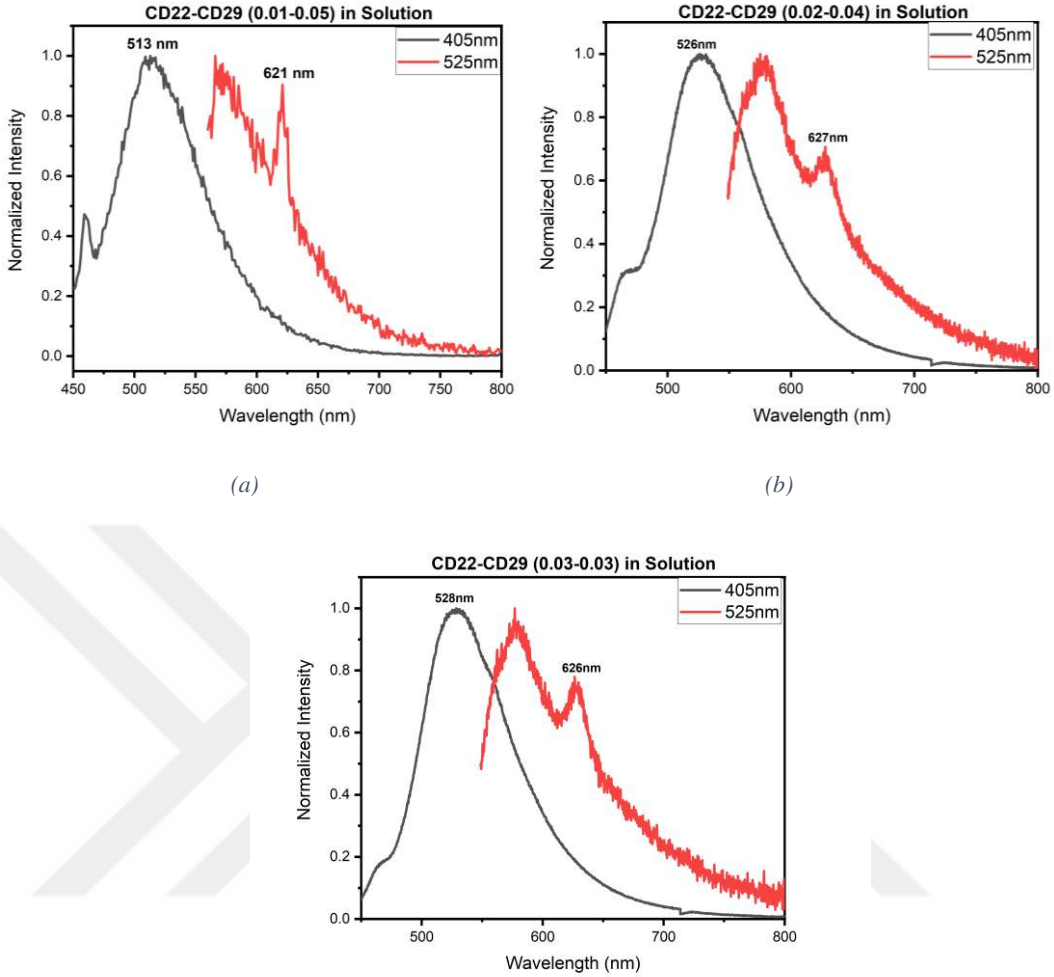

Figure 3.55: PL comparison of CD22-CD29 mixtures in solution with: (a) 0.01-0.05, (b) 0.02-0.04 and (c) 0.03-0.03 ratios.

It was observed that under both excitations, the CD mixtures displayed the emission characteristics of each indivudual particle. For instance under 525 nm excitation, the 0.03-0.03 ratio CD mixture emitted light at two points, 576 and 626 nm. While under same excitation wavelength single particles CD22 and CD29 emitted at 576 nm and 623 nm respectively, which implies the combination effect of the two particles.

We tried to create optical barcodes by dividing the minor emission coming from 525 nm excitation to the major emission coming from 405 nm excitation for each CD mixture combination (Figure 3.56.a).

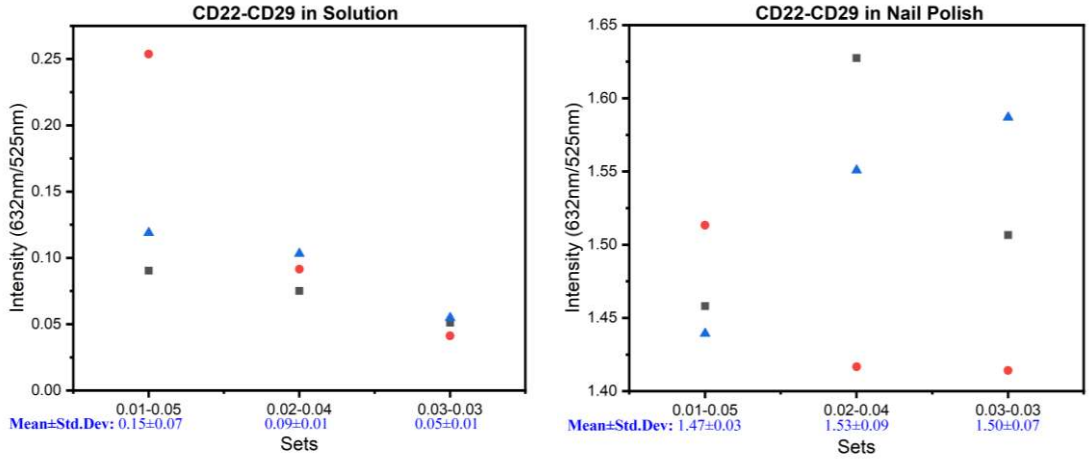

(a) *(b)*

Figure 3.56: CD22-CD29 mixtures: (a) in solution form, (b) in the nail polish as ink mixture.

Table 3.7: FL Lifetime of CD22, CD29 and several CD22-C29 mixtures.

Sample Name	Emission Point (nm)	Major Event (%)	Decay Time (T1) (ns)	Minor Event (%)	Decay Time (T2) (ns)	Average Decay Time (ns)
0.01-0.05	520	67.41	2.8	32.59	7.22	4.24
0.02-0.04	520	76.44	2.94	23.56	7.51	4.02
0.03-0.03	520	76.78	2.95	23.22	7.99	4.12
CD22	520	92.99	3.02	7.01	11.24	3.6
CD29	520	64.47	9.78	35.53	3.04	7.39

As can be seen in the solution test, the mean value of all ratios was so close to each other. After the solution test, the CDs were loaded in the same ratios to the commercial nail polish (Figure 3.56.b). Depending on the corresponding PL emission locations of the CD mixtures in solution form, the emission intensities of the CD mixture-based inks were tracked at 525 and 632 nm respectively by 405 nm and 525 nm sensors.

In the ink mixtures, it was observed that the difference between the standard deviations was comparable with the difference between the mean values. Apparently, neither the CD mixture solutions nor the CD mixture-based inks were applicable to be used as optical barcodes. As can be seen in Table 3.7, the PL lifetime of all the three ratios were comparable to the CD22. In terms of the average lifetime characteristics, CD mixture solutions with different ratios obviously didn't create optical barcodes.

3.2.6.2 CD01-CD12

Under UV light, CD01 and CD12 emitted yellow and bluish white respectively. As can be seen in Figure 3.57, under 405 nm excitation, CD01 and CD12 have emissions respectively at 552 and 451 nm, having a crosstalk in between them. The motivation for combining them in different ratios was obtaining different dominant emission intensities under 405 and 525 nm excitations to create optical barcodes.

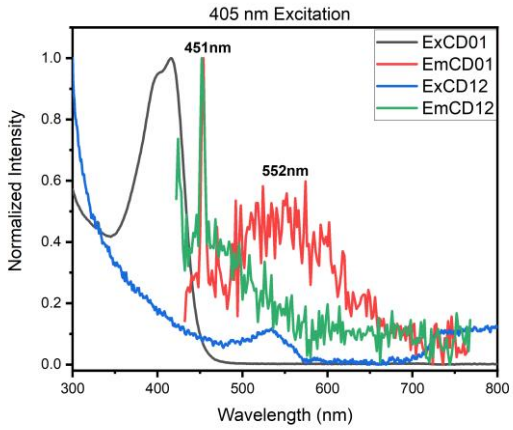

Figure 3.57: PL Crosstalk of CD01 and CD12 under 405 nm excitation.

To investigate the combination effect of the two particles mixture in solution form, each different ratio solution was irradiated at 405 and 525 nm respectively. The Figure 3.58 represented the PL emission spectra of the three CD mixtures (3-1, 1-3 and 2-2 ratio) at given excitation wavelengths with varying emission intensities.

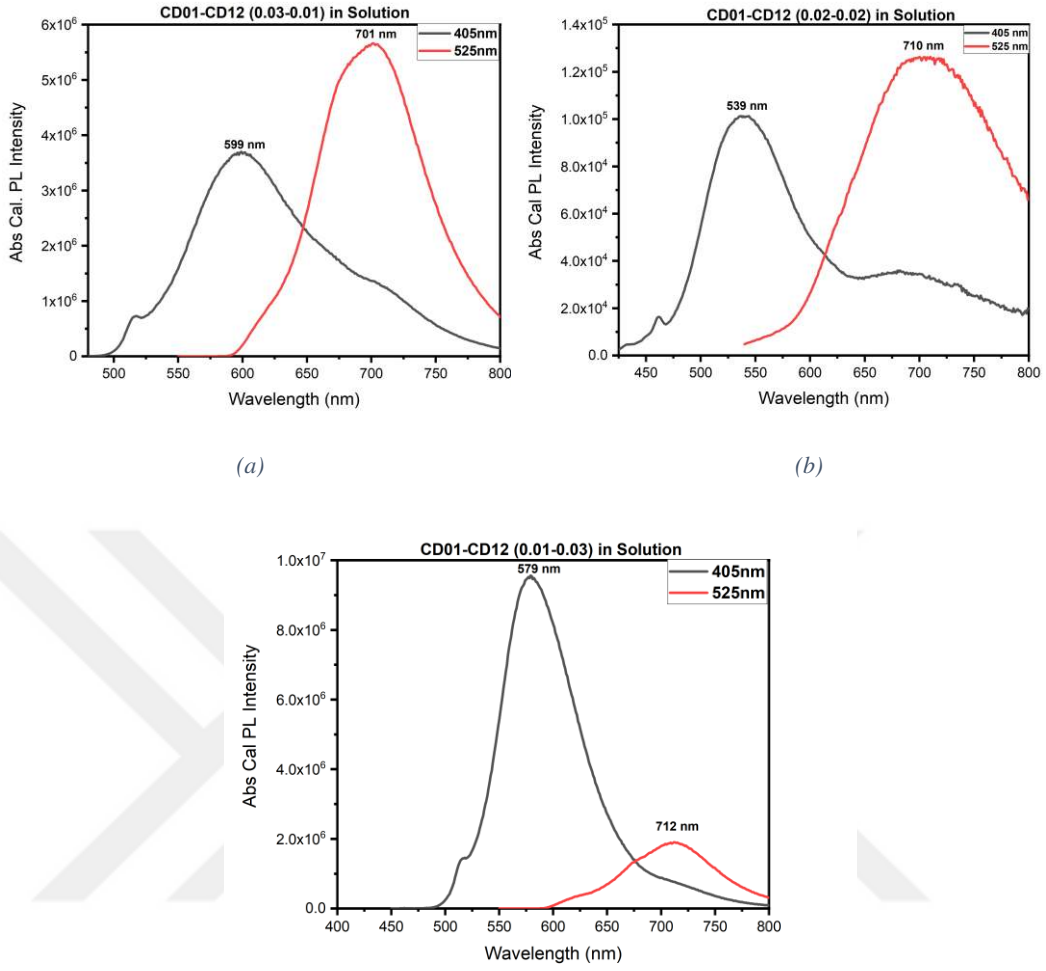

Figure 3.58: PL comparison of CD01-CD12 mixtures in solution with: (a) 0.03-0.01, (b) 0.02-0.02 and (c) 0.01-0.03 ratios.

It is important to note that under 405 nm excitation the individual particles CD01 and CD12 emitted at 552nm and 451 nm respectively, however the CD mixture emitted nearly at 600 nm. This indicated that during combination of these two particles there occurs an energy transfer from one another.

To summarize solution test, the below figure was created, in which the two emission intensities obtained by 405 and 525 nm excitations were divided into each other (Figure 3.59.a).

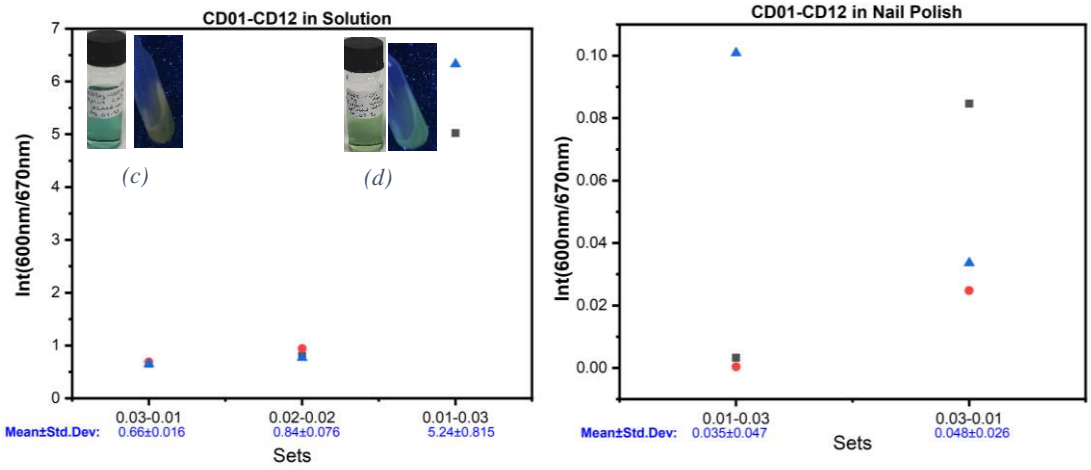

Figure 3.59: CD01-CD12 mixtures: (a) in solution form, (b) in the nail polish as ink mixture. UV light image of: (c) 0.03-0.01 mixture in solution, (d) 0.01-0.03 mixture in solution.

Table 3.8: FL Lifetime of CD01, CD12 and several CD01-CD12 mixtures.

Sample Name	Emission Point (nm)	Major Event (%)	Decay Time (T1) (ns)	Minor Event (%)	Decay Time (T2) (ns)	Average Decay Time (ns)
0.01-0.05	520	75.06	2.18	24.94	5.78	3.08
0.02-0.04	520	63.02	7.41	36.98	1.89	5.39
CD01	520	67.42	2.2	32.58	4.39	2.91
CD12	520	67.79	8.2	32.21	2.39	6.33

As can be seen in the solution test, among the three sets the mean value of the 1-3 and 2-2 were so close and 1-3 loading has larger a difference with 3-1 ratio. This brought the elimination of the 2-2 ratio as an optical barcode. In solution 1-3 ratio was emitting green and 3-1 ratio was emitting orange under UV (365 nm) light. After the solution test, CDs were loaded in resulting two ratios (1-3 and 3-1) to the nail polish (Figure 3.59.b). Depending on the corresponding PL emission locations of the CD mixtures in solution, the emission intensities of the inks were tracked at 600 nm and 670 nm respectively by 405 nm and 525 nm sensors. In the ink mixtures, it was observed that the difference between the standard deviations was higher than the difference between the mean values. Apparently, in paper applied form these two sets were not applicable to be used as optical barcodes. However, in solution forms the change in the average lifetime from 3.08 ns to

5.39 ns in Table 3.8: FL Lifetime of CD01, CD12 and several CD01-CD12 mixtures. 8 and the change in the PL emission mechanism, which was understood from the major event change, provided confirmatory evidence that the CD mixtures were good candidates as solution-based barcodes.

3.2.6.3 AICD01-CD22

There were two motivations for combining these two nanoparticles. The first one was the large difference in the highest intensity emission points of individual particles, making these particles a good pair to create barcode. As discussed before, both particles exhibit excitation independent emissions at 596 nm and 440nm/513nm, respectively for AI-CD01 and CD22. Combining them in different ratios might lead to different dominant emission intensities at 405 and 525 nm excitations, creating barcode.

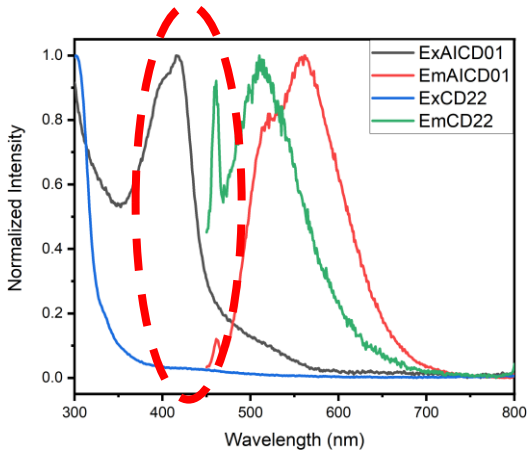

Figure 3.60: PL Crosstalk of AI-CD01 and CD22.

Second motivation was forming a FRET pair. At 405 nm excitation (Figure 3.60) the PL emission of CD22 overlapped with the absorbance of AI-CD01. Based on the evidence currently available, it seemed fair to suggest that spectral overlap led to formation of FRET pair, in which CD22 acted as an excited FRET donor and AI-CD01 acted as an acceptor. Due to the FRET tunneling, energy was transferred non-radiatively from CD22 to AI-CD01.

As can be seen in Figure 3.61, the CD mixture developed new emission centers, differing from the emission points of AI-CD01 and CD22, meaning that the mixtures

didn't directly mimic the PL behavior of one particle. The CD mixtures emitted at 525 nm and 650 nm, when they were excited respectively at 405 and 525nm. As the longer emitting particle AI-CD01 (596 nm) was superior in amount with respect to shorter emitting particle CD22 (440 and 513 nm) in the mixture, emission of CD mixture at longer wavelength (650 nm) strengthened and emission at shorter wavelength (525 nm) weakened.

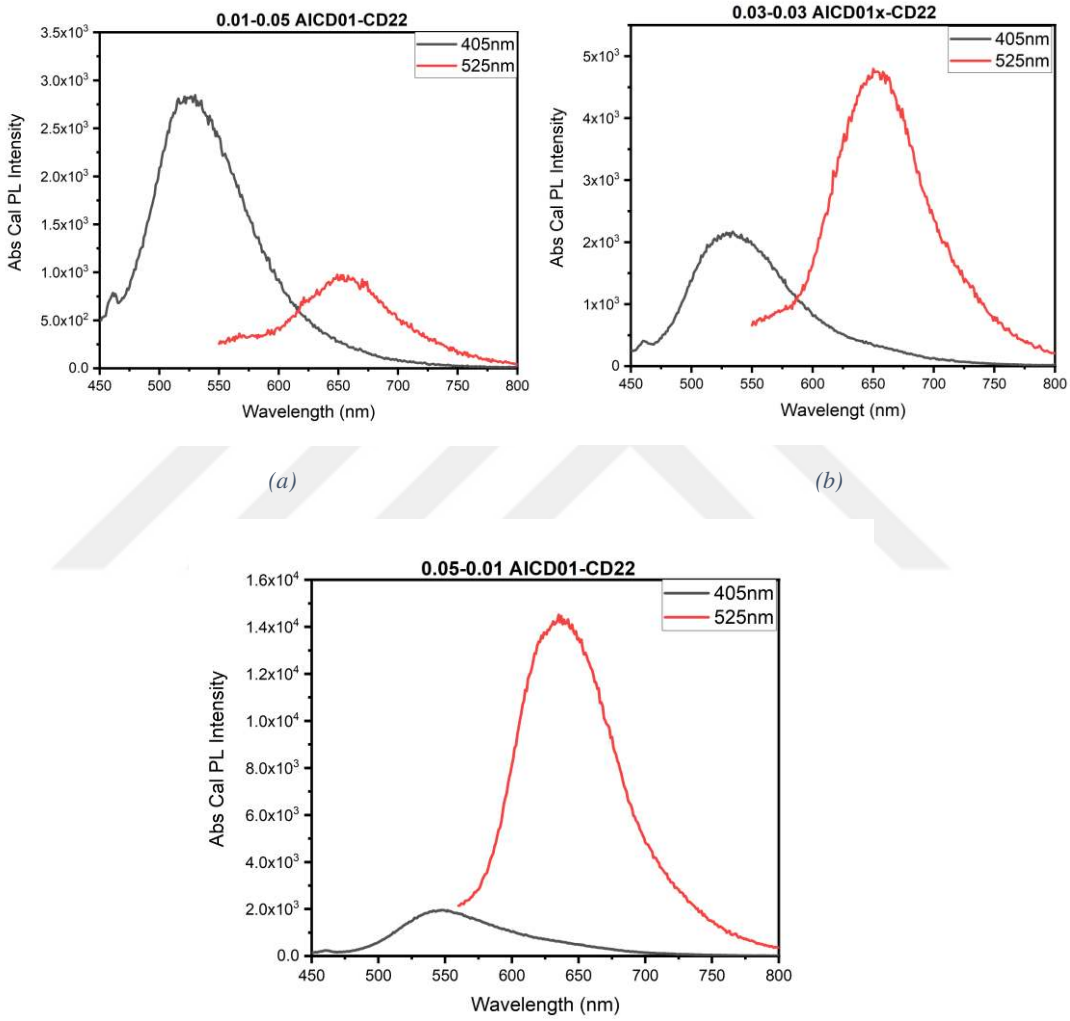

(a) *(b)*

(c)

Figure 3.61: PL comparison of AICD01-CD22 mixtures in solution with: (a) 0.01-0.05, (b) 0.03-0.03 and (c) 0.05-0.01 ratios.

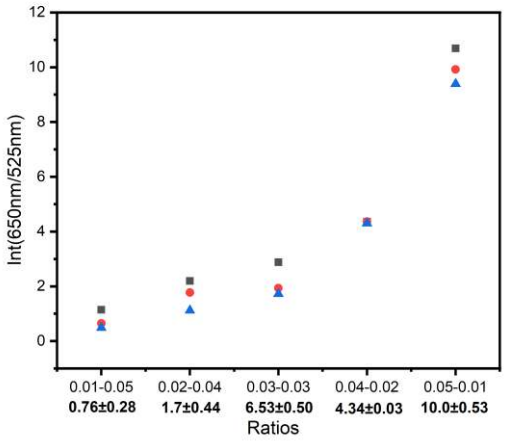

Figure 3.62: AICD01-CD22 mixtures in solution form.

As a result of the different emission intensities of each CD mixture, under 405 and 525 nm excitations, five barcodes were created in solution. These barcodes in Figure 3.62 were created as the division of the emission intensity obtained from 650 nm to the 525 nm.

A closer look to the Time Resolved Photoluminescence study in Table 3.9 indicated the lifetime relevance between the nanoparticles and their mixtures. As expected, the abundant nanoparticle in the CD mixture dominated the PL lifetime characteristics. To illustrate, from 0.01-0.05 to 0.05-0.01, the abundant CD nanoparticle changes from CD22 (5.27 ns) to AI-CD01 (3.35 ns), leading to the average lifetime change from 5.77 ns to 3.51 ns. Starting from the 0.03-0.03 to 0.05-0.01, lifetime of CD mixtures showed similarity with AI-CD01, accompanied by a PL emission pathway change with respect to the 0.01-0.05 and 0.02-0.04 ratios. Since in 0.01-0.05 and 0.02-0.04 ratios, the major event was the longer PL decay, whereas from 0.03-0.03 to 0.05-0.01 the major event was the shorter PL decay. The average lifetime of different mixtures provided lifetime encoded barcodes.

Due to FRET tunneling and nonradiative energy transfer from CD22 to AI-CD01, the PL lifetime of the excited chromophore (CD22) decreased from 5.27 ns to 3.42 ns, when AI-CD01 is added in 0.03-0.03 ratio (Figure 3.63). The 0.03-0.03 ratio was the optimum combination between the particles, taking into consideration that the lifetime of CD22 decreased the most. It is important to note that, FL lifetime decrease is a hallmark of FRET tunnelling.

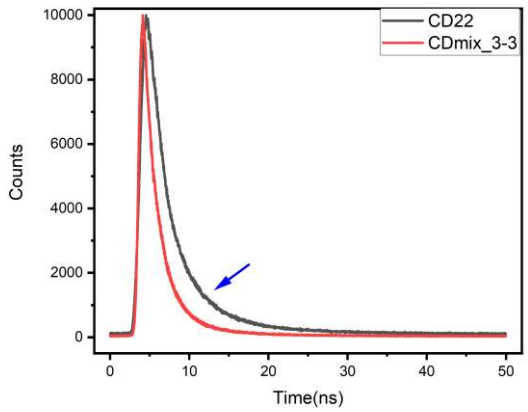

Figure 3.63: FL Lifetime comparison of CD22 and 0.03-0.03 mixture.

By utilizing the lifetime of 0.03-0.03 mixture and CD22 (donor) alone, the FRET efficiency was yielded as E=35%. Through nonradiative energy transfer from the donor to acceptor, PL of the donor particles quenches in each acceptor particle addition. In my studies FRET pair (CD22-AICD01) didn't show PL emission peaks corresponding to the individual particles. Therefore, the PL quenching through nonradiative energy transfer couldn't be observed in the PL emission spectra of FRET pair.

Table 3.9: FL Lifetime of AICD01, CD22 and several AICD01-CD22 mixtures.

Sample Name	Emission Point (nm)	Major Event (%)	Decay Time (T1) (ns)	Minor Event (%)	Decay Time (T2) (ns)	Average Decay Time (ns)
1-5	520	53.77	8.62	46.23	2.46	5.77
2-4	520	59.59	9.97	40.41	2.24	6.85
3-3	520	69.0	1.88	31.0	6.85	3.42
4-2	520	84.1	14.33	15.9	1.94	12.4
5-1	520	51.8	2.2	48.2	4.91	3.51
AI-CD01	520	57.89	4.27	42.11	2.09	3.35
CD22	520	52.71	2.86	47.29	7.96	5.27

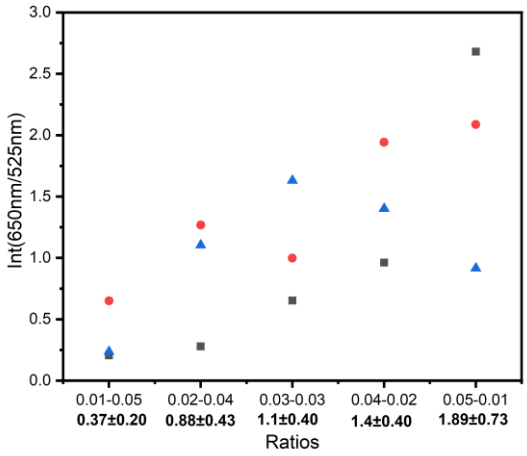

Figure 3.64: AICD01-CD22 mixtures: in the nail polish as ink mixtures.

By keeping the total carbon dot loading the same, particles were loaded in varying amounts to the nail polish (Figure 3.64). The difference in standard deviations between each mixture were lower than the difference in mean values. As confirmed by the solution test, five different barcodes were created on paper. The CD mixtures were stable in the binder more than 37 days (5weeks).

*3.3 **Conclusion***

In this thesis, I proposed 4 organic and 2 aqueous-based CDs emitting bluish white, yellow, cyan, and orange. The UV irradiation treatment led to photooxidation of CD01 surface and a change in the PL behavior. After UV irradiation, the PL emission intensity has increased 10-fold and PL QY has increased 20-fold. The AI-CD01 and CD01 were more stable in paper applied ink form than in solution form, meaning that binder prevents the aggregation and nonradiative energy transfer between nanoparticles. The 100 ppm organic CDs (yellow, orange) based inks have stronger PL intensity with respect to the Reference red particle-based ink. The yellow CD inks have 1.5-fold and the orange CD inks have 8 fold stronger PL intensity than Reference red ink. They had an increasing emission intensity on the paper substrate for 4.5 months and 4 months, respectively. The 30 ppm aqueous CDs (cyan, bluish white) based inks have stronger PL intensity with respect to the Reference blue CD-based ink. The bluish white CD inks have 4.5-fold, and

the cyan CD inks have 1.5-fold stronger PL intensity than Reference blue ink. The cyan CD ink was increasing emission intensity on the paper substrate for 6 months. It is important to note that the aqueous CD inks on paper substrate were invisible under daylight but visible under UV light.

CHAPTER 4 PERSPECTIVES

To provide a new perspective and optimize the PL characteristics of CD01, the CD01 solution can be photo-irradiated by various sources, such as 405 nm (violet-blue), 635 nm (red) and 808 nm (NIR) lasers, for different time intervals. In this way for each different set, both the morphological and structural changes that affect the PL emission, can be tracked. Instead of the carbon dot solution, the carbon dot powder can be irradiated and then dispersed in different solvents to validate the solvatochromic behavior (Alaş, 2021).

As previously mentioned and illustrated in Figure 3.16, CD18 has excitation dependent PL emission. Therefore, with different excitation/emission filters, the FL Microscope images of CD18 solution gave a range of colors. As a further perspective, FL Microscope images of the figure created by CD18 based ink can be taken with different excitation/emission filters. In this way, one ink formulation can provide different color emissions.

Enhancing the security level and providing multiple encryptions is a prominent objective in anticounterfeiting applications. As we know, the aqueous based CD18 (Figure 3.43.a) and CD24 (Figure 3.44.a) were emitting in different parts of the electromagnetic spectrum. As we previously succeeded in several particles, CD mixtures, containing different ratios of CD18 and CD24, can be formed. Each mixture will have a different dominant luminescent center and FL lifetime. Using these different mixtures, a single figure can be prepared. Each different mixture can be applied onto a different part of the figure. This may accomplish decoding the figure with FL Lifetime imaging (FLI), like in Figure 2.5.

CDs are surrounded by various surface functional groups. Like a previous study of our research group, we assumed that UV light irradiation of the carbon dot (TNP in water) surface leads to decarboxylation and a free radical will form on the alkyl group (R*) (Dadashi-Silab et al., 2015). That free radical on CDs surface will act as a photo-initiator in the polyethylene glycol diacrylate (PEGDA) photopolymerization. When PEGDA (monomer) was mixed with TNP in water (photo initiator) and UV light irradiated, the whole system gelled, and the gel was emitting yellow under UV light (Figure 4.1). When control experiment was performed in the absence of CDs, PEGDA

has still gelled and has no emission under UV light. This brought the idea that CDs didn't take role as a free radical photo initiator in the photopolymerization of PEGDA, but it assisted the formation of carbon dot embedded luminescing PEGDA gels (CD-PEGDA nanocomposites). As a new perspective and a further study, different color emissive composites can be prepared by using different monomers. Different monomers act as different media, and the change in the environment leads to a change in the emission color of the embedded CDs (Li et al., 2014).

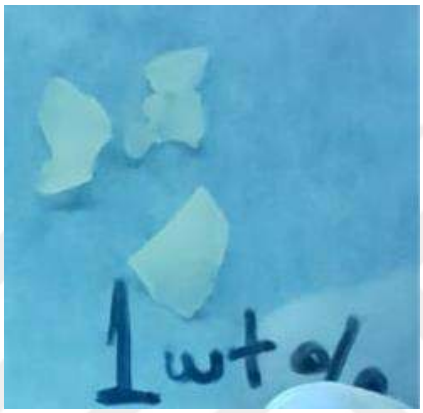

Figure 4.1: TNP in water-PEGDA nanocomposite.

Apart from the study of our group, carbon dots were not capped by fatty acids, such as lauric or oleic acid (Dadashi-Silab, 2015). Lastly, their surface can be coated to utilize the CDs as effective free radical photo-initiators.

BIBLIOGRAPHY

Alas, M. O. (2020). Fluorescent carbon dots are the new quantum dots: an overview of their potential in emerging technologies and nanosafety. *Materials Science, 55*(31), 15074–15105. doi:10.1007/s10853-020-05054-y

Alaş, M. Ö. (2021). Solvatochromic Surface-Passivated Carbon Dots for Fluorometric Moisture Sensing in Organic Solvents. *ACS Applied Nano Materials, 4*(8), 7974–7987. doi:10.1021/ACSANM.1C01282

Anand, S. R. (2019). Antibacterial Nitrogen-doped Carbon Dots as a Reversible "fluorescent Nanoswitch" and Fluorescent Ink. *ACS Omega, 4*(1), 1581–1591. doi:10.1021/acsomega.8b03191

Asghar, K. Q. (2017). One-pot green synthesis of carbon quantum dot for biological application. *AIP Conference Proceedings, 1832*(1). doi:10.1063/1.4980350

Bao, L. L. (2015). Photoluminescence-tunable carbon nanodots: surface-state energy-gap tuning. *Advanced Materials, 27*(10), 1663–1667. doi:10.1002/ADMA.201405070

Bartolomei, B. D. (2021). New trends in nonconventional carbon dot synthesis. *Trends in Chemistry, 3*(11), 943–953. doi:10.1016/J.TRECHM.2021.09.003

Bhati, A. A. (2018). Self-doped nontoxic red-emitting Mg-N-embedded carbon dots for imaging, Cu(ii) sensing and fluorescent ink. *New Journal of Chemistry, 42*(24), 19548–19556. doi:10.1039/c8nj04754e

Bhattacharyya, S. &. (2011). Intracellular probes. *Comprehensive Biomaterials , 3*, 447–470. doi:10.1016/b978-0-08-055294-1.00117-3

Bhattacharyya, S. E. (2017). Effect of nitrogen atom positioning on the trade-off between emissive and photocatalytic properties of carbon dots. . *Nature Communications, 8*(1), 1-9. doi:10.1038/s41467-017-01463-x

Busnelli, M. M. (2013). Analysis of GPCR Dimerization Using Acceptor Photobleaching Resonance Energy Transfer Techniques. In *Methods in Enzymology* (Vol. 521, pp. 311–327). doi:10.1016/B978-0-12-391862-8.00017-X

Chandra, S. P. (2014). High throughput electron transfer from carbon dots to chloroplast: a rationale of enhanced photosynthesis. *Nanoscale, 6*(7), 3647–3655. doi:10.1039/C3NR06079A

Chem UCLA. (2021). Retrieved from https://www.chem.ucla.edu/~bacher/UV-vis/uv_vis_tetracyclone.html

Chen, J. C. (2012). Influence of surface functionalization via chemical oxidation on the properties of carbon nanotubes. *Journal of Colloid and Interface Science, 370*(1), 32–38. doi:10.1016/J.JCIS.2011.12.073

Chen, J. W. (2017). Red-Emissive Carbon Dots for Fingerprints Detection by Spray Method: Coffee Ring Effect and Unquenched Fluorescence in Drying Process. *ACS Applied Materials and Interfaces, 9*(22), 18429–18433. doi:10.1021/ACSAMI.7B03917

Chen, L. H. (2019). A facile synthesis of 1,3,6,8-pyrenesulfonic acid tetrasodium salt as a hydrosoluble fluorescent ink for anti-counterfeiting applications. *RSC Advances, 9*(1), 476–481. doi:10.1039/C8RA09106D

Chen, Q. L. (2019). Construction of highly fluorescent N–O seven-membered heterocycles via thermo-oxidation of oxazolidines. . *Journal of Materials Chemistry C, 7*(26), 8045–8052. doi:10.1039/C9TC01199D

Chini, M. K. (2019). Graphene quantum dots and carbon nano dots for the FRET based detection of heavy metal ions. *Nano-Structures & Nano-Objects*. doi:10.1016/J.NANOSO.2019.100347

Crista, D. M. (2020). Evaluation of Different Bottom-up Routes for the Fabrication of Carbon Dots. *Nanomaterials, 10*(7), 1316. doi:10.3390/NANO10071316

Dadashi-Silab, S. Y. (2015). Magnetic iron oxide nanoparticles as long wavelength photoinitiators for free radical polymerization. *Polymer Chemistry, 6*(11), 1918–1922. doi:10.1039/C4PY01658K

Dager, A. U. (2019). Synthesis and characterization of Mono-disperse Carbon Quantum Dots from Fennel Seeds: Photoluminescence analysis using Machine Learning. *Scientific Reports, 9*(1), 1–12. doi:10.1038/s41598-019-50397-5

Ding, H. L. (2020). Surface states of carbon dots and their influences on luminescence. *Journal of Applied Physics, 127*(23), 231101. doi:10.1063/1.5143819

Ding, H. Y. (2016). Full-color light-emitting carbon dots with a surface-state-controlled luminescence mechanism. *ACS Nano, 10*(1), 484–491. doi:10.1021/ACSNANO.5B05406

Douglas A. Skoog, F. J. (2018). *Principles of Instrumental Analysis.* Cengage.

Emrooz, H. B. (2021). Zinc-salt assisted synthesis of three-dimensional oxygen and nitrogen co-doped hierarchical micro-meso porous carbon foam for supercapacitors. *Scientific Reports, 11*(1), 1-11. doi:10.1038/s41598-021-01151-3

Fu, X. L. (2021). Color-switchable hybrid dots/hydroxyethyl cellulose ink for anti-counterfeiting applications. *Carbohydrate Polymers*. doi:10.1016/j.carbpol.2020.117084

Gasiorowski-Denis, E. (2014). *CRACKDOWN ON COUNTERFEITING*. Retrieved from https://www.iso.org/news/2014/01/Ref1809.html

Geiger, C. (2012). *Criminal Enforcement of Intellectual Property: A Handbook of Contemporary Research.* Edward Elgar Publishing.

Geng, B. Y. (2018). NIR-responsive carbon dots for efficient photothermal cancer therapy at low power densities. *Carbon, 134*, 153–162. doi:10.1016/J.CARBON.2018.03.084

Gómez, I. J. (2021). Exploring the Emission Pathways in Nitrogen-Doped Graphene Quantum Dots for Bioimaging. *Journal of Physical Chemistry C, 125*(38), 21044–21054. doi:10.1021/ACS.JPCC.1C06029

Griffin, W. C. (1949). Classification of Surface-Active Agents by HLB. *Journal of the Society of Cosmetic Chemists, 1*(5), 311-326.

Guo, Y. Z. (2019). Green fluorescent carbon quantum dots functionalized with polyethyleneimine, and their application to aptamer-based determination of thrombin and ATP. *Microchimica Acta, 186*(11), 1–8. doi:10.1007/S00604-019-3874-Y/TABLES/1

Haase, M. &. (n.d.). Upconverting Nanoparticles. *Angewandte Chemie International Edition, 50*(26), 5808–5829. doi:10.1002/anie.201005159

Han, Z. H. (2020). Hydrothermal synthesis of carbon dots and their application for detection of chlorogenic acid. *Luminescence, 35*(7), 989–997. doi:10.1002/BIO.3803

Holá, K. S. (2017). Graphitic Nitrogen Triggers Red Fluorescence in Carbon Dots. *ACS Nano, 11*(12), 12402–12410. doi:10.1021/acsnano.7b06399

Houghton, R. A. (2003). The Contemporary Carbon Cycle. In *Treatise on Geochemistry* (Vols. 8–9, pp. 473–513). doi:10.1016/B0-08-043751-6/08168-8

Hu, L. S. (2014). Multifunctional carbon dots with high quantum yield for imaging and gene delivery. *Carbon, 67*, 508–513. doi:10.1016/J.CARBON.2013.10.023

Iijima, S. (1991). Helical microtubules of graphitic carbon. *Nature, 354*(6348), 56–58. doi:10.1038/354056a0

Itoh, T. (.–4. (2012). Fluorescence and Phosphorescence from Higher Excited States of Organic Molecules. *Chemical Reviews, 112*(8), 4541–4568. doi:10.1021/CR200166M

IYTE. (2021). Retrieved from http://web.iyte.edu.tr/~serifeyalcin/lectures/chem305/cn_7.pdf

Jariwala, D. S. (2013). Carbon nanomaterials for electronics, optoelectronics, photovoltaics, and sensing. *Chemical Society Reviews, 42*(7).

Jia, H. W. (2019). Electroluminescent Warm White Light-Emitting Diodes Based on Passivation Enabled Bright Red Bandgap Emission Carbon Quantum Dots. *Advanced Science, 6*(13). doi:10.1002/ADVS.201900397

Jiang, K. S. (2015). Red, Green, and Blue Luminescence by Carbon Dots: Full-Color Emission Tuning and Multicolor Cellular Imaging . *Angewandte Chemie, 127*(18), 5450–5453. doi:10.1002/ANGE.201501193

Kalsi, P. S. (2007). Spectroscopy of organic compounds. New Age International.

Kalytchuk, S. W. (2018). Carbon Dot Fluorescence-Lifetime-Encoded Anti-Counterfeiting. *ACS Applied Materials and Interfaces, 10*(35), 29902–29908. doi:10.1021/acsami.8b11663

Khan, W. U. (2017). High Quantum Yield Green-Emitting Carbon Dots for Fe(III) Detection, Biocompatible Fluorescent Ink and Cellular Imaging. *Scientific Reports, 7*(1), 1–9. doi:10.1038/s41598-017-15054-9

Kouznetsov, C. A. (2016). “Green” Quantum Dots: Basics, Green Synthesis, and Nanotechnological Applications. In *Green Nanotechnology - Overview and Further Prospects.* doi:10.5772/62327

Kroto, H. (1993). The Birth of C60: Buckminsterfullerene. In H. Kroto, *Electronic Properties of Fullerenes* (pp. 1–7). Springer. doi:10.1007/978-3-642-85049-3_1

L.E., M. (2015). Classifications and Structures of Nanomaterials. In M. L.E., *Handbook of Materials Structures, Properties, Processing and Performance* (pp. 719-746). Springer. doi:https://doi.org/10.1007/978-3-319-01815-7_45

Lakowicz, J. R. (2006). *Principles of fluorescence spectroscopy.* doi:10.1007/978-0-387-46312-4

Lee, U. H. (2021). Carbon dots for epoxy curing: Anti-forgery patterns with long-term luminescent stability. . *Chemical Engineering Journal*. doi:10.1016/J.CEJ.2020.126988

Li, L. &. (2018). Photoluminescence tuning in carbon dots: Surface passivation or/and functionalization, heteroatom doping. *Materials Chemistry C, 6*(30), 7944–7970. doi:10.1039/c7tc05878k

Li, X. R. (2020). Modulating the local coordination environment of single-atom catalysts for enhanced catalytic performance. *Nano Research, 13*(7), 1842–1855. doi:10.1007/s12274-020-2755-3

Li, X. Y. (2019). Tuning the photoluminescence property of carbon dots by ultraviolet light irradiation. *RSC Advances, 9*(22), 12732–12736. doi:10.1039/C9RA02080B

Li, X. Z. (2014). Engineering surface states of carbon dots to achieve controllable luminescence for solid-luminescent composites and sensitive Be2+ detection. *Scientific Reports, 4*(1), 1-8. doi:10.1038/srep04976

Lin, S. L. (2017). Solvatochromism of bright carbon dots with tunable long-wavelength emission from green to red and their application as solid-state materials for warm WLEDs. *RSC Advances, 7*(66), 41552–41560. doi:10.1039/C7RA07736J

Liu, H. L. (2018). Synthesis of Luminescent Carbon Dots with Ultrahigh Quantum Yield and Inherent Folate Receptor-Positive Cancer Cell Targetability. *Scientific Reports, 8*(1). doi:10.1038/s41598-018-19373-3

Liu, J. L. (2020). Carbon Dots: A New Type of Carbon-Based Nanomaterial with Wide Applications. *ACS Central Science, 6*(12), 2179–2195. doi:10.1021/ACSCENTSCI.0C01306

Liu, M. L. (2019). Carbon dots: Synthesis, formation mechanism, fluorescence origin and sensing applications. *Green Chemistry, 21*(3), 449–471. doi:10.1039/c8gc02736f

Liu, M. L. (2019). Carbon dots: Synthesis, formation mechanism, fluorescence origin and sensing applications. *Green Chemistry , 21*(3), 449–471. doi:10.1039/c8gc02736f

Lu, S. S. (2017). Near-Infrared Photoluminescent Polymer–Carbon Nanodots with Two-Photon Fluorescence. *Advanced Materials, 29*(15). doi:10.1002/ADMA.201603443

M., E. (2014). *Performance enhancement of hybrid nanocrystal-polymer bulk heterojunction solar cells : aspects of device efficiency, reproducibility, and stability.*

Mandani, S. S. (2016). White light emission by controlled mixing of carbon dots and rhodamine B for applications in optical thermometry and selective Fe3+ detection. *RSC Advances, 6*(88), 84599–84603. doi:10.1039/C6RA17306C

Matsoso, B. J. (2016). Time-dependent evolution of the nitrogen configurations in N-doped graphene films. *RSC Advances, 6*(108), 106914–106920. doi:10.1039/C6RA24094A

Mauter, M. S. (2008). Environmental Applications of Carbon-Based Nanomaterials. In *Environmental Science and Technology* (Vols. 42(16):5843–59).

Mizobe, Y. I. (n.d.). A novel strategy for fluorescence enhancement in the solid-state: affording rigidity to fluorophores packing. *Chemical Communications, 20*, 2126–2128. doi:10.1039/B517687E

Müller Kerstin, E. B. (2017). Review on the Processing and Properties of Polymer Nanocomposites and Nanocoatings and Their Applications in the Packaging, Automotive and Solar Energy Fields. *Nanomaterials*.

Naghshbandi, M. P. (2020). Stabilization of phytase on multi-walled carbon nanotubes via covalent immobilization. *Methods in Enzymology*, 431–451. doi:10.1016/BS.MIE.2019.10.013

Nakama, Y. (2014). Surfactants. In *Cosmetic Science and Technology: Theoretical Principles and Applications* (pp. 231-244). doi:10.1016/B978-0-12-802005-0.00015-X

Nunney, T. &. (2011). Characterizing Materials for Energy Generation Using X-ray Photoelectron Spectroscopy (XPS). *Microscopy Today, 19*(2), 22-28. doi:10.1017/S1551929511000022

Ostyn, N. R. (2019). Low-temperature activation of carbon black by selective photocatalytic oxidation. *Nanoscale Advances, 1*(8), 2873–2880. doi:10.1039/C9NA00188C

Pang, Y. Z. (2018). Facile preparation of N-doped graphene quantum dots as quick-dry fluorescent ink for anti-counterfeiting. *New Journal of Chemistry, 42*(20), 17091–17095. doi:10.1039/c8nj03375g

Papaioannou, N. T. (2019).). Investigating the Effect of Reaction Time on Carbon Dot Formation, Structure, and Optical Properties. *ACS Omega, 4*(26), 21658–21665. doi:10.1021/ACSOMEGA.9B01798

Permatasari, F. A. (2016). Role of C–N Configurations in the Photoluminescence of Graphene Quantum Dots Synthesized by a Hydrothermal Route. *Scientific Reports, 6*(1), 1-8. doi:10.1038/srep21042

Permatasari, F. A. (2018). Design of Pyrrolic-N-Rich Carbon Dots with Absorption in the First Near-Infrared Window for Photothermal Therapy. *ACS Applied Nano Materials, 1*(5), 2368–2375. doi:10.1021/ACSANM.8B00497

Puvvada, N. K. (2012). Synthesis of biocompatible multicolor luminescent carbon dots for bioimaging applications. doi:10.1088/1468-6996/13/4/045008

Qu, D. Z. (2014). Formation mechanism and optimization of highly luminescent N-doped graphene quantum dots. *Scientific Reports, 4*(1), 1-11. doi:10.1038/srep05294

Rabchinskii, M. K. (2020). From graphene oxide towards aminated graphene: facile synthesis, its structure and electronic properties. *Scientific Reports, 10*(1), 1-12. doi:10.1038/s41598-020-63935-3

S. H. Jin, H. K. (2013). Tuning the photoluminescence of graphene quantum dots through the charge transfer effect of functional groups," ACS Nano 7(2), 1239–1245 (2013). *ACS Nano, 7*(2), 1239–1245.

Sadjadi, S. (2021). The utility of carbon dots for photocatalysis. In *Emerging Carbon Materials for Catalysis* (pp. 123–160). doi:10.1016/b978-0-12-817561-3.00004-4

Sahu, S. B. (2012). Simple one-step synthesis of highly luminescent carbon dots from orange juice: Application as excellent bio-imaging agents. *Chemical Communications, 48*(70), 8835–8837. doi:10.1039/c2cc33796g

Schneider, J. R. (2017). Molecular fluorescence in citric acid-based carbon dots. *Physical Chemistry C, 121*(3), 2014–2022. doi:10.1021/acs.jpcc.6b12519

Sharma, A. &. (2019). Small molecules derived carbon dots: Synthesis and applications in sensing, catalysis, imaging, and biomedicine. *Nanobiotechnology, 17*(1), 92. doi:10.1186/s12951-019-0525-8

Siddique, A. B. (2018). Amorphous Carbon Dots and their Remarkable Ability to Detect 2,4,6-Trinitrophenol. *Scientific Reports, 8*(1), 1–10. doi:10.1038/s41598-018-28021-9

Sigma Aldrich . (2021). Retrieved from https://www.sigmaaldrich.com/TR/en/product/sigma/c8002

Sigma Aldrich . (2021). Retrieved from https://www.sigmaaldrich.com/tr/en/technical-documents/technical-article/analytical-chemistry/photometry-and-reflectometry/ir-spectrum-table

Sigma Aldrich . (2021). Retrieved from https://www.sigmaaldrich.com/TR/en/product/sigma/h8502

Sigma Aldrich . (2021). Retrieved from Maleic acid

Sigma Aldrich . (2021). Retrieved from https://www.sigmaaldrich.com/TR/en/product/sial/m0375

Sigma Aldrich . (2021). Retrieved from https://www.sigmaaldrich.com/TR/en/substance/malonicacid10406141822?context=product

Sigma Aldrich . (2021). Retrieved from https://www.sigmaaldrich.com/TR/en/product/sial/52549

Sigma Aldrich . (2021). Retrieved from https://www.sigmaaldrich.com/TR/en/product/aldrich/p23938?gclid=CjwKCAiAksyNBhAPEiwAlDBeLMmzfKuxcmDhU4-mYS8VF1V-CFKI680JMdjh90jXiMn8ZiuR6BJxkxoCwcEQAvD

Sigma Aldrich . (2021). Retrieved from https://www.sigmaaldrich.com/TR/en/product/sigald/215112

Sigma Aldrich . (2021). Retrieved from https://www.sigmaaldrich.com/TR/en/product/aldrich/408719

Sigma Aldrich . (2021). Retrieved from https://www.sigmaaldrich.com/TR/en/product/sigma/p6001?gclid=CjwKCAiAk

syNBhAPEiwAlDBeLG_RMUdTUpaDibT_t33Aa3cJ5mnjgsDO_secnt1S3812VqmiJaqZbRoCrDsQAvD_BwE

Sigma Aldrich . (2021). Retrieved from https://www.sigmaaldrich.com/TR/en/substance/resorcinol11011108463

Singh, A. K. (2016). Physicochemical, Electronic, and Mechanical Properties of Nanoparticles. *Engineered Nanoparticles*, 77-123. doi:10.1016/b978-0-12-801406-6.00003-0

Singh, I. A. (2018). Carbon Quantum Dots: Synthesis, Characterization and Biomedical Applications. *15*(2), 219-230. doi:10.4274/TJPS.63497

Sk, M. A. (2014). Revealing the tunable photoluminescence properties of graphene quantum dots. *Materials Chemistry C, 2*(34), 6954–6960. doi:10.1039/c4tc01191k

Sodipo, B. K. (n.d.). One minute synthesis of amino-silane functionalized superparamagnetic iron oxide nanoparticles by sonochemical method. *Ultrasonics Sonochemistry, 40*, 837–840. doi:10.1016/J.ULTSONCH.2017.08.040

Song, Y. Z. (2014). Investigation from chemical structure to photoluminescent mechanism: A type of carbon dots from the pyrolysis of citric acid and an amine. *Materials Chemistry C, 3*(23), 5976–5984. doi:doi.org/10.1039/c5tc00813a

Stainless Steel Autoclave. (2016). Retrieved from https://www.researchgate.net/figure/Teflon-lined-stainless-steel-autoclave-used-in-solvothermal-and-hydrothermal-synthesis-of_fig2_312326500

Stepanova, M. D. (2021). Surface modification of carbon dots by UV laser radiation. *Journal of Physics: Conference Series*, *1866.* doi:10.1088/1742-6596/1866/1/012005

Sudolská, M. &. (n.d.). Exact roles of individual chemical forms of nitrogen in the photoluminescent properties of nitrogen-doped carbon dots. . *Applied Materials Today,, 7*, 190-200. doi:10.1016/j.apmt.2017.03.004

Sun, T. X. (2017). Anti-counterfeiting patterns encrypted with multi-mode luminescent nanotaggants. *Nanoscale, 9*(8), 2701–2705. doi:10.1039/c6nr09083d

Sun, Y. P. (2006). American Chemical Society. *128*(24), 7756–7757. doi:10.1021/ja062677d

Tan, D. Q. (n.d.). Effect of UV irradiation on photoluminescence of carbon dots. . *Optical Materials Express, 4*(2), 213-219. doi:10.1364/OME.4.000213

Tang, L. J. (2012). Deep ultraviolet photoluminescence of water-soluble self-passivated graphene quantum dots. *ACS Nano, 6*(6), 5102–5110. doi:10.1021/nn300760g

Tetsuka, H. A. (2012). Optically Tunable Amino-Functionalized Graphene Quantum Dots. *Advanced Materials, 24*(39), 5333–5338. doi:10.1002/ADMA.201201930

Tian, Z. Z. (2017). Full-Color Inorganic Carbon Dot Phosphors for White-Light-Emitting Diodes. *Advanced Optical Materials, 5*(19). doi:10.1002/adom.201700416

Vinoth Victor, G. S. (2021). Non-enzymatic glucose sensor and photocurrent performance of zinc oxide quantum dots supported multi-walled carbon nanotubes. *Materials Science and Engineering B 265(1):115036*. doi:10.1016/j.mseb.2020.115036

Wang Z, D. Z. (2015). Carbon nanomaterial-based electrochemical biosensors: an overview. *Nanoscale*. doi:doi.org/10.1039/C5NR00585J

Wang, H. L. (2021). Carbon dots with positive surface charge from tartaric acid and m-aminophenol for selective killing of Gram-positive bacteria. *Journal of Materials Chemistry B, 9*(1), 125–130. doi:10.1039/D0TB02332A

Wang, J. W. (2012). Amphiphilic egg-derived carbon dots: Rapid plasma fabrication, pyrolysis process, and multicolor printing pattern. *Angewandte Chemie, 51*(37), 9297–9301. doi:10.1002/anie.201204381

Wang, L. C. (2019). Facile preparation of amino-carbon dots/gold nanoclusters FRET ratiometric fluorescent probe for sensing of Pb2+/Cu2+. *Sensors and Actuators, 282*, 78–84. doi:10.1016/J.SNB.2018.11.058

Wang, T. W. (2019). Carbon dots with molecular fluorescence and their application as a “turn-off” fluorescent probe for ferricyanide detection. *Scientific Reports, 9*(1), 1–9. doi:10.1038/s41598-019-47168-7

Wang, Y. &. (2014). Carbon quantum dots: synthesis, properties and applications. *Materials Chemistry, 2*(34), 6921–6939. doi:10.1039/C4TC00988F

West, A. (2018). Experimental Methods to Investigate Self-Assembly at Interfaces. In *Interface Science and Technology* (Vol. 21, pp. 131–241). doi:10.1016/B978-0-12-801970-2.00003-3

Wibrianto, A. K. (2020). Comparison of the effects of synthesis methods of B, N, S, and P-doped carbon dots with high photoluminescence properties on HeLa tumor cells. *RSC Advances, 11*(2), 1098–1108. doi:10.1039/D0RA09403J

Wu, M. Z. (2017). Scalable synthesis of organic-soluble carbon quantum dots: superior optical properties in solvents, solids, and LEDs. *Nanoscale, 9*(35), 13195–13202. doi:10.1039/C7NR04718E

Xu, M. X. (2015). Hydrophilic and blue fluorescent N-doped carbon dots from tartaric acid and various alkylol amines under microwave irradiation. *Nanoscale, 7*(38), 15915–15923. doi:10.1039/C5NR04209G

Xu, Q. K. (2016). Heteroatom-doped carbon dots: synthesis, characterization, properties, photoluminescence mechanism and biological applications. *Materials Chemistry B, 4*(45), 7204–7219. doi:10.1039/C6TB02131J

Yan, F. S. (2019). The fluorescence mechanism of carbon dots, and methods for tuning their emission color: a review. *Microchimica Acta , 186*(8), 1–37. doi:10.1007/s00604-019-3688-y

Yan, F. S. (2019). The fluorescence mechanism of carbon dots, and methods for tuning their emission color: a review. . *Microchimica Acta, 186*(8), 1–37. doi:10.1007/S00604-019-3688-Y/TABLES/5

Yang, F. B. (2020). Nitrogen-doped graphene quantum dots prepared by electrolysis of nitrogen-doped nanomesh graphene for the fluorometric determination of ferric ions. *Microchimica Acta, 187*(6), 1-10. doi:10.1007/S00604-020-04294-8

Yang, P. Z. (2019). Facile synthesis and photoluminescence mechanism of green emitting xylose-derived carbon dots for anti-counterfeit printing. *Carbon, 146*, 636–649. doi:10.1016/J.CARBON.2019.02.028

Yang, P. Z. (2020). Facile synthesis of yellow emissive carbon dots with high quantum yield and their application in construction of fluorescence-labeled shape memory nanocomposite. *Journal of Alloys and Compounds*. doi:10.1016/J.JALLCOM.2020.154399

Zhou, N. W. (2018). Probing Active Sites on Metal-Free, Nitrogen-Doped Carbons for Oxygen Electroreduction: A Review. . *Catalysts, 8*(11), 509. doi:10.3390/CATAL8110509

Zhu, S. M. (2013). Highly Photoluminescent Carbon Dots for Multicolor Patterning, Sensors, and Bioimaging. *Angewandte Chemie International Edition, 52*(14), 3953–3957. doi:10.1002/anie.201300519

Zhu, Z. Z. (2019). Red carbon dots: Optical property regulations and applications. *Materials Today , 30*, 52-79. doi:10.1016/j.mattod.2019.05.003

Zuo, P. L. (2016). A review on syntheses, properties, characterization and bioanalytical applications of fluorescent carbon dots. *Microchimica Acta, 183*(2), 519–542. doi:10.1007/s00604-015-1705-3